Final Report for AFOSR Grant F49620-02-1-0058

Experiments in Transient Growth and Roughness-Induced Bypass Transition

Edward B. White
Department of Mechanical and Aerospace Engineering
Case Western Reserve University
10900 Euclid Ave.
Cleveland, OH 44106-7222

Summary

The work reported here is a series of wind-tunnel experiments that establishes the basic behavior of roughness-induced disturbances that undergo transient algebraic growth in a laminar boundary layer. The experiments explore three aspects of these disturbances' behavior: their fundamental response to various configurations of surface roughness, their receptivity, and their behavior when the surface roughness amplitude is large. The experiments consist of hotwire measurements of the steady and unsteady disturbances created by isolated 3D roughness elements, spanwise arrays of 3D elements and patches of random, distributed roughness. Spanwise roughness arrays are used most extensively as these are found to produce disturbances best-suited for comparison with theoretical predictions.

The results establish that surface roughness does create disturbances that undergo transient growth and that it does so in a manner consistent with the physical picture known as Landahl's lift-up mechanism. The observed growth is qualitatively similar to what is predicted by optimal-disturbance theory. However, theoretical predictions tend to overestimate the length over which disturbances grow and are thought to overestimate the total amount of transient growth. The difference between what is predicted by optimal disturbance theories and what is observed in the experiments is linked to receptivity. Receptivity is found to play two roles in the transient growth phenomenon: it determines initial disturbance amplitude and also distributes energy among the modes of the continuous disturbance spectrum. This second effect is associated with the initial-value-problem formulation of the transient growth problem and explains why some disturbances grow and decay in a manner very similar to what is predicted by optimal-disturbance theory while others only decay and others undergo a significant decay and then a weak phase of transient growth. Regardless of whether certain disturbances undergo transient growth or not, all of the roughness-induced disturbances studied in this experiment have energies that scale approximately as the square of roughness-based Reynolds number across a wide range of Reynolds numbers. At high values of the roughness-based Reynolds number (above approximately 250) transition occurs just aft of the arrays of 3D roughness elements. This transition does not appear to be connected with transient growth. Rather, it occurs because the element's wakes are unstable to a high-frequency Kelvin–Helmoholtz type instability mechanism. Transient growth of steady disturbances only occurs if this rapid transition connected with the unsteady disturbances does not occur.

The results of the experiments are available in the following published and forthcoming papers and student theses:

- White, E.B., and E. Reshotko. 2002. Roughness-induced transient growth in a flat plate boundary layer. *AIAA Paper 2002-0138.*
- White, E.B. 2002. Transient growth of stationary disturbances in a flat plate boundary layer. *Physics of Fluids* **14**(12):4429–39.
- White, E.B., and F.G. Ergin. 2003. Receptivity and transient growth of roughness-induced disturbances. *AIAA Paper 2003-4243.*
- Ergin, F.G. 2003. *Measurements of Roughness-Induced Disturbances in a Flat Plate Boundary Layer.* M.S. Thesis, Case Western Reserve University.
- White, E.B., and F.G. Ergin. 2004. Using laminar-flow velocity profiles to locate the wall behind roughness elements. *Experiments in Fluids* **36**:805–12.
- Rice, J.M. 2004. *Receptivity and Scaling of Non-Optimal Transient Disturbances.* M.S. Thesis, Case Western Reserve University.
- Ergin, F.G., and E.B. White. 2005. Multicomponent and unsteady velocity measurements of transient disturbances. *AIAA Paper 2005-0527.*
- White, E.B., J.M. Rice and F.G. Ergin. 2005. Receptivity of stationary transient disturbances to surface roughness. *Physics of Fluids* **17**(5), in press.
- Ergin, F.G., A. Tumin, M. Choudhari and P. Fischer. 2005. Roughness-Induced Transient Growth: Experiments, Computations, and Theory. *Proc. 4th Intl. Symp. on Turbulence and Shear Flow Phenomena.*
- Ergin, F.G., and E.B. White. 2005. Biorthogonal decomposition of roughness-induced disturbances in a laminar boundary layer. *Physics of Fluids*, in preparation.
- Song, A.J., R.L. Balik, F.G. Ergin and E.B. White. 2005. Effect of the x-based Reynolds number on transient growth receptivity to roughness. *Physics of Fluids*, in preparation.
- Ergin, F.G., and E.B. White. 2005. Unsteady and transitional flows behind roughness elements. *AIAA Journal*, in preparation.

The project involved one faculty member, two graduate students and to undergraduate students, all at Case Western Reserve University. The project P.I. was Edward B. White, and assistant professor in the Department of Mechanical and Aerospace Engineering. The two graduate students were Justin M. Rice and F. Gökhan Ergin. The undergraduate students who assisted with laboratory work are Arnold J. Song and Rebecca L. Balik.

Contents

List of Figures

Final Report for AFOSR Grant F49620-02-1-0058

Experiments in Transient Growth and Roughness-Induced Bypass Transition

Edward B. White
Department of Mechanical and Aerospace Engineering
Case Western Reserve University
10900 Euclid Ave.
Cleveland, OH 44106-7222

1 Introduction and Objectives

The stability of boundary layers has been analyzed most successfully using a normal mode decomposition of the Navier–Stokes equations linearized about a steady basic state. Using this approach, a flow is considered to be unstable if any of its disturbance modes are subject to exponential growth or stable if all of its modes are subject to exponential decay. This analysis leads to the familiar Orr–Sommerfeld/Squire system of equations that can be solved using either a temporal or spatial formulation. The solution describes the growth and decay of Tollmien–Schlichting (TS) waves at various Reynolds numbers, wave numbers and frequencies. For 2-D boundary layers, Squire's Theorem gives the well-known result that 2-D, streamwise-traveling disturbances (i.e., those with spanwise wavenumber $\beta = 0$) are destabilized at lower Reynolds numbers than obliques waves, and consequentially, most of the work done to date on this system has focused on the growth of these 2-D waves because they have been viewed as the most important to the transition process.

While this approach successfully describes the boundary layer when the initial disturbance amplitudes are very low, a number of important problems that include high-amplitude freestream turbulence, high-amplitude surface roughness, or both, undergo a transition process that includes disturbance growth in regions where the Reynolds number is small and all the normal modes are subject to exponential decay. This phenomenon was named *bypass transition* by Morkovin because the disturbances were said to bypass the well-understood TS route to turbulence. For many years bypass was attributed to unknown nonlinear interactions of the disturbance modes, not because of any direct evidence of such interactions, but rather because the transition mechanism in those cases defied any other explanation (Reshotko 2001).

A relatively recent development that addresses the bypass transition problem is a theory regarding a linear instability mechanism known as *transient growth*. Transient growth is an attractive theory because it appears to be capable of explaining many subcritical (i.e., subcritical to the growth of TS waves) transition phenomena of heretofore unknown origin, especially those involving spanwise-varying disturbances, exactly the sort of disturbances produced by surface roughness or freestream turbulence. Transient growth is fundamentally different than TS wave growth because it results from an *inviscid* rather than a viscous mechanism and produces *algebraic* rather than exponential growth. Disturbances that experience this algebraic transient growth eventually decay exponentially, but prior to this decay they are capable of undergoing very significant growth and should therefore be considered to be equally likely as TS waves to lead to transition. Despite the original suspicion to the contrary, transient growth is a linear mechanism.

The transient growth mechanism was first identified by Ellingsen and Palm (1975) and Landahl (1980) and since that time a number of investigators have contributed to a basic theoretical understanding of transient growth. The most recent reviews of these efforts are by Schmid and Henningson (2001) and Reshotko (2001). The basic idea is that transient growth arises from a coupling of oblique TS and Squire modes that exists because the linearized Navier–Stokes equations are not self-adjoint, and therefore have non-orthogonal eigenmodes. Thus, even when all the eigenmodes are damped some transient period of algebraic growth occurs prior to the eventual exponential decay of the disturbances. The most-commonly described physical scenario is that in which stationary streamwise-oriented vortices move fluid from the high-velocity regions of a shear layer to the low-velocity regions near the wall and simultaneously move the low-velocity near-wall fluid away from the wall thus forming the high- and low-velocity longitudinal streak that are ubiquitous in boundary layers in the last stages of transition.

The particular importance of transient growth to the overall understanding of boundary layer transition to turbulence is illustrated by the transition road map, a diagram that illustrates the variety of processes that can lead to transition. The latest revision by Morkovin et al. (1994) is shown in Figure 1. The diagram illustrates that the first stage of the transition is a process known as receptivity, the mechanism whereby environmental disturbances (turbulent and acoustic freestream fluctuations, surface roughness, surface vibration, etc.) enter the boundary layer and provide the initial conditions for instability wave amplification. Details of the transition process vary greatly with the amplitude and character of the initial disturbances. If the initial disturbances are small, the process passes through a sequence of linear growth of primary instabilities leading to secondary instabilities and eventually to breakdown (route A). Moderate amplitude disturbances pass through a phase of transient growth prior to rejoining the low-amplitude path (route B), or may lead directly from the transient growth phase to breakdown (route C). In the route-B scenario, the spanwise variations that are amplified by transient growth may significantly alter the characteristics of the subsequently amplified TS waves. The highest-amplitude disturbances can never be described by linearized equations, and for these the bypass transition label is retained (routes D and E). The diagram illustrates that transient growth is a key feature of many (or even most) transition scenarios that include realistic amplitude initial disturbances. Therefore, transient growth is of critical importance to a correct and complete understanding of boundary layer transition.

The need to understand transient growth and how it may explain cases of bypass transition has a direct bearing on a number of important technological problems. In the external flow arena, the design of laminar-flow wings is quite important for reducing fuel consumption, increasing range, or increasing endurance. Past work on laminar flow control has focused on suppression of TS using suction or manipulation of the suction-side pressure gradient. However, these efforts were not always successful in practice, and roughness was the principal feature that prevented laminar-flow successes in the laboratory from being realized in flight Morkovin (1990). In the unsuccessful cases it is possible that roughness-induced transient growth contributed to premature transition. In these cases, freestream turbulence would not have been important because freestream turbulence levels in the flight environment are below what can be achieved in wind-tunnel experiments. In addition to external flows over wings, transient growth is likely to be relevant to transition of internal flows as well. An example is transition on turbine blades in gas-turbine engines. In this high-freestream-turbulence, high-roughness environment, the mechanisms of transition are not understood, and one frequently reads of "bypass transition" in turbines discussed as an actual transition mechanism rather than as a category label that indicates transition via some unknown mechanism. Understanding the actual mechanisms is of critical importance for improving engine performance because this is the only reliable means of predicting how design changes will affect transition. The importance of transition is that it can produce

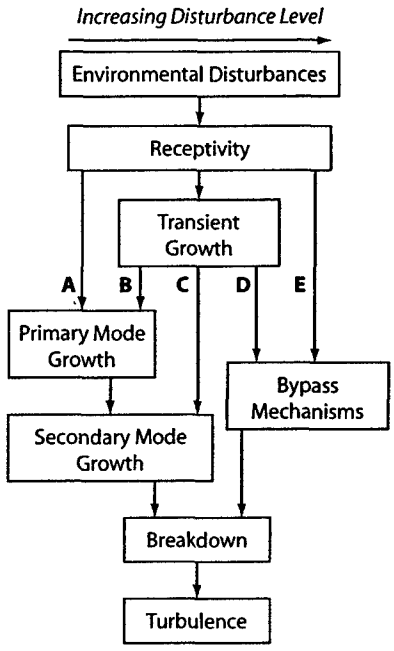

Figure 1: The transition road map. Adapted from Morkovin et al. (1994).

order-of-magnitude-scale changes in blade surface heat transfer and appears to be a mechanism that can suppress stall in low-pressure turbines at cruise conditions.

1.1 Spatial transient growth in Blasius boundary layers: Theory and experiments

Within the context of traditional normal-mode analysis, the basic results of a stability analysis include the minimum critical Reynolds number and the exponential growth rate, wavenumber, and frequency of the most unstable disturbance. This type of result is not appropriate for transient growth studies because transient growth occurs even when all eigenmodes are damped and there are no unstable modes. Instead, a concept introduced by Farrell (1988) is to examine the initial value problem in an optimization context and find the initial disturbance that produces the maximum growth of disturbance kinetic energy at a specified later time. Farrell studied 2-D disturbances of 2-D boundary layers using a temporal approach. Butler and Farrell (1992) extended this to 3-D optimal disturbances in several canonical 2-D shear flows including the Blasius boundary layer. For Blasius flow, Butler and Farrell find that the disturbance kinetic energy growth scales with the length Reynolds number, Re, and that the global optimal disturbance has wavenumbers $\alpha = 0$ and $\beta = 0.38$.

Recently, the study of transient growth in Blasius boundary layers has continued to center on the growth of optimal disturbances, but attention has shifted from temporal to spatial growth, because the spatial approach is usually a better representation of experimentally observed behavior. Andersson et al. (1999), Luchini (2000) and Tumin and Reshotko (2001) address the linearized spatial optimal-disturbance problem and Andersson et al. (2001) use DNS to solve the full nonlinear problem. Within the linearized framework, Andersson et al. and Luchini both consider nonparallel-flow boundary layers. Andersson et al. restrict the problem to steady disturbances and consider a range of Reynolds numbers, whereas Luchini considers both stationary ($\omega = 0$) and traveling ($\omega \neq 0$) disturbances but is restricted to high Reynolds numbers. Above $Re_L = 10^4$ the stationary-disturbance results of Andersson et al.

and Luchini are equivalent. In the high Reynolds number limit, both find that for $x = 0$ (the leading edge) as the disturbance input location and $x = L$ (the reference length for the Reynolds number scaling) as the output location, the optimal spanwise wavenumber is $\beta = 0.45$ and this disturbance reaches a maximum amplitude at $x = 2.5\,L$. Luchini finds that for $\beta = 0.45$, a stationary disturbance is optimal. The optimal input consists of counter-rotating streamwise vortices and the corresponding output consists of alternating high- and low-speed streamwise streaks. At the output location, the maximum streamwise velocity disturbance is at $\eta = 2.2$.

Andersson et al. (2001) approach the full nonlinear spatial-growth problem via DNS using the optimal-disturbance results of Andersson et al. (1999) as inflow conditions to the computational domain. The DNS results validate the linear solution for low-amplitude disturbances. For increasing disturbance amplitudes, the nonlinear solution show progressively less disturbance growth and a disturbance growth maximum that shifts downstream slightly.

Tumin and Reshotko (2001) solve the linearized spatial growth problem in parallel-flow boundary layers by considering the continuous spectrum of eigenvalues associated with a spatial initial-value formulation of the linearized disturbance equations. Tumin and Reshotko find that an $\alpha = 0, \beta = 0.45$, $\omega = 0$ disturbance is optimal, in agreement with Andersson, Berggren, and Henningson (1999) and Luchini (2000), but that the optimal disturbance reaches its maximum amplitude at $x = 1.5\,L$. Despite the qualitative difference in the maximum growth location for the $\beta = 0.45$ disturbance, the growth and decay curves generated by Tumin and Reshotko are qualitatively similar to those of the previous investigators (Andersson et al. 1999; Luchini 2000). Tumin and Reshotko attribute this discrepancy to their parallel, instead of nonparallel, formulation. The optimal disturbance shapes are also very similar, and again, $\eta = 2.2$ is found to be the location of the peak u' disturbance downstream.

Before the work presented here was undertaken little research had been conducted that directly addressed transient growth resulting from surface roughness and none that can directly address the spatial-growth theories. The historical literature on the effects of 3-D surface roughness in boundary layers is extensive but most of this work concerns roughness-induced breakdown that occurs at high roughness-based Reynolds numbers and does not directly address instability mechanisms (see reviews by Dryden 1959; Smith and Clutter 1959; Tani 1961; von Doenhoff and Braslow 1961 and Tani 1969). More modern experiments on subcritical surface roughness by Reshotko and Leventhal (1981), Kendall (1981) and others sought evidence that roughness leads to accelerated transition by destabilizing steady boundary-layer profiles to Tollmien–Schlichting waves but were unsuccessful. With the benefit of hindsight, the experiments by Reshotko and Leventhal and Kendall as well as a much-earlier experiment by Tani et al. (1962) appear to contain evidence of transient growth. However, because transient growth theory had not been developed at the time of those experiments, they do not include the sorts of measurements that are required to perform a detailed comparison with the theory.

Three boundary-layer experiments conducted prior to the current work did directly address transient growth and each was successful in demonstrating it does occur. These experiments were by Breuer and Haritonidis (1990), Westin et al. (1994) and Matsubara and Alfredsson (2001). Breuer and Haritonidis tracked the evolution of an impulsively generated disturbances while Westin et al. and Matsubara and Alfredsson considered unsteady disturbances generated by freestream turbulence. In general, these experiments all confirm that transient growth occurs and the work featuring turbulence-induced disturbances provides disturbance profiles and spanwise wavelengths that are consistent with certain aspects of optimal-disturbance theory. Unfortunately, all of these experiments only consider unsteady disturbances while recent spatial optimal disturbance theories (Luchini 2000; Tumin and

Reshotko 2001) indicate that stationary disturbances are optimal so the relevance of these experiments to optimal-disturbance-theory validation is limited.

1.2 Project objectives

Transient growth theory suggests that many transition scenarios that are not well-described by traditional modal-stability theory approaches may have an explanation that includes transient algebraic disturbance growth at subcritical Reynolds numbers. However, direct evidence of this that is suitable for a direct comparison with theory is lacking. With these ideas in mind, the current experimental work has three principal objectives:

1. to conduct the first comprehensive and controlled experiments on transient growth of stationary, roughness-induced disturbances;
2. to investigate the receptivity of these disturbances to various features of surface roughness; and
3. to explore the limits of high-amplitude transient disturbances and bypass transition.

Achieving these three objectives will provide the first definitive information on the validity and relevance of optimal disturbance theories and will help to establish whether transient growth disturbances can indeed illuminate poorly understood features of roughness-induced bypass transition scenarios.

1.3 Report organization and publications resulting from this project

In the following sections the overall design of the experiments conducted to achieve these objectives are explained (Sec. 2) and the results of various experiments are described in three parts. Results of the basic validation experiments are given in Sec. 3; receptivity results are given in Sec. 4 and results on unsteady disturbances and bypass transition are given in Sec. 5. Overall conclusions are given in Sec. 6.

The information contained here is also available is a series of publications (some still in preparation) that have resulted from this work. The basic behavior of transient disturbances is reported by

- White, E.B., and E. Reshotko. 2002. Roughness-induced transient growth in a flat plate boundary layer. *AIAA Paper 2002-0138.*
- White, E.B. 2002. Transient growth of stationary disturbances in a flat plate boundary layer. *Physics of Fluids* **14**(12):4429–39.
- Ergin, F.G. 2003. *Measurements of Roughness-Induced Disturbances in a Flat Plate Boundary Layer.* M.S. Thesis, Case Western Reserve University.
- Ergin, F.G., and E.B. White. 2005. Multicomponent and unsteady velocity measurements of transient disturbances. *AIAA Paper 2005-0527.* (Spanwise velocity measurements.)

Receptivity issues have been reported by

- White, E.B., and F.G. Ergin. 2003. Receptivity and transient growth of roughness-induced disturbances. *AIAA Paper 2003-4243.*
- Rice, J.M. 2004. *Receptivity and Scaling of Non-Optimal Transient Disturbances.* M.S. Thesis, Case Western Reserve University.
- White, E.B., J.M. Rice and F.G. Ergin. 2005. Receptivity of stationary transient disturbances to surface roughness. *Physics of Fluids* **17**(5), in press.

- Ergin, F.G., A. Tumin, M. Choudhari and P. Fischer. 2005. Roughness-Induced Transient Growth: Experiments, Computations, and Theory. *Proc. 4th Intl. Symp. on Turbulence and Shear Flow Phenomena.*
- Ergin, F.G., and E.B. White. 2005. Biorthogonal decomposition of roughness-induced disturbances in a laminar boundary layer. *Physics of Fluids*, in preparation.
- Song, A.J., R.L. Balik, F.G. Ergin and E.B. White. 2005. Effect of the x-based Reynolds number on transient growth receptivity to roughness. *Physics of Fluids*, in preparation.

Unsteady disturbances and bypass transition findings have been reported by

- Ergin, F.G., and E.B. White. 2005. Multicomponent and unsteady velocity measurements of transient disturbances. *AIAA Paper 2005-0527.* (Unsteady velocity measurements.)
- Ergin, F.G., and E.B. White. 2005. Unsteady and transitional flows behind roughness elements. *AIAA Journal*, in preparation.

And, finally, a finding regarding experimental techniques for roughness array studies is reported by

- White, E.B., and F.G. Ergin. 2004. Using laminar-flow velocity profiles to locate the wall behind roughness elements. *Experiments in Fluids* **36**:805–12.

1.4 Project personnel

Over it's duration this project has involved one faculty member, two graduate students and to undergraduate students, all at Case Western Reserve University (Case). The project P.I. is Edward B. White, and assistant professor in the Department of Mechanical and Aerospace Engineering. The two graduate students are Justin M. Rice and F. Gökhan Ergin. Justin Rice received a M.S. degree in Mechanical Engineering during the course of the project; Gökhan Ergin received a M.S. degree in Mechanical Engineering and will receive a Ph.D. in Mechanical Engineering from work stemming from the project. The undergraduate students who assisted with laboratory work are Arnold J. Song and Rebecca L. Balik.

2 Experimental Setup and Techniques

The experiments presented here are wind tunnel studies that seeks to provide data suitable for comparison with transient growth theories and computations for Blasius boundary layers. Because recent spatial theories of optimal disturbances(Luchini 2000; Tumin and Reshotko 2001) predict that stationary disturbances are optimal, the focus here is restricted to these stationary disturbances. The data consist of hotwire-anemometer measurements of time-averaged and fluctuating streamwise (u) velocities and time-averaged spanwise (w) velocities. Roughness inputs consist of both random, distributed surface roughness patches and spanwise arrays of cylindrical surface-roughness elements.

2.1 Wind tunnel and flat plate model

The wind tunnel facility used for the experiments is the Case Western Reserve University (Case) wind tunnel, an open-return facility with a 710 mm $\times$ 710 mm $\times$ 2.7 m test section and a maximum operating speed of 25 m/s. The tunnel underwent a major renovation in 2001 in support of planned boundary-layer-stability experiments (including the present work) and its design follows the

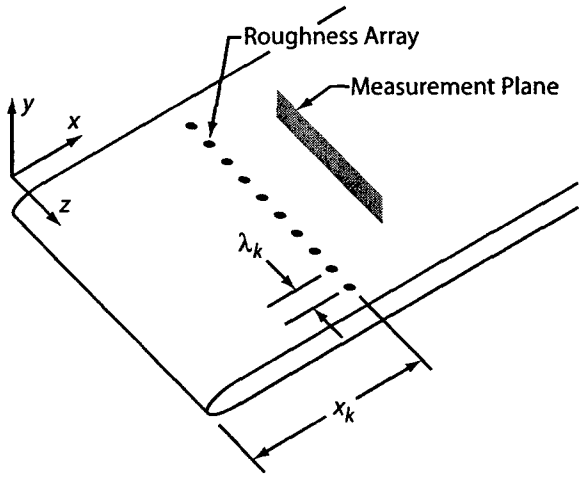

Figure 2: Coordinate system, roughness array parameters and measurement plane orientation.

recommendations of Reshotko et al. (1997) for flow quality. Operating at 12 m/s, the total (not high-pass-filtered) u'_{rms} level in the test section is approximately 0.35% U_∞. Although this level may seem high relative to other tunnels, fluctuation spectra indicate that approximately 93% of the fluctuation power is contained below 1 Hz, a conservative cutoff frequency for AC-coupling filters. To compare the fluctuation measurements of the Case tunnel to facilities whose quoted turbulence levels are measured using traditional AC-coupled fluctuation-intensity measurements, only the u' intensity above 1 Hz should be considered. Restricted to these frequencies, the Case tunnel's u'_{rms} level is 0.09% U_∞. Alternatively, separating the contributions of acoustic and turbulent velocity fluctuations in the manner suggested by Reshotko et al. (1997) shows that the turbulent u'_{rms} amounts to 0.05% U_∞.

The flat plate model used here was originally constructed by Reshotko and Leventhal (1981). The model is mounted vertically in the tunnel 0.5 m downstream of the test section inlet, with the test side located approximately 250 mm from test section's side wall. The plate is constructed of aluminum and is 9.5 mm thick, 635 mm in span, and 1100 mm in length. The plate's leading edge is elliptical with the flat portion of the plate beginning 25 mm from the leading edge. The test side of the plate is polished to a near-mirror finish. When random, distributed roughness is used to generate disturbances this roughness consists of adhesive-backed sandpaper that is placed in a 0.5-mm-deep slot that extends across the plate's span from 100 mm to 200 mm downstream of the leading edge. When roughness arrays are used to generate controlled disturbances the slot is filled with a brass shim that is flush with the plate's upper surface.

The roughness arrays that are used to generate controlled disturbances consist of circular disks of height k and diameter d that are placed in a spanwise array with spacing λ_k and streamwise position x_k. Measurements are obtained in spanwise–wall-normal planes downstream of the array as indicated in Fig. 2. Various roughness array parameters and speeds are used in each of this project's experiments and details of each are given in the appropriate sections.

Proper plate alignment is achieved using four positioning stages located at the four corners of the plate and an adjustable trailing-edge flap. Alignment verification is provided by shape factors (the ratio of boundary layer displacement to momentum thicknesses) obtained during the experiments. True zero-pressure-gradient conditions correspond to a shape factor of $H = 2.59$; variations of ± 0.04

are acceptably close to zero-pressure-gradient behavior (Saric 1996). Displacement thickness and momentum thickness growth in the streamwise direction is used to calculate the virtual leading-edge location for each experimental condition. To perform this calculation, a least-squares regression is performed using all of the spanwise-averaged thickness measurements, $\delta^* = 1.72[(x - x_{vle})/Re']^{1/2}$ and $\theta = 0.664[(x - x_{vle})/Re']^{1/2}$, where x_{vle} is the location of the virtual leading edge and Re' is the unit Reynolds number. For all of the data described below, the x (streamwise) location is cited relative to the physical leading edge, not the virtual leading edge. The Re' and x_{vle} values that result from the least-squares regression analyses are used to generate the boundary-layer thickness $\delta = [(x - x_{vle})/Re']^{1/2}$ and this is used to nondimensionalize the wall-normal coordinate as $\eta = y/\delta$.

2.2 Hotwire measurement techniques and data analysis

Measurements are performed by hotwire anemometers that are moved through spanwise–wall-normal planes orient as shown in Fig. 2 at various x locations. An integer number of steps in z is performed per λ_k and this permits spatial phase-lock averaging to be performed to minimize random variations in the steady velocity field that are not associated with the roughness array inputs. A optimal-filtering approach is used for random, distributed roughness patches. This approach is similar to what is suggested by Naguib et al. (1996) and is described in detail for use with distributed roughness by White and Reshotko (2002). Two different approaches to moving hotwires within the measurement plane were considered. These are discussed in Sec. 2.3 below.

Streamwise velocity measurements are obtained using straight-wire probes and are decomposed into a spanwise-invariant basic state, a stationary disturbance and an unsteady disturbance as

$$u(x, y, z, t) = \overline{U}(x, y) + U'(x, y, z) + u'(x, y, z, t).$$

The basic state can be either considered to be the spanwise mean of the time-averaged velocity field or the mean of the time-averaged velocities that are obtained at z coordinates corresponding to locations between roughness elements. In the first case U' does not include any contribution of a spanwise-uniform steady disturbance; in the second there could be a spanwise uniform steady disturbance.

Of interest in the current work is the energy growth of steady and unsteady disturbances and what contributes to these disturbances. To find these energies a spatial root-mean-squqred (rms) steady disturbance, U'_{rms}, is calculated and this is used to generate the total steady disturbance energy

$$E_{rms} = \int_0^\infty [U'_{rms}(\eta)]^2 \, d\eta.$$

It is also of interest to determine which spanwise modes contribute to E_{rms} for this purpose the U' data is Fourier transformed in z and spatial-mode power spectral densities (PSD) are computed for each inverse spanwise wavelength, λ. The PSD are normalized such that at any wall-normal position η Parseval's theorem can be written as

$$U'^2_{rms} = \int_0^{1/2\Delta z} \mathrm{PSD}(\lambda) \, d(\lambda^{-1})$$

where Δz is the spanwise hotwire step and, therefore, $1/2\Delta z$ is the Nyquist limit. In this way the steady disturbance energy associated with a particular spanwise wavelength is

$$E_\lambda = \int_0^\infty \mathrm{PSD}(\eta, \lambda) \, d\eta.$$

The unsteady disturbance energy is associated with the u' fluctuations and the temporal u'_{rms}. Similar to the steady measurements, a total unsteady disturbance energy is computed via the integral

$$e_{\text{rms}}(x) = \int_0^{\infty} \int_{-\lambda_k/2}^{\lambda_k/2} \left[u'_{\text{rms}}(x, \eta, z)\right]^2 \, d\eta \, dz$$

that is performed across a single roughness-array wavelength. The unsteady fluctuations are decomposed using temporal Fourier transform and temporal PSDs are computed such that

$$u'_{\text{rms}}{}^2 = \int_0^{f_{\text{samp}}/2} \text{PSD}(f) \, df.$$

With this approach the energy contained in 200-Hz frequency band is calculated using an integral over the band and is reported using the center frequency. For instance, the band of frequencies from 600 Hz to 800 Hz will be of interest and the energy in this band is referred to as e_{700}:

$$e_{700}(x) = \int_{600\ \text{Hz}}^{800\ \text{Hz}} \int_0^{\infty} \int_{-\lambda_k/2}^{\lambda_k/2} \text{PSD}(x, \eta, z, f) \, dz \, d\eta \, df.$$

Spanwise velocity measurements are obtained using a pair of slant-wire probes with different angular orientations at the same location. For this purpose, a new hotwire sting design is used that carries a combination of slanted and straight hotwire sensors (Fig. 3). This sting assembly includes a shaft that rotates in a streamlined casing and allows angular calibration of slanted hotwires. Outside the test section, the shaft is connected to an angle indicator and the sting assembly is rigidly attached to the traverse. Inside the test section, the hotwire sensors are placed perpendicular to the shaft's axis through a multiple-hotwire holder. The angular position of the sensors can be adjusted by rotating the spindle of the angle controller with a precision of 0.2°. The multiple-hotwire holder is designed to carry four hotwires. One hotwire is a straight sensor in the freestream; the remaining three sensors are in the boundary layer. The boundary-layer sensors are positioned in a trident design with one straight sensor in the middle and two slanted hotwire sensors mounted 9.5 mm one either side of the the center probe. Using a separation that is an integer multiple of the spanwise step permits all three boundary layer sensors to be placed at the same measurement location at three different spanwise traverse steps. Naturally, this requires excellent alignment of the flat surface with the traverse plane and the sensors with respect to each other and great care is exercised to achieve this alignment.

Slanted hotwire angle calibration is performed following the recommendations of Bruun (1995). First, the yaw angle of each wire is determined by gradually rotating the sensor in the freestream and monitoring the bridge voltage. When the bridge voltage is a maximum, the maximum cooling rate is achieved because the impinging velocity is perpendicular to the wire axis. The calibration of all four sensors is performed simultaneously. First, the sting is positioned so that all hotwires are located in the freestream. Second, it is rotated 5° clockwise from its position during an experiment and a velocity calibration is performed. Third, the sting is rotated 10° counterclockwise and another velocity calibration is performed for the same tunnel speed range. Finally, data from both velocity calibrations at two different angles are combined and the calibration constants are computed by using the King's Law and Hinze's formula (Hinze 1959):

$$V_e = \left(A + B\,E^2\right)^n = \tilde{V}\left(\cos^2\alpha + k^2 \sin^2\alpha\right)^{1/2}.$$

In these equations A, B and n are calibration constants, $\tilde{V}$ is the freestream speed (during the

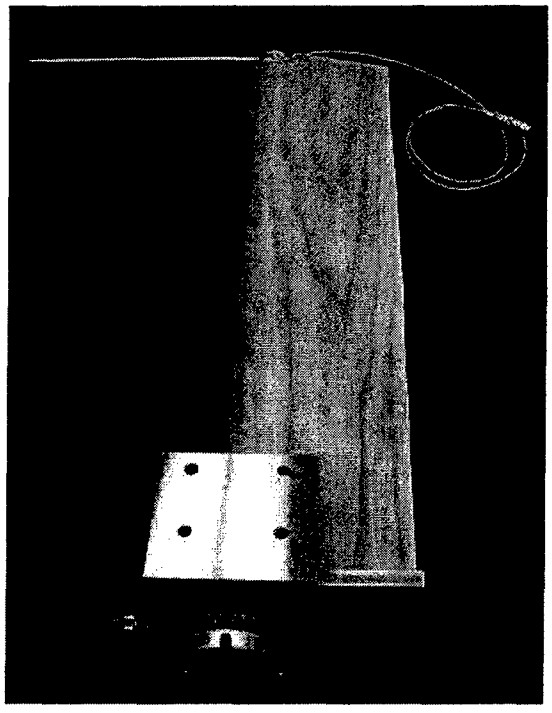

Figure 3: Multiple-probe hotwire sting with angular adjustment capability.

calibration procedure only), V_e is the effective cooling velocity, E is the hotwire voltage, α is the sensor's yaw angle and k is the sensor's yaw coefficient. A nonlinear least-square fit is performed to find A, B, n and k values for each sensor. The yaw coefficient is assumed to be constant following Jørgensen (1971). According to Bruun, this method predicts the effective cooling velocity to within 1% for yaw angles between 0° and 70° and the error reaches only 15% for a yaw angle of 90°.

2.3 Approaches to hotwire scanning

Hotwires are selected as the measurement instrument for the experiments because of their many advantages for velocity disturbance measurements. However, hotwires do have a significant drawback with respect to other types of anemometers because they do not give accurate velocity measurements near a wall. At low velocities in the near-wall region of a boundary layer, wires are affected both by natural convection and by conduction to the surface. Even if these problems did not make measurements near a surface inaccurate, hotwires are so fragile that contact with a solid surface can often destroy a sensor. Therefore, it is common practice to not obtain measurements below a low-velocity cutoff between 12% and 20% of the freestream velocity in low-speed boundary-layer experiments.

Although the lack of data for the lowest velocities is often not significant, the inability of hotwires to approach the wall means that the precise location of the wall is not known in the hotwire's coordinate system (i.e., that associated with the traversing system). Ideally, one would use the test model's solid surface and the freestream velocity to define the experiment's coordinate system, but the hotwire traverse defines another system that can never be perfectly aligned with the model's system. Therefore, some means of locating the wall in the hotwire's system is necessary if measurements are to be assigned a correct spatial reference relative to the model.

There are a number of approaches to generating local wall-location estimates in the hotwire's coordinate system. One of the most common is to perform a least-squares fit of the near-wall portion of the experimentally obtained boundary-layer velocity profile, $U(y)$. Because the no-slip condition guarantees that the velocity at the wall is zero, the y location at which this fit yields $U = 0$ can be taken as an estimate of the wall location. If the streamwise pressure gradient, $\partial p/\partial x$, is locally zero, then the second derivative of the velocity profile, $\partial^2 U/\partial y^2$, is also zero, and a fit to a line is the correct function in this region. The form for this fit is $U(y) = m(y - y_{\text{wall}})$, where m and y_{wall} are the parameters determined by the fit. Even when the pressure gradient is not exactly zero, the second derivative at the wall is often small enough that fitting to a line is still appropriate. It is tempting to consider using a quadratic fit to locate the wall when $\partial^2 U/\partial y^2$ is not zero. However, quadratic fits tend to be dominated by the negative second derivative that exists throughout most of the boundary layer because the portion of the profile near the wall that might have a positive second derivative is not sampled thoroughly enough to yield good fits in this region.

Using a least-squares approach to locate the wall means that wall location estimates suffer from random error due to uncertainty in the velocity measurements and may also suffer from systematic errors if measurements are obtained where $\partial p/\partial x$ and hence $\partial^2 U/\partial y^2$ are nonzero at the wall, such as in the wake of roughness elements. The impact these errors have on an experiment's results varies with the type of result that is of interest. In experiments on steady disturbances, one critical role that wall-location errors can play is to produce errors in the steady disturbance profile, $U'(y)$. An erroneous shift of $\sigma_{y_{\text{wall}}}$ in the local velocity profile, $U(y)$, leads to an error of $(\partial U/\partial y)\sigma_{y_{\text{wall}}}$ in U'. Because disturbance quantities are usually very small, this error can be larger than the disturbance of interest and can easily lead to an estimate of U' with a completely different character than the true disturbance profile.

The most straightforward approach to scanning a hotwire across y–z planes while making wall-location estimates is to make repeated line scans in the negative y direction, once for each z location. This technique is a natural choice because wall-normal velocity profiles are rapidly obtained in a manner consistent with how one usually imagines a boundary-layer profile. In this project, this procedure is implemented as follows. To begin, the boundary-layer hotwire probe is positioned several millimeters outside the boundary layer at the starting z location. Once the experiment starts, the automatic control program initiates a sequence of hotwire movements toward the plate in the negative y direction with velocity measurements obtained for 1.0 s after each movement while the hotwire is stationary. Outside the boundary layer the steps are large, 300 to 400 μm; inside the boundary layer the steps decrease to 30 to 40 μm near the wall. (The actual step sizes are selected to be values that correspond to discrete steps of the traverse's stepper motors.) Movement toward the wall stops once the hotwire measures a velocity below a low-velocity threshold, typically $0.18\,U_\infty$. Once this threshold is passed, the hotwire is returned to its starting position and is then moved one step in the positive z direction. The entire sequence is repeated until the entire y–z plane is covered.

Because the location of the wall is unknown during each scan in the negative y direction, the hotwire's initial location is arbitrarily assigned a value $y = 0$, and subsequent measurement points are assigned appropriate negative y values. Once each line scan ends, a least-squares fit to a line is performed using the points whose velocity is less than $0.35\,U_\infty$. The fit generates the estimated wall location, y_{wall}, and this estimate is subsequently subtracted from all of the points in the line scan so that they all have positive y locations that are (presumably) correctly referenced with respect to the wall. This procedure is implemented using a computer-control program written in-house at Case. The program is named "Slice" because it provides data on individual slices (y–z planes) of the region of

interest. For clarity, the label Slice will be used to denote the wall-location estimating technique that the Slice program implements.

The Slice approach is quite common and has been successfully employed in numerous stability experiments. Besides its conceptual simplicity, it lends itself to straightforward automatic control programs that are easy to implement and modify. Slice and other programs that implement the same technique consist of loops over the basic line scan in which each (x, z) position immediately yields its own wall-position estimate without requiring data from other locations. The technique is also immune from positioning errors that could arise from backlash in the hotwire traverse mechanism. Because all of the wall estimates are obtained independently, any backlash that occurs as the hotwire's motion changes from the positive y to the negative y direction is compensated for in the first large negative y step outside the boundary layer. Once inside the boundary layer, all of the steps are in the same direction and are thus taken without backlash error. Even if the first step does suffer from backlash, it does not affect the wall-location estimate.

Unfortunately, the Slice approach suffers several drawbacks. The first is that it does not produce correct wall estimates at positions with significant velocity-profile curvature near the wall. Moreover, because it does not include any provision for comparing wall estimates from position to position, it does not provide feedback on potential systematic errors resulting from this curvature. (A control program could provide this data, but for this information to be reliable, the traverse system cannot suffer from any backlash.) A second, less serious, drawback is that even when a linear fit is appropriate, there are random errors associated with the wall estimates. Because each location's estimate is independent, the errors of these estimates become the errors of the corrected y coordinates. It would be preferable to use further statistical processing to reduce the wall-location errors prior to performing the correction, but this is not possible when all locations are treated independently.

An alternative strategy for scanning y–z planes that avoids the problems outlined above is to perform repeated line scans in the z direction with each line obtained at a specific y location. This approach was implemented using a second control program named "Dice." To begin the Dice technique, the hotwire is positioned at a starting location outside of the boundary layer. Once the control program starts, the hotwire moves in the positive z location and stops at regular intervals to obtain velocity data. As with the Slice technique, an integer number of z steps is taken per spanwise wavelength so that spatial phase-locked averaging can be performed. Once each scan in z is completed, the hotwire is returned to the starting z location and is then moved one step toward the plate in the negative y direction for the next line scan. Once again, the initial y location is assigned the coordinate $y = 0$ and steps in the negative y direction decrease from 300 to 400 μm to 30 to 40 μm. This process is stopped once the average velocity of a line scan falls below a specified low-velocity threshold.

Besides being simply a different sequence of hotwire movements, Dice differs from Slice in that the least-squares fits used to estimate y_{wall} cannot be performed until data from the entire plane are available. Then, local least-squares estimates of the wall location are performed for individual z locations using points whose streamwise velocity is less than $0.35\,U_\infty$. The difference here is that with all the data in hand it is possible to perform this fit only at selected spanwise locations and, in particular, only at locations that are known not to be strongly influenced by the upstream roughness. This is the critical advantage that Dice provides; it does not make wall-location estimates at locations that are prone to suffer from systematic errors.

To obtain an estimate of y_{wall} across all z locations, including those whose $U(y)$ profiles are influenced by the roughness, a second least-squares fit is performed to generate a quadratic fit of the wall location as a function of z. This second fit uses the local y_{wall} estimates as input. The linear

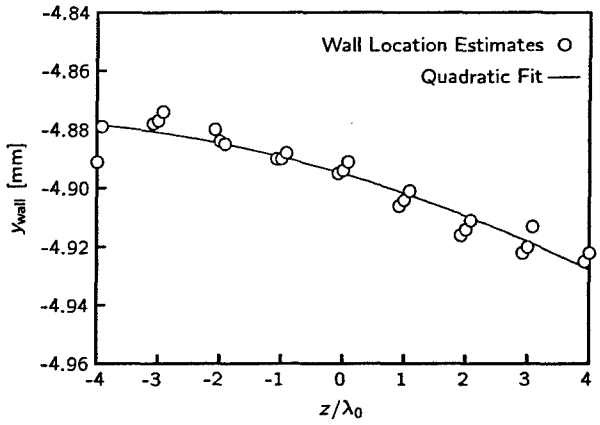

Figure 4: Typical results of a quadratic fit of y_{wall} estimates performed by Dice.

portion of this fit accounts for any misalignment between the flat plate's and the traverse's z axes, and the quadratic portion accounts for warp in the plate's surface and the traverse's z rail. Once obtained, the quadratic fit is used to correct the y locations of all the data so that the velocity profile at each z location is correctly referenced to the wall.

In the experiment for which Dice was developed, three z locations per roughness-array wavelength were selected as locations for which local wall estimates were obtained. These are the locations directly between the roughness elements' centers and one z step on either side of this central location. Figure 4 shows a typical realization of y_{wall} estimates across the span and the quadratic fit that results from these estimates. In the figure, the integer values of z/λ_0 indicate points between roughness elements (where the wall estimates are obtained) and the roughness elements' centers are located at z/λ_0 values of the integers plus one half. The wall-location estimates are fairly consistent from point to point in one cluster, but the data show definitive trends in terms of both skew and warp.

A key feature to note in Fig. 4 is that there is scatter of as much as 10 μm in each of the point clusters. (The displacement thickness at this location is more than 100 times this large, approximately 1.1 mm.) Even under the best circumstances (i.e., no near-wall profile curvature), the same scatter would exist in the wall estimates generated using Slice, and points in all the individual velocity profiles would have y-coordinate uncertainties on this order. However, because these are random errors, using a quadratic fit in z reduces the wall-location uncertainty by not responding to the random error at each z location. In this instance, the wall-location uncertainty associated with the spanwise-fitting technique is 4.7 μm, about half that of the local estimates obtained at the most advantageous spanwise positions between roughness elements. Another advantage of Dice is that by not relying on the low-velocity threshold to terminate negative y movements at individual z stations, it is capable of descending much closer to the wall than Slice in strongly decelerated velocity profiles. In the present experiments, a $0.18\,U_\infty$ velocity threshold sometimes allowed velocities as low as $0.10\,U_\infty$ to be obtained in the near wake of the roughness array.

There are some disadvantages to the Dice approach, however. First, excellent alignment between the plate and traverse is required so that the spanwise line scans are nearly parallel to the plate. If they are not parallel, one end of the span range will include measurement points much closer to the plate than the other and this has disadvantages for estimating the wall location where near-wall data are not available. Even worse, if the plate and traverse are not not parallel, this makes collisions

between the hotwire and the plate more likely. This means that additional plate alignment care is required, and fine tuning of the automatic control program is required so that the hotwire motion that is nominally carried out at constant y actually accounts for some of the plate/traverse skew. A second disadvantage is that the technique is more susceptible than Slice to traverse backlash problems because the z motion reverses direction. Overcoming this requires using a good-quality traversing mechanism with anti-backlash compensation and tuning the traverse speed using multiple line scans at constant y to verify repeatability. Ultimately, once Dice was implemented in the Case tunnel, between 50% and 100% more time was required to scan an entire plane than was required using the Slice procedure.

Comparing data produced using the Slice and Dice techniques can be accomplished by generating and analyzing a data set using Dice and subsequently reanalyzing the same data using Slice. Analyzing the same data using the two techniques provides a means of comparing the techniques without the concern that run-to-run variations in the experiment could interfere with the comparison. When the data are reanalyzed using the Slice approach, least-squares fits are performed using only those points that would be collected in an experiment controlled by the Slice program: those whose velocities fall between $0.18\,U_\infty$ and $0.35\,U_\infty$. Comparisons are performed using data from $x = 310$, 325, and 350 mm and two roughness arrays, $Re_k = 121$ and $Re_k = 54$. For clarity of illustration, the Slice reanalysis is performed using spatially phase-lock-averaged data that have been shifted by the Dice approach's y_{wall} estimate. This way, the wall-location estimates produced using Slice will directly indicate the difference between the two approaches' results. Also, in the results presented below, the y coordinate is replaced by the nondimensional Blasius coordinate, η, to better indicate the impact of wall-estimate errors in terms of the boundary-layer thickness.

As a first step, least-squares estimates of y_{wall} are compared for locations midway between roughness-element centers, $z/\lambda_0 = 0$, the locations at which Dice makes its y_{wall} estimates. Here the y_{wall} estimates produced by Slice vary from the Dice estimates by 0.015 units of η or less. These small variations result from the fact that Dice uses a quadratic fit across z to correct the data's y locations whereas Slice uses local fits to find the wall.

The more interesting comparisons are in the wake of the roughness elements, $z/\lambda_0 = 0.5$. Figure 5 provides these for all three x locations with the $Re_k = 121$ roughness array. The plots on the left of Fig. 5 show the $U(\eta)$ velocity profiles produced by the two analysis techniques and those on the right show the disturbance profiles, $U'(\eta)$, that result from subtracting the basic-state profiles from the wake profiles. Starting with the results from $x = 310$ mm in Fig. 5(a), the $U(y)$ profile obtained using Dice shows very clearly that the true effect of the roughness element is to produce a strongly decelerated profile that must have a positive second derivative, $\partial^2 U/\partial\eta^2$, at the wall. Unfortunately, the region with the positive second derivative falls below the experimental cutoff velocity and, therefore, no direct evidence of the positive second derivative is available to the least-squares fitting routine. This does not interfere with Dice's analysis because the wake profiles are not used to estimate wall positions. However, it is obvious that Slice's analysis will be affected. A least-squares fit performed on the wake profile by Slice incorrectly identifies $\eta = 0.70$ as the wall position and shifts the velocity profile toward the wall by this amount. (In dimensional terms, this shift corresponds to 440 μm, nearly as large as the roughness height.) The Slice $U(y)$ profile in Fig. 5(a) shows that the incorrect estimate of the wall location makes the $U(y)$ profile appear to be accelerated when it is in fact decelerated. The corresponding $U'(y)$ disturbance plots shown in Fig. 5(b) reinforce that the effect of the incorrect wall estimate is dramatic; the disturbance profile produced by Slice indicates strongly accelerated flow whereas the profile produced by Dice shows the correct, decelerated behavior.

These results demonstrate that using wall-location estimates generated by least-squares fits of laminar velocity profiles can lead to grossly inaccurate results if the technique makes wall estimates

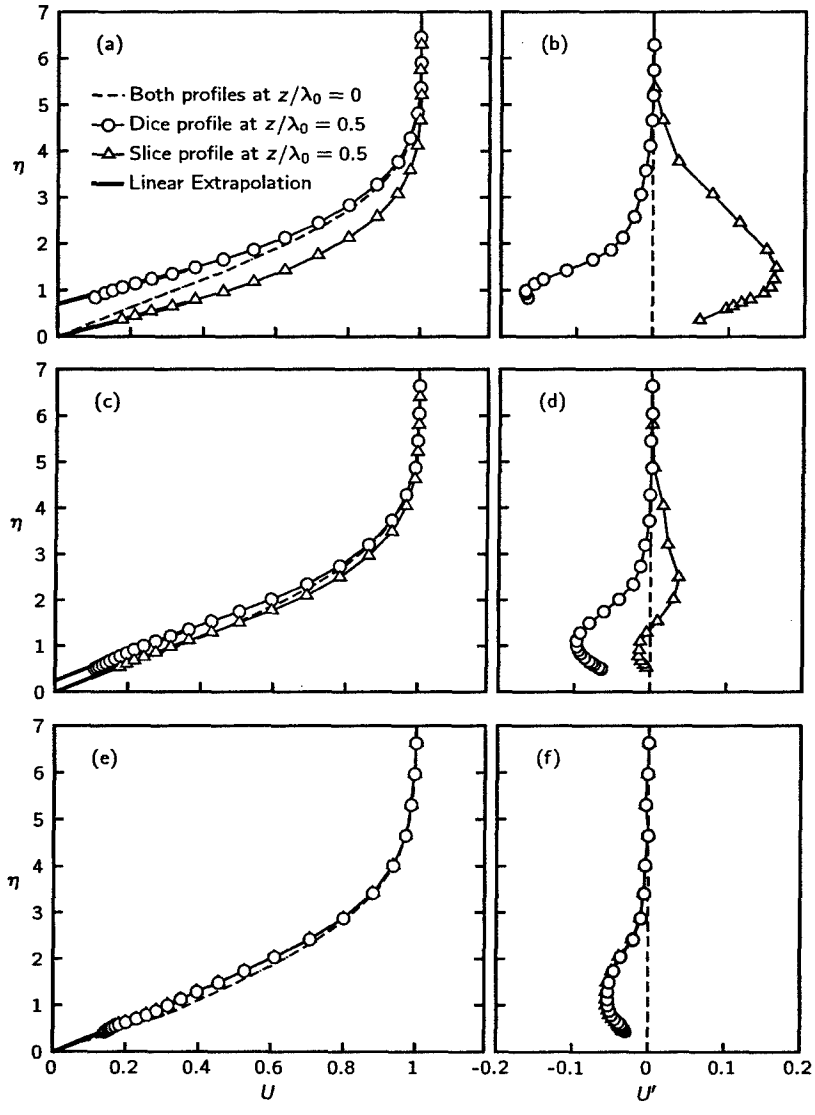

Figure 5: Mean flow, $U(\eta)$, and stationary disturbance, $U'(\eta)$, profiles obtained using Slice and Dice at $x = 310$ mm, (a) and (b); 325 mm, (c) and (d); and 350 mm, (e) and (f). The roughness-array is located at $x = 300$ mm, it's spanwise spacing is 19 mm, and it's amplitude is $Re_k = 121$. The symbols are for identification purposes only and do not represent actual measurement points. However, the point on each curve closest to the wall is representative of the minimum velocity at which data would be available using each technique.

at all locations, including those affected by surface roughness. The alternative approach, making least-squares-based wall estimates only at selected locations and using those estimates to generate a quadratic function that represents the wall location, eliminates the systematic error that can occur in roughness elements' wakes and reduces the random error at all positions. The first approach, referred to here as Slice, produces spurious shifts of the boundary-layer velocity profiles that lead to incorrect stationary disturbance profiles and incorrect conclusions regarding the growth of stationary disturbances in the near wake of roughness. Because the magnitudes of the steady disturbance velocities are small, the shifts induced by the Slice approach lead to measurement errors on the same order of the true disturbance. These can be difficult to detect by comparing results of different roughness amplitudes because the wall-location errors and the disturbance amplitudes scale in the same way with roughness amplitude and, therefore, their combined effect also scales well with roughness amplitude.

3 Basic Experiments on Roughness-Induced Transient Growth

At the outset of this project it was not known whether surface roughness produces stationary transient disturbances and, if they do, whether the evolution of these disturbances can be predicted using optimal-disturbance theory. Therefore, the first objective of the project was to determine whether low-amplitude surface roughness does generate stationary transient disturbances and whether these disturbances behave as optimal disturbances. Of interest are disturbances generated by random, distributed surface roughness, isolated 3D roughness elements and spanwise arrays of 3D elements.

3.1 Preliminary experiments

In an effort to establish the basic behavior and to develop experimental techniques a preliminary experiment was conducted using four surface roughness configurations and an 8 m/s freestream velocity. The four roughness configurations are

- 180-grit ($Re_k \approx 4$) sandpaper from $x = 100$ mm to 200 mm
- 80-grit ($Re_k \approx 24$) sandpaper from $x = 100$ mm to 200 mm
- an isolated, cylindrical roughness element with $d = 7.6$ mm and $k = 380$ μm ($Re_k = 55$) located at $x = 204$ mm
- a spanwise array of four $d = 7.6$ mm, $k = 380$ μm cylindrical roughness elements on a spanwise spacing of $\lambda_k = 16$ mm at $x = 204$ mm

For the first case, the $Re_k \approx 4$ distributed roughness, $\overline{U}$ and U' velocity measurements are obtained at $x = 250$ mm and 500 mm. These data shows that random variations in the steady velocity are large compared to those that can be attributed to the roughness. Using the optimal filtering technique described above it is possible to extract $U'_{\text{rms}}(\eta)$ profiles that are similar to the expected Klebanoff-mode shape that is predicted by spatial optimal disturbance theories (Andersson et al. 1999; Luchini 2000; Tumin and Reshotko 2001) with a peak amplitude of approximately $0.009\,U_\infty$ at $x = 250$ mm and $0.006\,U_\infty$ at $x = 500$ mm.

Increasing the distributed roughness amplitude to $Re_k = 24$ provides a much stronger disturbance signal. Profiles of $\overline{U}$ and U'_{rms} obtained using the optimal-filtering technique for this configuration are given in Fig. 6. Although the profiles indicate that the expected Klebanoff-mode shape does exist, it is not growing with increasing downstream distance. This is somewhat surprising given that many of

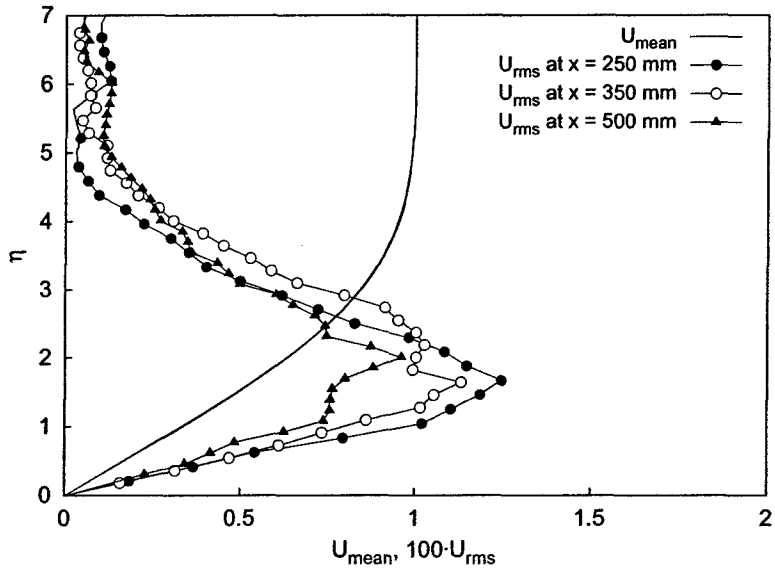

Figure 6: Profiles of $\overline{U}$ and U'_{rms} with 80-grit roughness between $x = 100$ and 200 mm.

the spanwise wavelength components that make up the steady disturbance are sufficiently long (the longest significant spanwise wavelength component is about 24 mm) that they can still be expected to be growing in the measurement region based on optimal disturbance theory.

To increase the amplitude of the disturbance signal available for analysis, a single isolated roughness element is applied just aft of the 180-grit roughness. The element is 7.6 mm in diameter and has a height of 380 μm, which gives $Re_k = 55$ at nominal operating conditions. At $x = 250$ mm and $x = 450$ mm, the distortion of the mean-flow traces due to the combined action of the 180-grit paper and isolated roughness are given in Figs. 7 and 8, respectively. It is immediately apparent that the roughness element produces much higher amplitude distortion than the 180-grit paper and that the distortion is localized in the region directly downstream of the element. The velocity traces suggest that the form of the disturbance is a pair of counter-rotating vortices that lift low-speed fluid away from the wall directly behind the element and pull high-speed fluid toward the wall at the edges of the element. Moving from $x = 250$ to 450 mm, the width of the region influenced by the isolated element does not noticeably increase. This is in good agreement with Kendall's (1981) observation that the wakes of isolated roughness elements are very persistent. Here the two stations are approximately 20 and 85 boundary-layer thicknesses downstream from the element, and yet the distortion caused by the element can be clearly distinguished in each. Another observation of Kendall's that is confirmed here is that a velocity defect is apparent directly behind the element in the near-wake region. However, in the far-wake region, only a velocity excess that extends across the entire diameter of the roughness is observed.

The fact that the mean-flow distortion remains limited to a spanwise region directly in the wake of the element is quite different from what is observed when isolated roughness elements generate streamwise vortices that are unstable modes of exponentially growing instabilities. In the crossflow-transition experiment of Radeztsky et al. (1999), an isolated element was observed to produce a packet of streamwise vortices that grew in both amplitude and streamwise extent with streamwise distance.

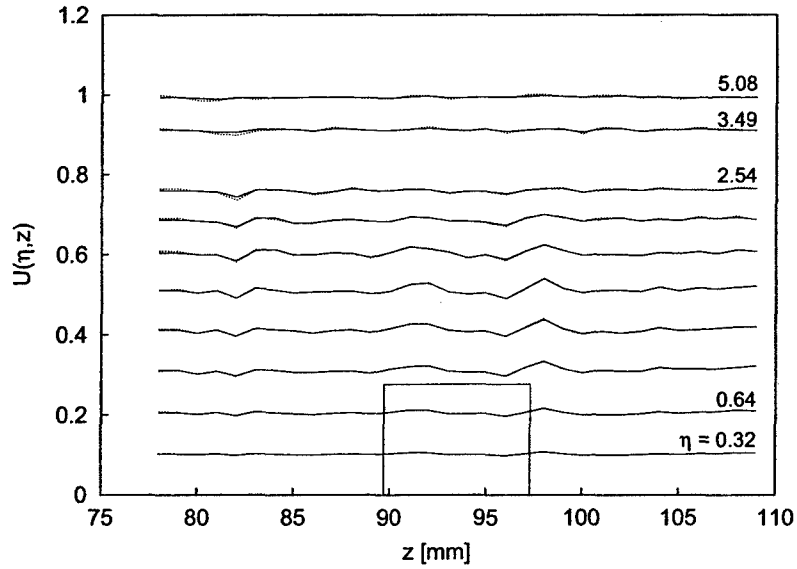

Figure 7: Streamwise velocity traces (not contours) at $x = 250$ mm with 180-grit sandpaper plus a single roughness element installed. The rectangle indicates the approximate location of the roughness element and the velocity of the undistorted boundary layer at the top of the roughness element.

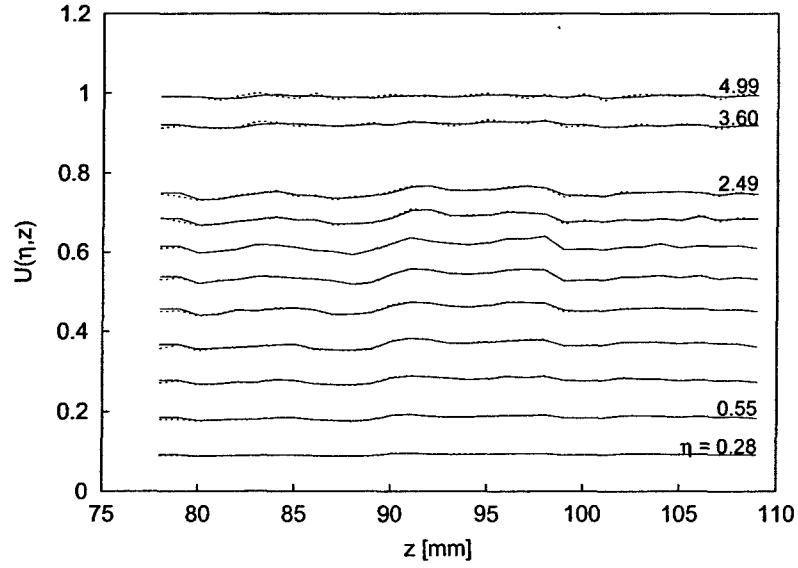

Figure 8: Streamwise velocity traces at $x = 450$ mm with 180-grit sandpaper plus a single roughness element installed.

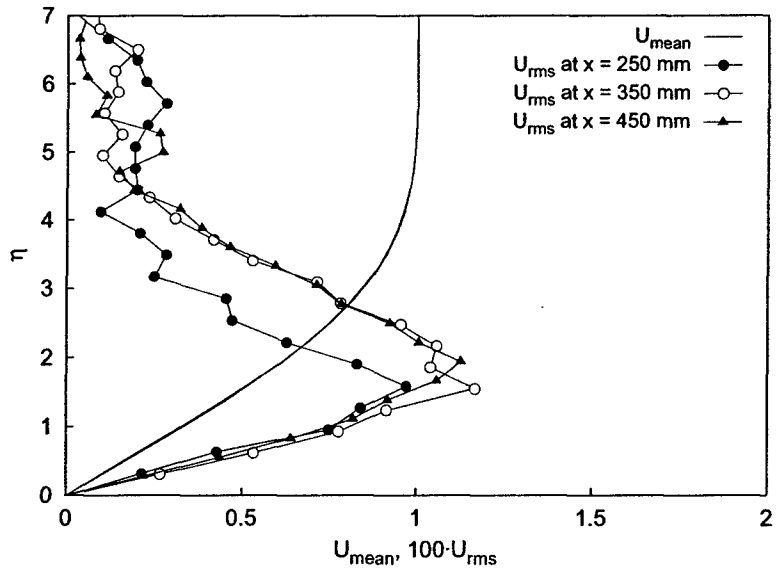

Figure 9: Profiles of $\overline{U}$ and U'_{rms} with 180-grit sandpaper plus a single roughness element installed.

Profiles of the velocity trace rms levels at $x = 250$, 350, and 450 mm (Fig. 9) confirm that the introduction of the isolated roughness element substantially increases the stationary disturbance level. (Note that the rms levels are obtained over the entire 31 mm extent of the scan, only about 10 mm of which appears to be influenced by the roughness.) The rms profiles show that as x increases, the peak rms level increases from 0.0097 at $x = 250$ mm to 0.0117 at $x = 350$ mm and then decreases somewhat to 0.0112 at $x = 450$ mm. As this occurs, the η location of the peak continues to increase, moving from $\eta = 1.59$ to $\eta = 1.94$. The change in the location of the peaks with x indicates that the rms curve is not self similar. This is different from the behavior observed by Westin et al. (1994) who observed that a turbulence-induced u'_{rms} peak remained fixed at $\eta = 2.3$. All of the rms curves bear a very strong resemblance to Klebanoff modes that are observed under conditions of moderate freestream turbulence. Here, of course, the measurements are of the variations in steady velocity across a range of span instead of the unsteady fluctuations at a single location.

The spatial spectra of the velocity traces are quite revealing in this case. The velocity power spectral densities (PSD) are given in Fig. 10. These curves are obtained from the η position with the largest rms level at each x location. At $x = 250$ mm, most of the disturbance energy is concentrated at spanwise wavelengths of 6.4 and 3.6 mm. Because the extent of the sample is relatively small and the wavelength resolution is rather low, these wavelengths correspond to the roughness diameter and half the roughness diameter, respectively. Moving downstream, the shorter wavelength, 3.6 mm, decays rapidly, while the longer wavelength, 6.4 mm, grows and then decays slightly. Meanwhile, a 16.0 mm wave that was not evident at $x = 250$ mm grows to be the largest-amplitude wave at $x = 450$ mm. Using the displacement thickness measured at $x = 350$ mm to provide an appropriate boundary-layer scale, the three wavelengths, 3.6 mm, 6.4 mm, and 16.0 mm, correspond to nondimensional spanwise wavenumbers $\beta = 1.0$, 0.6, and 0.2, respectively. Therefore, the transient-growth theories suggest that the 6.4 mm wave is close to optimal, whereas the shorter wavelength should decay in the test region and the longer wavelength should grow slowly and algebraically. At least qualitatively, that

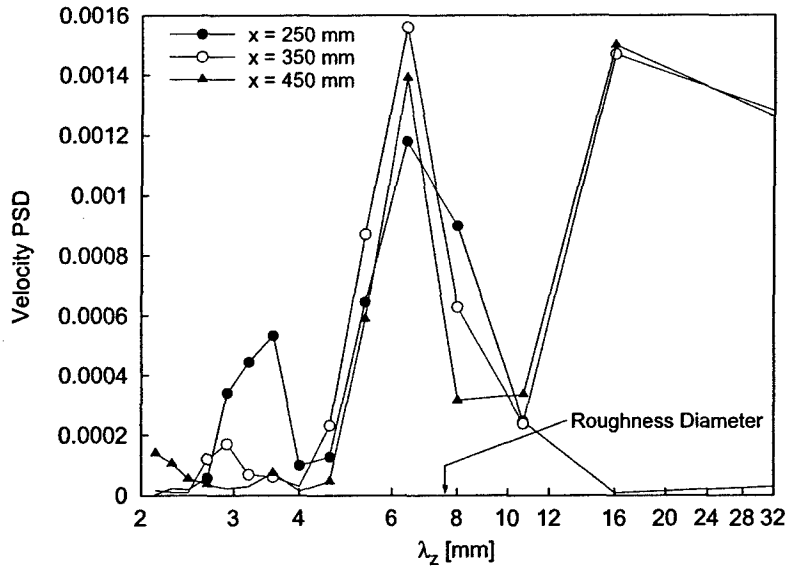

Figure 10: Streamwise-velocity power spectra with 180-grit sandpaper plus a single roughness element installed. At each x, the spectrum is obtained at the η location of maximum U'_{rms}.

is what is observed here. The 3.6 mm wave decays immediately, the 6.4 mm wave grows and then decays slightly, and the 16.0 mm wave grows to large amplitude without decaying.

Because the application of an isolated roughness element is seen to be quite effective, both for increasing the overall disturbance amplitude and for providing a distinct disturbance spectrum, an array of four roughness elements are applied at $x = 204$, all with $k = 380$ μm. The spanwise spacing of the elements is $\lambda_k = 16$ mm, approximately twice the element diameter. This spacing is designed to enhance the 16.0 mm component of the spectrum that was not evident at the most upstream location for the single-element test. Scans with this roughness configuration extend over 120 mm in span and include a region on both sides of the array that is not in the wake of the roughness elements. As before, the zone influenced by the roughness is not observed to spread in the span direction, so the data sets are truncated to include only the central region that is directly influenced by the roughness. The velocity traces in the affected region are given in Fig. 11. Examining the rms disturbance profiles (Fig. 12), the effect of the increased number of elements is exactly what is expected: the maximum amplitudes are increased because the averaging does not include a region without disturbance generators. Furthermore, the rms curves confirm the growth behavior observed in the single-element scans; that is, moving downstream, the maximum of the rms profile grows and then decays while the η location of the maximum moves away from the wall with increasing downstream distance, in this case ranging from $\eta = 1.26$ at $x = 250$ mm to $\eta = 2.22$ at $x = 650$ mm.

Spatial spectra of the velocities at the location of maximum U_{rms} are given in Figure 13. The larger spanwise extent of these measurements relative to the isolated roughness case provides for better spectral resolution. With this resolution, it is apparent that the disturbances begin, and remain, very sharply defined in wavenumber space. In this case, we see the largest spectral components at $\lambda = 17.2$, 7.7, and 5.3 mm, which roughly correspond to λ_k, $\lambda_k/2$ (also the roughness diameter) and $\lambda_k/3$, respectively. The corresponding βs are 0.73, 0.51, and 0.23, respectively. Therefore, the $\lambda_k/2$ wave is nearly optimal and should experience the largest growth, whereas the $\lambda_k/3$ wave should grow

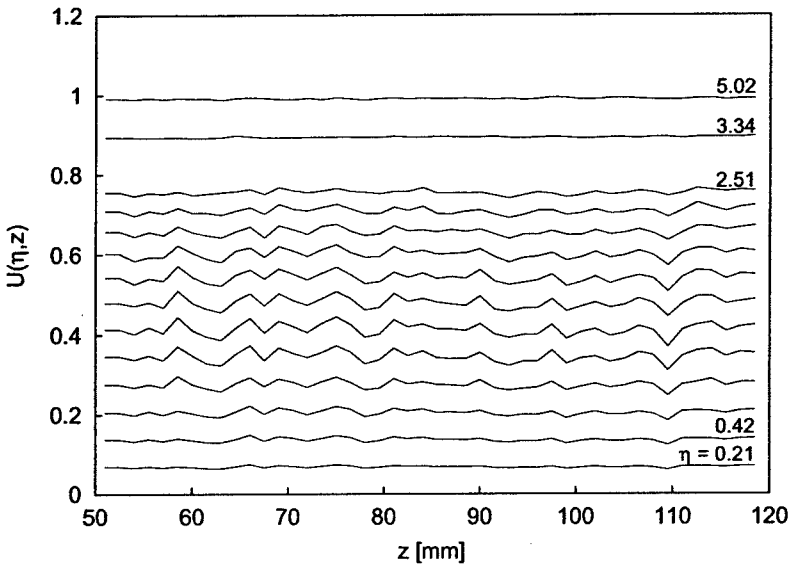

Figure 11: Streamwise velocity traces at $x = 250$ mm with 180-grit sandpaper plus a four-element roughness array installed.

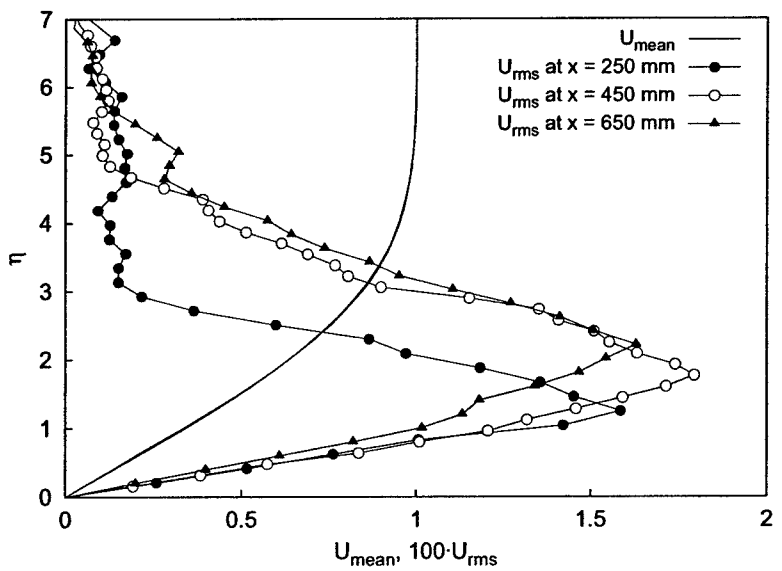

Figure 12: Profiles of $\overline{U}$ and U'_{rms} with 180-grit sandpaper plus a four-element roughness array installed.

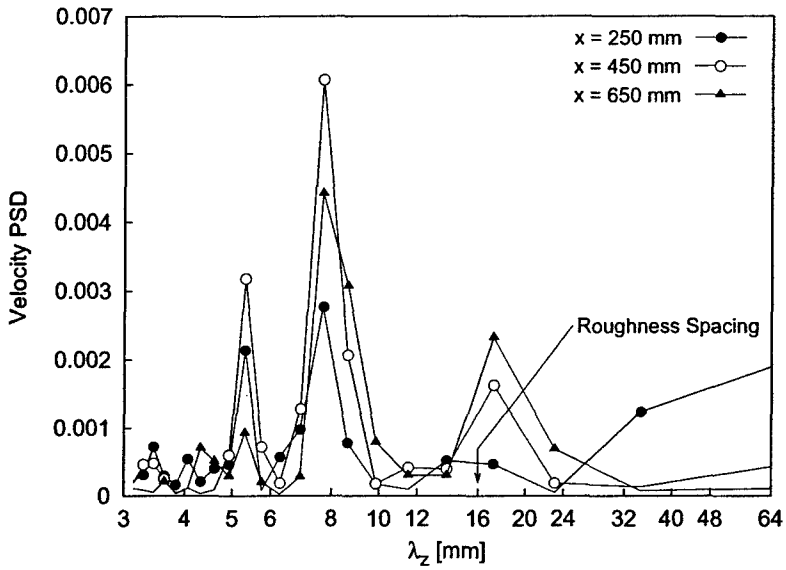

Figure 13: Streamwise-velocity power spectra with 180-grit sandpaper plus a four-element roughness array installed. At each x, the spectrum is obtained at the η location of maximum U'_{rms}.

and decay quickly and the λ_k wave should not reach maximum amplitude in the test region. In contrast to the behavior observed for the isolated element, Figure 13 shows that the shortest wavelength does undergo a brief period of growth prior to decaying, as does the 7.7 mm wave. The longest wavelength increases in power throughout the test region.

The higher quality spectral data afforded by the increased span range and periodic roughness make it possible in this case to plot PSD versus η for various wavelengths. Typical curves are shown for $x = 450$ mm in Fig. 14. Individual wavelength components included in this plot show that the location of the maximum PSD moves to larger values of η with increasing λ. That is, longer wavelength disturbances appear to have peak amplitudes farther from the wall than short-wavelength disturbances. If this can be confirmed, it would indicate why the rms peaks move to larger η for increasing downstream distance: the shift of the rms peak toward increasing η with increasing x location reflects an increasing fraction of the total disturbance energy represented by long, rather than short, wavelengths.

In addition to providing meaningful PSD versus η curves, the better quality spectra also make it possible to track the energy growth of particular disturbances. To accomplish this, the PSD for the three dominant wavelengths are integrated versus y, the dimensional wall-normal distance, at each x station. The resulting integrals are referred to as "disturbance energy" in Fig. 15. This integral quantity is used as a measure of disturbance growth for a variety of reasons. First, because the PSD versus η data exhibit large fluctuations, an integral measure will produce a smoother energy growth result than a measure based on a single point. Second, if a point were to be selected for a single-point growth measure, it is unclear what point should be selected and whether this selection should remain fixed or be allowed to vary with λ, or x. Finally, energy integrals are used as growth measures in transient-growth theories, so it is natural to do the same here.

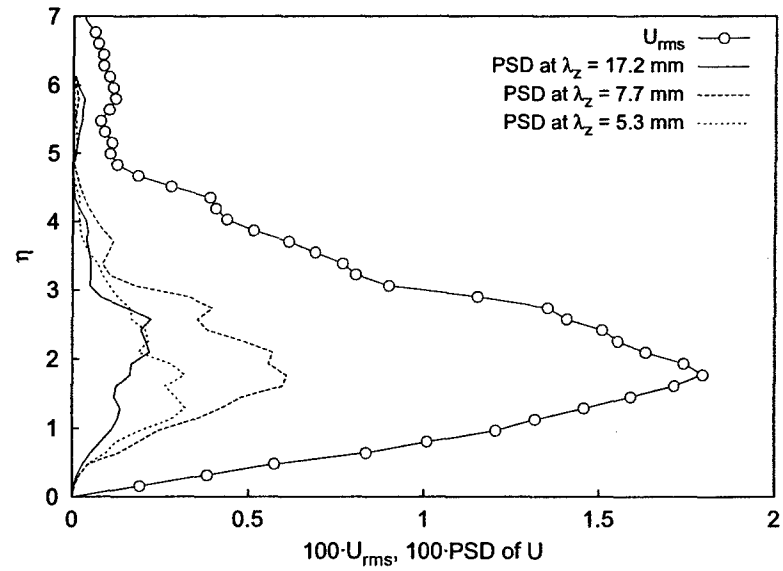

Figure 14: Profiles of U'_{rms} and PSD at $x = 450$ mm with 180-grit sandpaper plus a four-element roughness array installed.

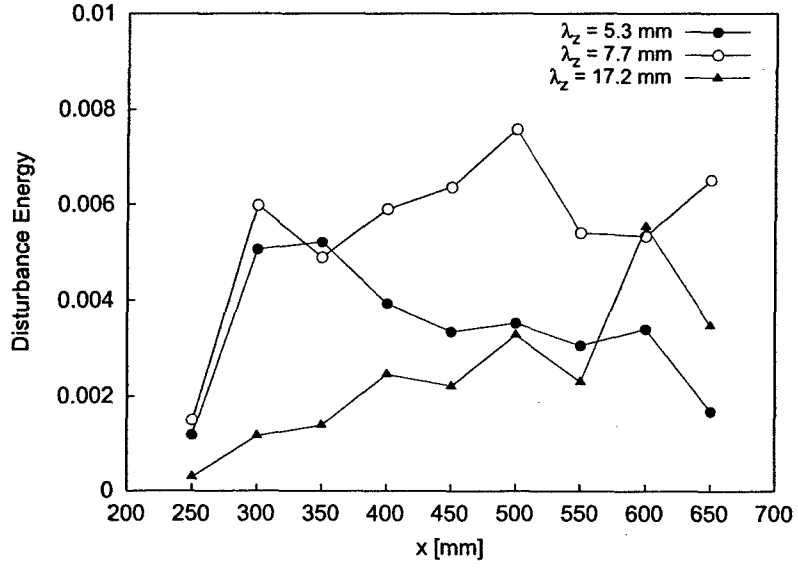

Figure 15: Stationary disturbance energy growth with 180-grit sandpaper plus a four-element roughness array installed.

The evolution of the integrated disturbance energies progresses much as the individual spectra would suggest. The 5.3 mm wavelength disturbance grows significantly from $x = 250$ mm to $x = 350$ mm and then decays throughout the remainder of the measurement region. The 7.7 mm wavelength disturbance grows just as quickly over the first 50 mm and then continues to grow more slowly over the remainder of the domain. The 7.7 mm disturbance may begin to decay by $x = 550$ mm, but because the point-to-point fluctuations of the growth curves are so large, this is impossible to verify. Finally, the 17.2 mm wavelength disturbance grows much more slowly than the shorter-wavelength disturbances, but it continues to grow throughout the measurement region. These data are too preliminary to provide specific validation of transient-growth codes, but the qualitative agreement with the sort of behavior predicted by the various transient-growth theories is encouraging.

The data from these four preliminary cases provide strong evidence that transient growth does occur for steady, roughness-induced disturbances. In these cases, the spanwise rms of time-averaged velocity, U_{rms}, the quantity relevant to stationary, streamwise disturbances, grows and then decays in the measurement region. The preliminary experiments are not sophisticated enough to provide detailed validation of particular transient-growth models, but the qualitative aspects of the disturbance growth are consistent with transient-growth theory. In particular, where it is possible to identify certain spanwise wavelengths of the steady disturbance, the wavelengths longer than the so-called optimal disturbance grow more slowly than other disturbances, wavelengths shorter than the optimal disturbance grow rapidly and then decay, and wavelengths close to the optimal wavelength grow to the highest amplitude in the measurement region.

Besides these confirmations of the theory's predictions, a number of other observations are made. First, as the x location increases, the location of the U_{rms} peak moves to larger η. This behavior is in contrast to what is observed for u'_{rms} peaks in boundary layers exposed to high levels of freestream turbulence (Westin et al. 1994). There the peak is always located near $\eta = 2.3$ and the u'_{rms} distribution appears self similar. The behavior seen here may result from the differential growth of disturbances of various wavelengths, all of which may have a somewhat different distribution of disturbance energy in η. In any case, it is observed here is that U_{rms} is clearly not self similar. Beyond this, the experiment confirms a number of observations of Kendall (1981) regarding the behavior of subcritical roughness-induced disturbances.

For the random, distributed roughness cases, the results are more difficult to interpret. In both cases, the U_{rms} curve decays from the outset, and none of the clear indicators of transient-growth behavior that are apparent for the isolated-roughness and roughness-array cases is observed.

3.2 Roughness-array experiments

The preliminary experiments clearly establish that spanwise arrays of roughness elements are very useful for establishing amplitude- and wavelength-controlled disturbances that can be compared to theoretical predictions. Moreover, the existence of spanwise periodicity makes spatial phase-lock averaging possible and this provides a more effective means of removing random noise than the optimal filtering technique that is used when a spatial phase reference does not exist. Therefore, more detailed experiments were conduced using three separate configurations labeled A, B and C. Each configuration used cylindrical roughness elements with $k = 380$ μm, $d = 6.35$ mm, and $x_k = 225$ mm. Configurations A and B had the elements spaced with $\lambda_k = 12.5$ mm (approximately twice the elements' diameter) while configuration C had $\lambda_k = 25.0$ mm (four times the diameter). The experiments of configurations A and C were conducted at a freestream speed of 12 m/s while

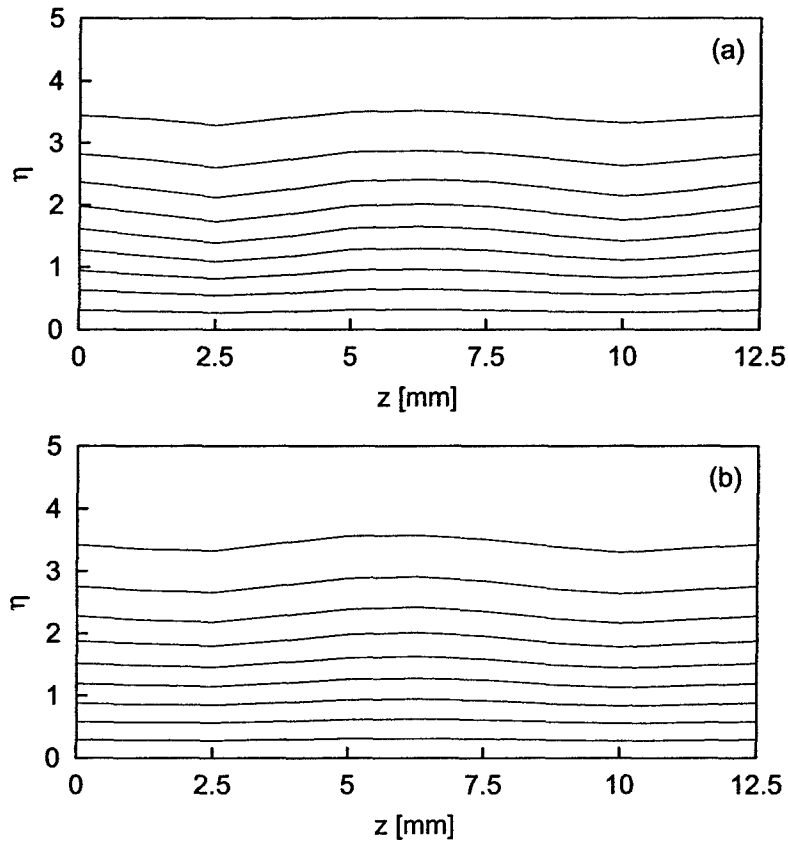

Figure 16: Mean-flow velocity contours for configuration A: $U_\infty = 12$ m/s with a 12.5-mm-spaced roughness array. Contours are averaged over eight disturbance input wavelengths. Contour lines represent increments of $0.1\,U_\infty$. Plots are shown for (a) $x = 350$ mm and (b) $x = 650$ mm.

the experiments of configuration B were conduced at a freestream speed of 8 m/s. The velocities produced Re_k values of 80 for configurations A and C and 45 for configuration B.

Configuration A, the experiment's baseline configuration, features a freestream speed of $U_\infty = 12$ m/s and a roughness spacing, $\lambda_k = 12.5$ mm. Based on the boundary layer thickness at the roughness location, λ_k corresponds to a nondimensional spanwise wavenumber $\beta = 0.24$. Although optimal-growth studies cite optimal wavenumbers, wavelengths are used here for the presentation of experimental data because these are more intuitively related to the boundary layer thickness and roughness spacing. The most straightforward means of visualizing stationary disturbances is via contour plots of the time- and phase-lock-averaged streamwise velocity in wall-normal–spanwise (η, z) planes. Two such plots for $x = 350$ and 650 mm are given in Fig. 16. At these locations the plots suggest the accumulated effect of a counter-rotating pair of streamwise vortices that produce a low-speed region on the roughness elements' spanwise centerlines ($z = 6.25$ mm in the figure) and high-speed regions on either side of the centerline.

The U'_{rms} distributions corresponding to the velocity profiles of Fig. 16 bear a strong resemblance to the Klebanoff modes that are observed in instances of high freestream turbulence (Klebanoff 1971; Kendall 1985; Westin et al. 1994; Matsubara and Alfredsson 2001) and in the distributed roughness

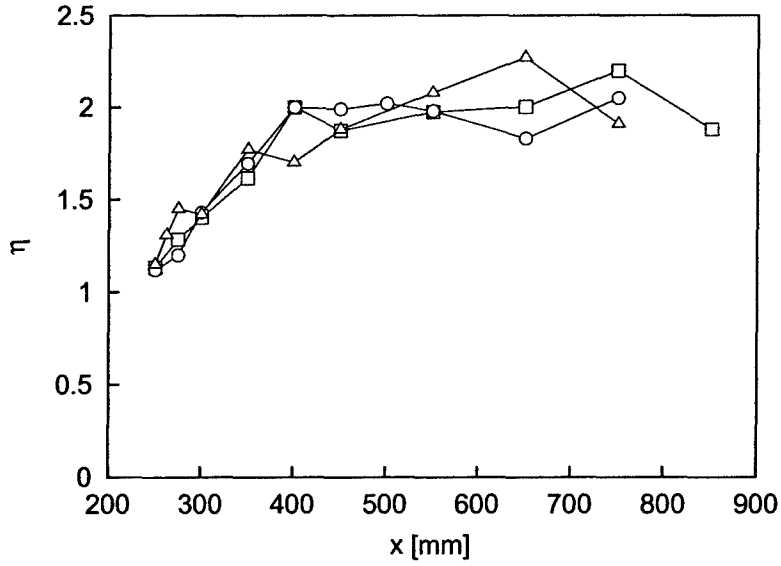

Figure 17: Variation of the location of maximum U'_{rms} with streamwise position for configurations A (□), B (○), and C (△).

study of Reshotko and Leventhal (1981). However, unlike those studies' results that show a $u'_{rms}(\eta)$ profile with a peak at $\eta = 2.2$ at all streamwise locations, here, the location of the $U'_{rms}(\eta)$ distribution's peak is not fixed at $\eta = 2.2$, but instead occurs at $\eta < 2.2$ and moves to higher η with increasing downstream distance. The variation of the disturbance profile means that $U'_{rms}(\eta)$ is not self-similar. A plot of the peak's location as a function of streamwise distance (Fig. 17) suggests that the peak may be approaching $\eta = 2.2$, but it does not reach this value in any of the three configurations included in this experiment. Gaster et al. (1994) show similar disturbance profiles with peaks at $\eta \approx 1.8$ at two downstream locations.

Movement of the U'_{rms} peak was noted by White and Reshotko (2002), who suggested that this behavior would occur if the η location of the disturbance maximum were a function of disturbance wavelength; movement of the U'_{rms} peak would then occur as increasingly long wavelength disturbances become more important. However, spectra from White and Reshotko's study were not sufficiently well resolved to verify this suggestion. Figure 18 gives spanwise spectra of the U' from the location of maximum U'_{rms} at $x = 350$ and 650 mm. The plots show that the spectra are well resolved and that the roughness array is very effective at producing disturbances at distinct wavelengths. The three dominant wavelengths are 12.31, 6.27, and 4.16 mm, which correspond to λ_k, $\lambda_k/2$, and $\lambda_k/3$, respectively. The spectra for all η are assembled to give wall-normal profiles of PSD at each of the important wavelengths (Fig. 19). These profiles indicate that at each streamwise location, the amplitude maximum's location *is not* a strong function of wavelength, and therefore, these data do not confirm White and Reshotko's suggestion. Instead, every wavelength's amplitude maximum moves to higher η with increasing streamwise distance; the individual components' disturbance profiles are not self-similar.

Disturbance kinetic energy is plotted versus streamwise location in Fig. 20. The figure shows rapid growth of all disturbances just downstream of the roughness array followed by slow decay downstream of each disturbance's kinetic energy maximum. Qualitatively, the curves are similar to what is predicted

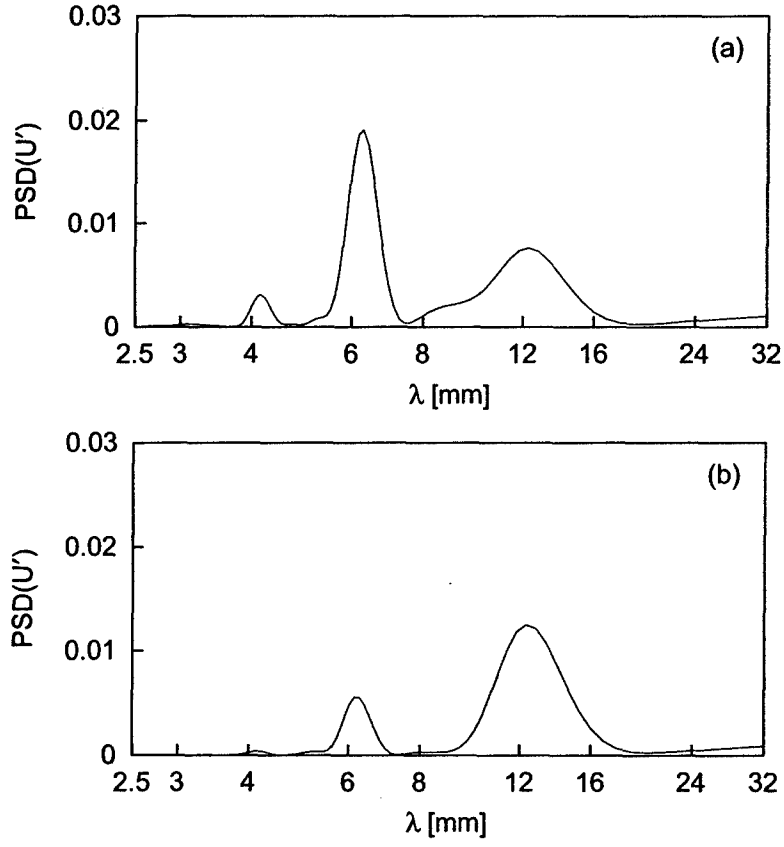

Figure 18: Spanwise-wavelength power spectral density versus spanwise wavelength for configuration A. The curves are obtained at the η for maximum U'_{rms} at each x location. Plots are shown for (a) $x = 350$ mm and (b) $x = 650$ mm.

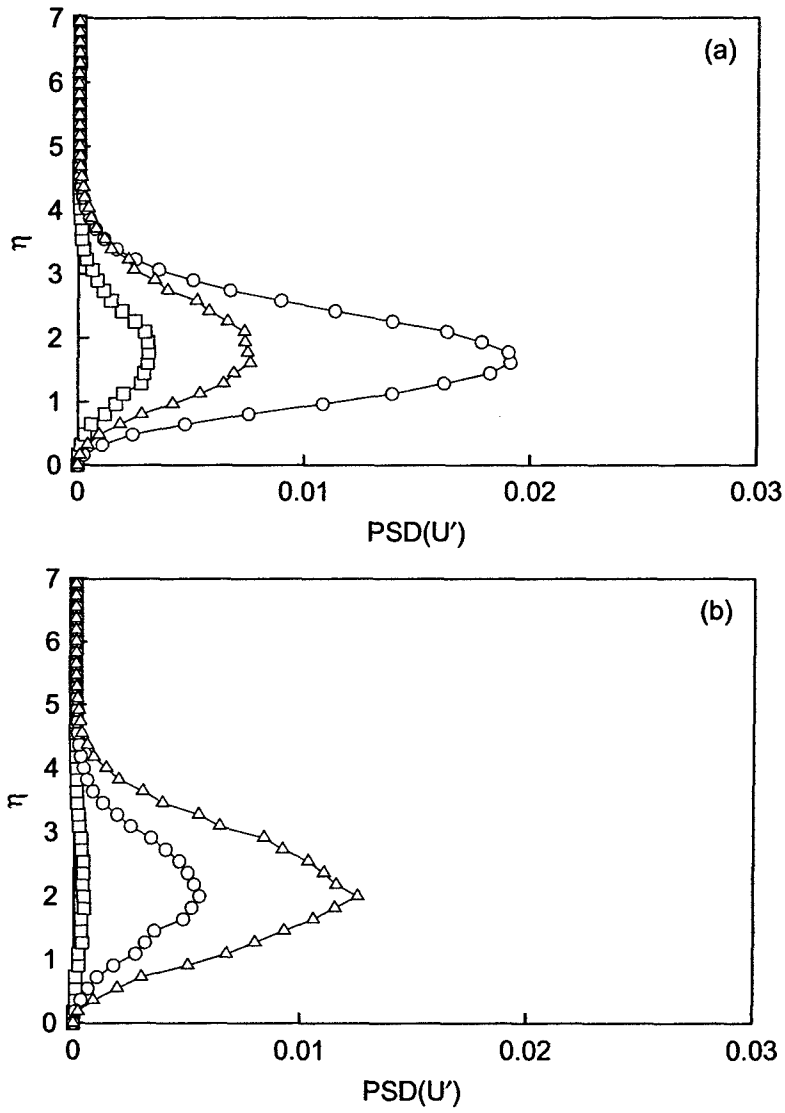

Figure 19: Spanwise-wavelength power spectral density profiles for configuration A. Plots are shown for (a) $x = 350$ mm and (b) $x = 650$ mm. The symbols correspond to 4.16-mm (□), 6.27-mm (○), and 12.31-mm disturbances (△).

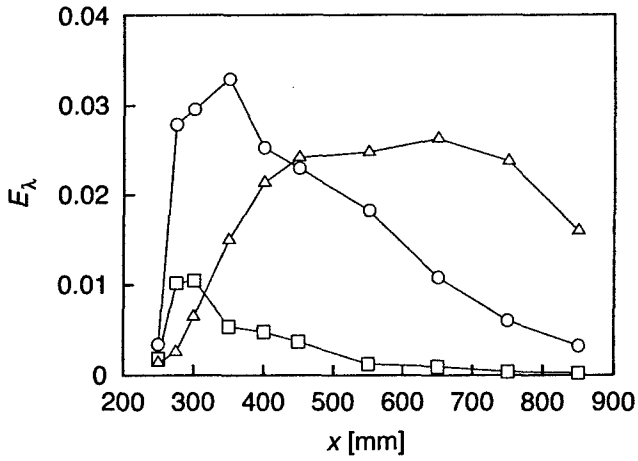

Figure 20: Stationary disturbance energy growth for configuration A. The symbols correspond to E_λ of the 4.16-mm (□), 6.27-mm (○), and 12.31-mm (△) disturbances.

by optimal-disturbance studies. Individual disturbance components reach their respective maxima in the order predicted by the theories (i.e., in the order of increasing wavelength), but all of the maxima observed here occur much farther upstream than is predicted. Table 1 summarizes the locations of the maxima and compares these to Tumin and Reshotko's (2001) calculated optimal disturbances. Tumin and Reshotko's parallel-flow computations are chosen for comparison instead of Andersson et al.'s (1999) or Luchini's (2000) because in both of the nonparallel approaches, the disturbance input location is taken to be the leading edge where the boundary layer thickness is zero and nonparallelism is very important. Perhaps because of this, the nonparallel computations (Andersson et al. 1999; Luchini 2000) put the maxima locations 67% farther downstream than the parallel-flow prediction. The parallel-flow model is clearly more applicable to the present experiment in which the disturbance input occurs well downstream of the leading edge. For configuration A, the boundary layer thickness only grows by about 30% between, $x = 225$ mm, the disturbance input, and $x = 350$ mm, where the strongest disturbance is a maximum.

Configuration B duplicates the physical setup of configuration A but has a lower freestream velocity, 8 m/s, and therefore lower roughness and length Reynolds numbers. Overall, the behavior of this case is nearly identical to the higher Reynolds number configuration. By $x = 350$ mm centerline has only decelerated flow and this persists farther downstream. Spectra indicate that the same three wavelengths, 4.16, 6.27, and 12.31 mm, dominate the disturbance spectrum but that the disturbance amplitudes are significantly lower than those observed for configuration A. Because the disturbance amplitudes are small in this configuration, the growth curves have significantly more scatter than do those in Fig. 20. Nevertheless, the locations of the disturbance maxima can be unambiguously identified. As in configuration A, these maxima occur in the order predicted by theory. Also in agreement with theory, the maxima occur somewhat farther upstream of their higher Reynolds number counterparts, but again, all occur upstream of both the parallel-flow(Tumin and Reshotko 2001) and the nonparallel-flow(Andersson, Berggren, and Henningson 1999; Luchini 2000) predictions (see Table 1).

The third experimental configuration, configuration C, features a freestream speed of 12 m/s and a roughness spacing of 25 mm, twice that of the previous configurations. This setup is included to

Table 1: Transient Energy Growth Maxima Locations.

	Unit Re	
Wavelength	507×10^3 m^{-1}	762×10^3 m^{-1}
4.16 mm		
predicted[a]	292 mm	326 mm
observed	300 mm[b]	300 mm[c]
6.27 mm		
predicted[a]	378 mm	455 mm
observed	300 mm[b]	350 mm[c,d]
8.42 mm		
predicted[a]		641 mm
observed		350–400 mm[d]
12.31 mm		
predicted[a]	815 mm	1113 mm
observed	550 mm[b]	650 mm[c]

[a]The predicted maxima locations are dimensional values calculated for optimal disturbances (Tumin and Reshotko 2001) plus 225 mm, the location of the roughness arrays in the present experiment.

[b]Data from configuration B.

[c]Data from configuration A.

[d]Data from configuration C.

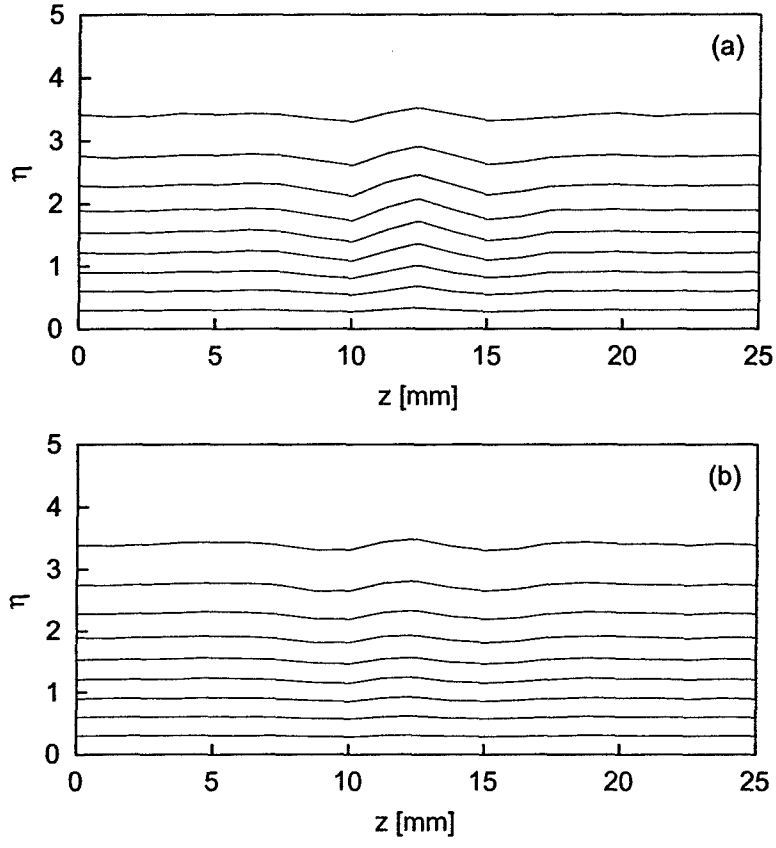

Figure 21: Mean-flow velocity contours for configuration C: $U_\infty = 12$ m/s with a 25-mm-spaced roughness array. Contours are averaged over eight disturbance input wavelengths. Contour lines represent increments of $0.1\,U_\infty$. Plots are shown for (a) $x = 350$ mm and (b) $x = 650$ mm.

produce isolated-roughness behavior while retaining good spectral resolution and the ability to perform phase-locked averaging. Velocity contour plots (Fig. 21) show that the details of the disturbance evolution with the longer-wavelength array are similar to those seen in the previous configurations. The plots suggest that the spanwise extent of the elements' wakes remains very compact far downstream and does not interact with neighboring wakes. This behavior is very different from what would be observed if the streamwise vortices resulted from a modal instability such as the Görtler or cross-flow mechanisms. A unstable mode would produce wave-packet spreading and the most amplified wavelength would fill the entire span at downstream stations.

Disturbance spectra are again obtained at the η locations of maximum U'_{rms} (Fig. 22). The spectra have disturbance peaks at $\lambda = 24.62$, 12.31, 8.42, 6.27, 5.00, and 4.16 mm, corresponding to λ_k, $\lambda_k/2$, ..., $\lambda_k/6$, respectively. All the important wavelenghts grow and decay in the same manner as the previous cases and, once again, reach amplitude maxima in the order of increasing wavelength. A benefit of the wider spacing is that harmonics of the input wavelength are well separated and more disturbance wavelengths can be tracked in spite of the low rms disturbance level. The kinetic energy growth of the total, 6.27-, 8.42-, and 24.62-mm disturbances are given in Fig. 23. The other disturbances show similar growth and decay behavior but are omitted from the figure for clarity. As

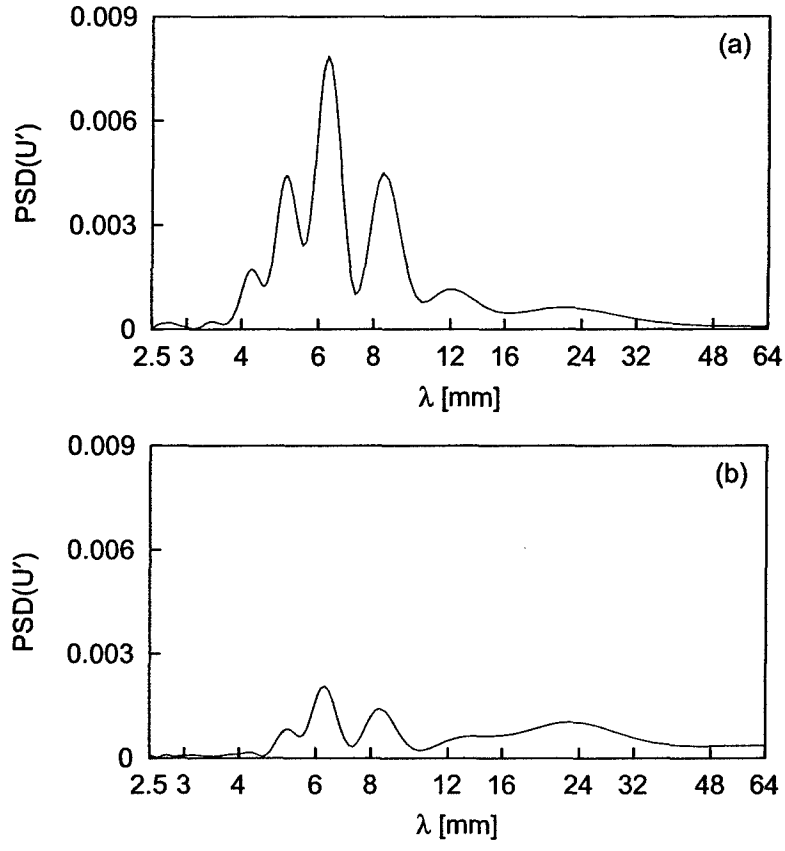

Figure 22: Spanwise-wavelength power spectral density versus spanwise wavelength for configuration A. The curves are obtained at the η for maximum U'_{rms} at each x location. Plots are shown for (a) $x = 350$ mm and (b) $x = 650$ mm.

before, all of the disturbances reach a maximum upstream of the point predicted by theory (see Table 1). A set of abnormally high-amplitude data points exist at $x = 275$ mm. These data are thought to be spurious and are therefore not considered for the summary of disturbance maxima given in Table 1. The 24.62-mm disturbance is not included in the table because it is not clear that it has reached its maximum in the measurement range of the experiment.

Overall, the results of the three configurations are in general qualitative agreement with spatial theories of optimal transient growth (Andersson et al. 1999; Luchini 2000; Tumin and Reshotko 2001). Rapid growth is observed in the region just downstream of the disturbance input and the disturbance kinetic energy appears to grow linearly with streamwise distance. Stationary disturbances are decomposed using a spanwise Fourier transform. The disturbance component with the smallest spanwise wavelength reaches its maximum energy farthest upstream; longer wavelengths reach their maxima in order of increasing wavelength, as predicted. Downstream of their respective energy maxima, each component undergoes slow exponential decay.

The results presented here differ from optimal-disturbance behavior in two important respects. First, the maximum amplitude of the wall-normal disturbance profiles does not occur at $\eta = 2.2$. Second, the point at which the maximum disturbance energy occurs for each wavelength is signifi-

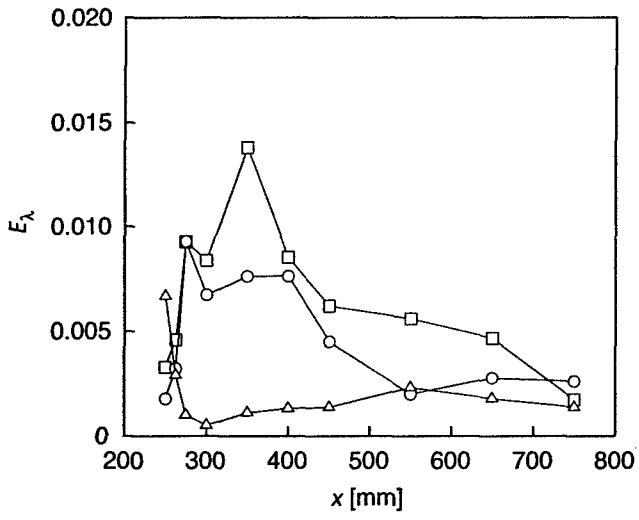

Figure 23: Stationary disturbance energy growth for configuration C. The symbols correspond to E_λ of the 4.16-mm (□), 6.27-mm (○), and 12.31-mm (△) disturbances.

cantly upstream of the point predicted by theory. Regarding the first point, studies with distributed disturbance input (Klebanoff 1971; Reshotko and Leventhal 1981; Kendall 1985; Westin et al. 1994; Matsubara and Alfredsson 2001) appear to agree with the theoretical prediction that the disturbance peak occurs at $\eta = 2.2$, whereas the present study finds $\eta < 2.2$. This is in spite of the fact that the present arrangement, in which a disturbance is introduced and permitted to grow without subsequent energy input, is the actual situation considered by transient growth theories. In this experiment, disturbance peaks are observed to approach $\eta = 2.2$ with increasing downstream distance. White and Reshotko (2002) suggested that movement of the peak would result if the peak location were a function of spanwise wavelength, but the current results show that this is not the case. Furthermore, recent Tumin confirm that the peak's location is not a strong function of wavelength (Tumin, personal communication).

Taken together, the complicated and unpredicted features of the disturbance profiles and their streamwise development may indicate that roughness can excite significantly nonoptimal disturbances. If so, peak's movement might occur as x increases if initially nonoptimal disturbances approach the predicted optimal behavior as the details of the initial disturbance become less important. If confirmed, this would mark another aspect in which transient growth differs from classical modal instabilities. Experimental experience with forced modal instabilities (e.g., T–S waves excited using vibrating ribbons) shows that unstable modes very quickly assume the theoretically predicted disturbance profiles and that the means by which disturbances are generated is not important to the subsequent disturbance evolution. No data obtained here specifically indicate that nonoptimal inputs explain the unexpected behavior, but the fact that existing transient growth theories address optimal disturbances, whereas experiments produce initial disturbances that may not be optimal, should not be overlooked. Differences in disturbance inputs may also explain the difference between the present results and the isolated-roughness studies by Gaster et al. (1994) and Joslin and Grosch (1995).

The other discrepancy between the behavior predicted by optimal disturbance studies and the current results is the location at which maximum transient growth is achieved. In all instances, the experimental maxima occur well upstream of the predicted locations (see Table 1). Surprisingly, the

parallel-flow calculations of Tumin and Reshotko (2001) are in better agreement than nonparallel-flow calculations (Andersson et al. 1999; Luchini 2000). As noted above, this may result from the use of the leading edge as the disturbance input location in the nonparallel-flow studies. At present, it is not clear why the models overpredict disturbance maximum location so significantly. Forthcoming parabolized-stability-equation models that include both nonparallelism and a realistic disturbance input location may improve agreement between theoretical predictions and the results seen here. However, the possibility that the initial disturbances generated by the roughness are not optimal may again strongly influence the behavior observed in the experiment. Nonoptimal disturbances would clearly undergo less growth than optimal disturbances and there is also and indication that they might reach a disturbance maxima farther upstream than their optimal counterparts (see, for example, Tumin and Reshotko's (2001) Fig. 6 that compares stationary and nonstationary $\beta = 0.45$ disturbances). Here again, if the discrepancy between theory and experiment is shown to be due to nonoptimal disturbance inputs, the receptivity of transient disturbances will assume a very important role in understanding transient-growth-induced transition. The importance of receptivity as the mechanism that specifies initial disturbance amplitudes is well recognized for classical instability modes. Similarly, receptivity specifies initial amplitudes for transient disturbances, but the possibility also exists that subsequent growth may depend strongly on how similar initial disturbances are to optimal disturbances; therefore, receptivity might continue to influence disturbance growth very far downstream from where disturbances are initiated.

3.3 Multicomponent measurements of roughness-induced transient disturbances

A critical feature of transient growth is that an initial disturbance (which may or may not be optimal) produces algebraic growth that is different in character than the initial disturbance. This is the idea behind Landahl's (1980) lift-up mechanism; a decaying streamwise vortex (i.e., a v', w' disturbance) generates an algebraically growing u' streak. To establish that this is indeed the case for cylindrical roughness elements that produce transient growth, measurements of the steady U and W velocity fields were obtained in the wake of an array of roughness elements at $x_k = 300$ mm ($x_{\text{vle}} = -7$ mm) with a spanwise spacing of $\lambda_k = 19$ mm, a diameter $d = \lambda_k/3$ and an amplitude of $Re_k = 202$. For these measurements the unit Reynolds number is $Re' = 764 \times 10^3$ m^{-1}. High-spatial-resolution slant-probe hotwire scans are performed that include 38 spanwise steps per λ_k.

Velocity measurements were performed at $x = 310$, 320 and 330 mm. The phase-lock averaged spanwise velocity profiles obtained at these locations are presented in Fig. 24. In each plot, the solid curves represent the spanwise velocity at the location where the curve intersects the plots' abscissa. Positive W velocities are to the right, negative values are to the left and 5% of the freestream speed is indicated by the heavy horizontal line in the upper right corner of each plot. Also included in these plots is the approximate location of roughness element generating the disturbances. Immediately downstream of the roughness at $x = 310$ mm, the spanwise velocity field is non-zero around the downstream of the edges of the roughness. Moving downstream to $x = 320$ mm, the spanwise velocities in these regions increase.

Further downstream at $x = 330$ mm, the spanwise velocity profiles reveal several important features about the origin of roughness-induced transient disturbances. First, it is important to note that the spanwise velocity is zero at the roughness centerline and between the roughness elements which confirms the expected symmertries. W is also zero along both sides of the roughness element. There are two regions on both sides of the roughness centerline that show significant spanwise velocities. These regions are almost perfectly symmetric and terminate exactly at the edge of roughness. On the left-hand-side of the roughness wake, the spanwise velocity value is negative close to the surface,

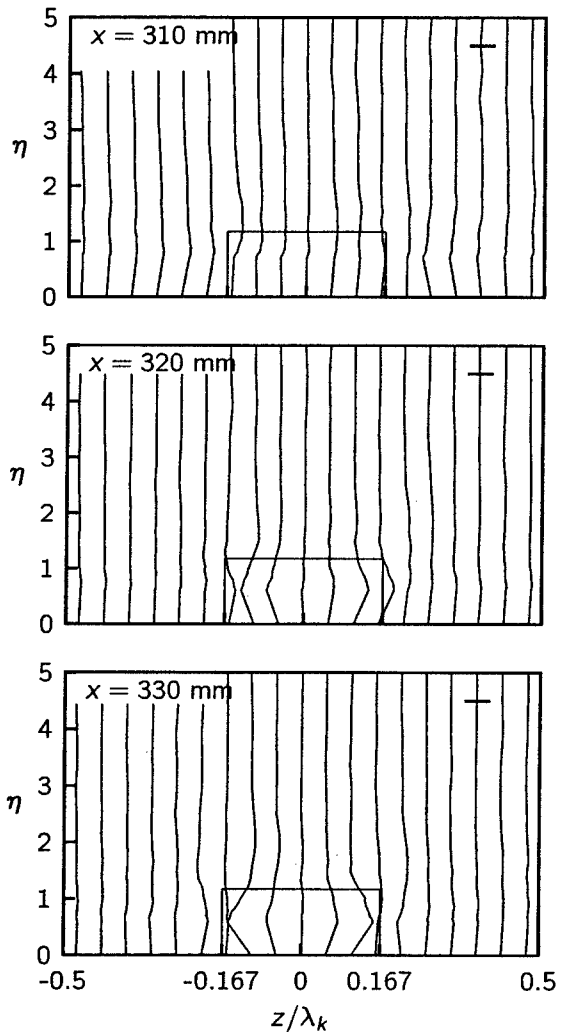

Figure 24: Wall-normal profiles of spanwise velocity for $Re_k = 202$. The rectangular boxes indicate the approximate size and location of the roughness elements and the heavy horizontal line indicates 5% U_∞.

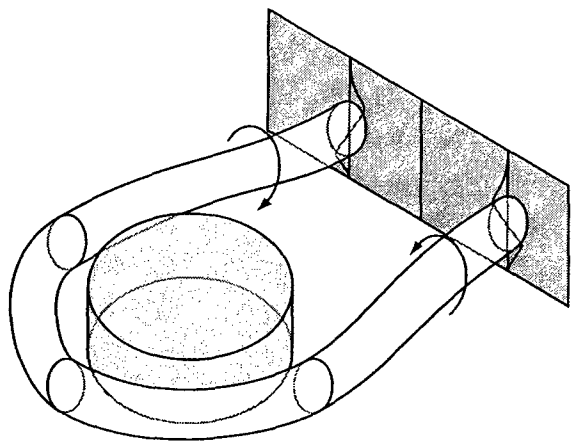

Figure 25: Schematic illustration of the horseshoe vortex about a cylindrical roughness element. The curves on the plane to the right of the figure indicate profiles of the steady spanwise velocity.

below the roughness height, and positive away from the surface, above the roughness height. On the right-hand-side the behavior is the opposite. This is the signature of a counter rotating vortex system with the vortex on the left hand side rotating clockwise and the vortex on the right hand side rotating counter clockwise. The rotation directions suggest that these vortices are the legs of a horseshoe vortex system such as those visualized by Acarlar and Smith (1987) and sketched in Fig. 25. Outside of each leg of the primary horseshoe a second weaker pair of vortices can be observed that rotate in the opposite direction of the primary pair.

It is important to note that at $x = 330$ mm the sense of the primary vortex system's rotation is not consistent with what one might expect from the contour plot of the streamwise U velocities given in Fig. 26. This figure shows that the centerline velocity is decelerated relative to the flow between the roughness elements. However, the rotation of the horseshoe vortex would tend to bring high-momentum fluid toward the wall directly behind the roughness element and produce the opposite effect. In fact, this is exactly what is observed in the far wake both in the current experiment (not shown) and in previous investigations by Kendall (1981) for an isolated element and later in this report for roughness arrays. In the near wake, the deceleration is the result of a small separated region on the roughness elements' downstream side and it takes a considerable streamwise distance for the action of the horseshoe vortex to overcome this and produce accelerated flow along the centerline. This transition from deceleration to acceleration along the centerline has been identified by Tumin and Reshotko (2004) as one cause for the discrepancy between optimal and realizable transient growth. Transient growth of the stationary disturbance can only begin after the primary vortex overcomes the effect of the decellerated flow just downstream of the roughness element.

In summary, the spanwise velocity measurements clearly show a horseshoe vortex system and this supports the notion that roughness-induced transient growth is consistent with Landahl's (1980) lift-up concept. Multicomponent velocity measurements are critical to an improved understanding of realizable transient growth because it is the streamwise-oriented vortex (i.e., the V' and W' disturbances) that is the initiator of transient growth. Future studies will be concentrated on estimating streamwise and spanwise velocity gradients from experimental data and calculating the wall-normal velocity from the continuity equation. This will provide the necessary initial disturbance conditions for computational works and will form the foundation for meaningful growth predictions for physically realizable disturbances.

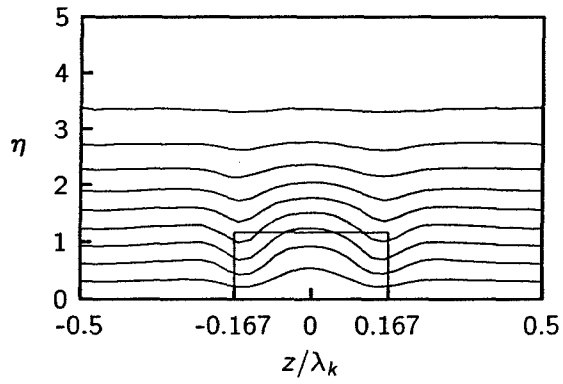

Figure 26: Streamwise velocity contours for $x = 330$ mm, $Re_k = 202$. Contour lines indicate 10% increments of U_∞.

4 Receptivity of Transient Disturbances to Arrays of 3D Surface Roughness Elements

The principal finding of the basic experiments on roughness-induced transient growth is that receptivity plays a significant role in determining the degree of non-optimality of realizable disturbances. This makes the project's second main objective regarding receptivity particularly important and also more complex than initially thought.

The initial complexity of a receptivity model for transient growth relative to exponentially growing modal instabilities arises from the mathematical implications of the differences between the eignenvalue and initial-value approaches for modeling disturbance growth in a boundary layer. For modal disturbances such as TS waves, it is possible to specify a single "receptivity coefficient" that gives the amplitude and phase of a discrete disturbance mode that results from environmental forcing of a particular amplitude, frequency and spanwise wavenumber (Saric et al. 2002). For modal disturbances, the amplitude is specified by the receptivity; the growth or decay rate is an eigenvalue of the stability equations and is independent of receptivity. However, in transient growth problems, the findings of the basic experiments is that receptivity sets the initial disturbance amplitudes as well as the algebraic growth rate and the location of maximum growth by distributing disturbance energy among the decaying modes of the continuous spectrum of eigenmodes.

In order to better understand full range of receptivity effects for roughness-induced transient disturbances a series of receptivity experiments is conducted to further explore the basic behavior established above. These experiments will serves as a step toward developing a rigorous understanding of the receptivity of transient disturbances to surface roughness and to do so in a manner that is compatible with transient growth's representation within linear stability theory. Because the nature of transient growth requires that a receptivity model address both amplitudes and growth rates, it is necessarily more complicated than receptivity of modal disturbances. Details of how this might be approached are given in the following subsection along with the specific objectives of the receptivity experiment.

4.1 Quantifying receptivity of transient disturbances

Both the transient and modal growth mechanisms can be understood in the context of the Orr-Sommerfeld/Squire system. For both types of disturbances, it is typical to consider a particular spanwise wavenumber, β, and frequency, ω, by taking Fourier transforms in time and in the spanwise direction:

$$\mathbf{q}(x,y,z,t) = \frac{1}{4\pi^2}\iint \hat{\mathbf{q}}_{\beta,\omega}(x,y)e^{i(\beta z-\omega t)}\,d\beta\,d\omega \tag{1}$$

where $\mathbf{q} = (u', v', w', p')^T$ and β and ω are real. Next, in the context of parallel-flow boundary layers, a Fourier transform with a complex wavenumber α is applied in the streamwise direction:

$$\hat{\mathbf{q}}_{\beta,\omega}(x,y) = \frac{1}{2\pi}\sum_{p,\omega}\int C_{\alpha(k),\beta,\omega}\,\boldsymbol{\Phi}_{\alpha(k),\beta,\omega}(y)e^{i\alpha(k)x}\,dk + \frac{1}{2\pi}\sum_{j} C_{\alpha_j,\beta,\omega}\,\boldsymbol{\Phi}_{\alpha_j,\beta,\omega}(y)e^{i\alpha_j x}. \tag{2}$$

Here the $\boldsymbol{\Phi}$'s are the suitably normalized eigenmodes (henceforth referred to as OSS modes for Orr–Sommerfeld/Squire) and the $C_{\alpha,\beta,\omega}$ coefficients give the amplitude of each of these modes. The first term is the sum of integrals over the pressure and vorticity branches on the continuous spectrum with real parameter k and the second term is the sum over discrete modes (Grosch and Salwen 1978; Tumin 2003). Because the equations are linear and specific (β,ω) pairs can be considered individually, the subscripts β and ω will be dropped for the remainder of this paper.

For modal instabilities, a single discrete OSS mode has an α_j with a negative imaginary part and this mode grows exponentially in x. The growing mode quickly renders the decaying modes' contribution to the total disturbance negligible and, therefore, to quantify receptivity in this situation, it is sufficient to specify a single complex constant C for the single unstable mode. Computational and experimental approaches to the receptivity of TS waves give C as the product of a complex amplitude and phase of the relevant environmental disturbance (e.g., a freestream acoustic wave) and a complex receptivity coefficient (Saric, Reed, and Kerschen 2002). For transient disturbances, the situation is much more complicated because all of the OSS modes undergo exponential decay and it is their superposition that leads to algebraic energy growth. This means that for any (β,ω) combination, a continuum of coefficients C_α are required — one for each α along the continuous spectrum. Because different distributions of coefficients can result from different initial conditions, a range of growth and decay rates are possible for any combination of the parameters β and ω.

The range of behaviors that are possible for transient growth indicates that it must be approached quite differently than modal instability mechanisms such as TS waves. To address this, Farrell (1988) introduced the concept of an optimal disturbance, the particular initial disturbance that undergoes the largest energy growth in a specified time. Butler and Farrell (1992) extended the concept to 3D disturbances of several canonical 2D basic states and found that, in Blasius boundary layers, the optimal disturbance is a stationary streamwise vortex. The optimal disturbance concept was extended most recently Andersson et al. (1999), Luchini (2000) and Tumin and Reshotko (2001) who considered spatial transient growth in Blasius boundary layers and found that a steady streamwise vortex is the optimal disturbance.

Experimental evidence of transient growth can be found in numerous experiments including both early studies of bypass transition and more recent experiments that have sought to deliberately study transient growth. Freestream turbulence experiments by Westin et al. (1994) and Matsubara and Alfredsson (2001) provide good evidence that transient growth occurs, but the uncontrolled and distributed nature of the disturbance inputs precludes using these experiments to make detailed comparisons between optimal disturbance predictions and experimental results. Therefore, these experiments

are unsuitable as a means of investigating receptivity. To overcome this, the basic experiments reported above included several different spanwise arrays of short cylindrical roughness elements that generated steady disturbances with specific spanwise wavenumbers. The disturbance field was decomposed into spanwise modes equivalent to the streamwise component of $\hat{\mathbf{q}}$ in Eqs. (1) and (2) and the results obtained using this approach showed very clear evidence of algebraic energy growth followed by exponential decay for some, but not all, of the spanwise modes.

The conclusion that can be drawn from the roughness array studies is that receptivity plays a double role in the transient growth process. In addition to setting the amplitude of the initial disturbance, as it does for modal instabilities, receptivity also determines the growth and decay rates of the disturbance. It does this by determining the C_α spectrum which specifies the energy of each of the OSS modes, all of which have different decay rates. The implication is that, because an experimentally realizable disturbance with the same frequency and spanwise wavenumber as the optimal disturbance will not have the optimal C_α spectrum, the realizable disturbance will undergo suboptimal growth and decay.

Ultimately, it will be desirable to use experimental data to generate a spectrum of coefficients, C_α, that correspond to particular experimentally realizable disturbances and to compare the experimentally measured transient growth to numerical predictions of the growth that results from the experimentally generated coefficients. This would provide an unambiguous validation of realizable transient growth theory. Furthermore, work along these lines will clarify which roughness parameters are associated with specific aspects of transient growth.

A method for generating C_α spectra from experimental data has been developed by Tumin(Tumin 2003). Tumin's method involves using the biorthogonality of OSS modes with their adjoints but, unfortunately, requires that the full disturbance field — the three disturbance velocities, the disturbance pressure, and streamwise and wall-normal derivatives of the disturbance velocities — be known as functions of y and z at one x station. In most boundary layer stability experiments, only the streamwise component of the disturbance velocity, u', can be obtained with relative ease. The v' and w' components are more difficult to obtain with reasonable accuracy and the disturbance pressure is probably unmeasurable. Tumin outlines how certain *a priori* assumptions about the form of the disturbance may limit the need for the full disturbance field but, at present, implementing even a reduced form of the biorthogonality calculation remains a daunting task.

As a step toward a rigorous implementation of Tumin's (2003) method, the present work seeks evidence of how different roughness configurations affect the spectrum of continuous modes but does not attempt to calculate the spectrum in a quantitative fashion. The experiments consist of measuring the streamwise component of steady disturbance fields, U', that are produced by different spanwise arrays of 3D roughness elements. The spacing and streamwise location of the different arrays are fixed while the amplitude and diameter of the cylinder-shaped elements are varied. The growth and decay rates of the disturbances produced by these arrays are compared and the results are used to infer possible changes to the continuous spectrum of complex amplitude coefficients.

Two separate series of receptivity experiments are performed. In both series stationary transient disturbances are generated using a spanwise array of cylindrical roughness elements. The array is located at $x_k = 300$ mm with the elements on $\lambda_k = 19$ mm centers. Roughness amplitudes are reported as roughness-based Reynolds numbers, $Re_k = U(k)k/\nu$. The elements' amplitudes and diameters, D, are constant across the array but are varied from experiment to experiment. The elements are constructed from stacked layers of adhesive-backed paper disks.

In the first set of experiments, the amplitude of the roughness elements is varied to observe the effect of roughness amplitude on the growth and decay of the transient disturbance energy. For this

first series of experiments, the roughness elements are 6.35 mm in diameter, $D = \lambda_k/3$, and the roughness amplitudes are $Re_k = 16$, 36, 143, 195, and 254. In the second set of experiments, a range of roughness diameters is examined while the roughness amplitude is held constant at $Re_k = 177$. The diameters used in the second series are $D = 3.81$, 4.76, 5.08, and 7.62 mm or $D = 0.20\lambda_k$, $0.25\lambda_k$, $0.27\lambda_k$, and $0.40\lambda_k$, respectively. Decimal values are used to specify roughness diameters while fractional values are used to specify spanwise disturbance components. This is because all of the important spanwise components of the disturbance energy are harmonics of the roughness spacing, λ_k, but not all of the roughness diameters are. For both series of experiments, the roughness arrays are composed of 16 elements, only eight of which fall within the spanwise measurement range of the hotwire. A summary of the parameters for the two series of experiments is given in Table I.

4.2 Receptivity to roughness height

The first series of experiments consists of varying the amplitude of the roughness array to determine what effect Re_k has on the the amplitude and other characteristics of the resulting transient disturbances. The roughness amplitudes considered here are $Re_k = 16$, 36, 143 and 195. To begin, Figs. 27 and 28 show the effect that $Re_k = 36$ and 195 roughness elements have on the velocity field at $x = 330$ mm, 30 mm downstream of the roughness elements' centers. (This and other x locations are cited with respect to the flat plate's physical leading edge.) The figures consist of contours of the time-averaged streamwise velocity and the wall-normal disturbance profiles. The contour plots show that, at this x location, the flow is accelerated on either side of an element's centerline and is decelerated along the centerline. Upstream of this position, in the immediate wake of the elements, the flow is purely decelerated. Moving downstream from $x = 330$ mm, the amount of deceleration along the centerline decreases and, by $x = 500$ mm, the velocity deficit on the centerline has disappeared but the regions of velocity excess persist and are gradually merging into a single high-speed streak.

Two important comments can be made regarding Figs. 27 and 28. First, the development of the velocity contours and disturbance profiles are qualitatively similar for both configurations. This development — velocity deficit in the near wake, mixed velocity deficit and excess in the intermediate wake region, and velocity excess in the far wake — is exactly what has been observed by Kendall (1981) and others for an isolated cylindrical roughness element. Second, the PSD profiles are all quite similar to one another and to the U'_{rms} profile. (The PSD profiles appear somewhat more narrow than the U'_{rms} profiles because they are energy rather than amplitude measures.)

Moving to quantitative measures of transient growth, Figs. 29–32 give the growth and decay of the disturbance energy components for the fundamental spanwise wavelength, $\lambda = \lambda_k$, and its first three harmonics, $\lambda_k/2$, $\lambda_k/3$ and $\lambda_k/4$. Similar to what was observed above, these four spanwise wavelengths appear very prominently in the power spectrum while wavelengths that are not harmonics of the fundamental contain essentially zero power. Data for the two lowest-amplitude cases, $Re_k = 16$ and 36, are not included because these follow the same trends but cannot be distinguished from zero on these plots.

Figure 29 shows that the disturbance energy contained in the fundamental wavelength λ_k is very high immediately downstream of the roughness element but falls sharply until about $x = 340$ mm. Downstream of $x = 340$ mm, the disturbance energy increases for several hundred millimeters until it reaches a maximum near the downstream end of the measurement domain. Tumin and Reshotko (2004) have noted that if $x = 340$ mm is considered as the initial location, the transient energy growth is quite large and is qualitatively similar to the optimal disturbance whose initial location is $x = 340$ mm. Contrary to what is observed for $\lambda = \lambda_k$, Fig. 30 shows that the $\lambda_k/2$ component does

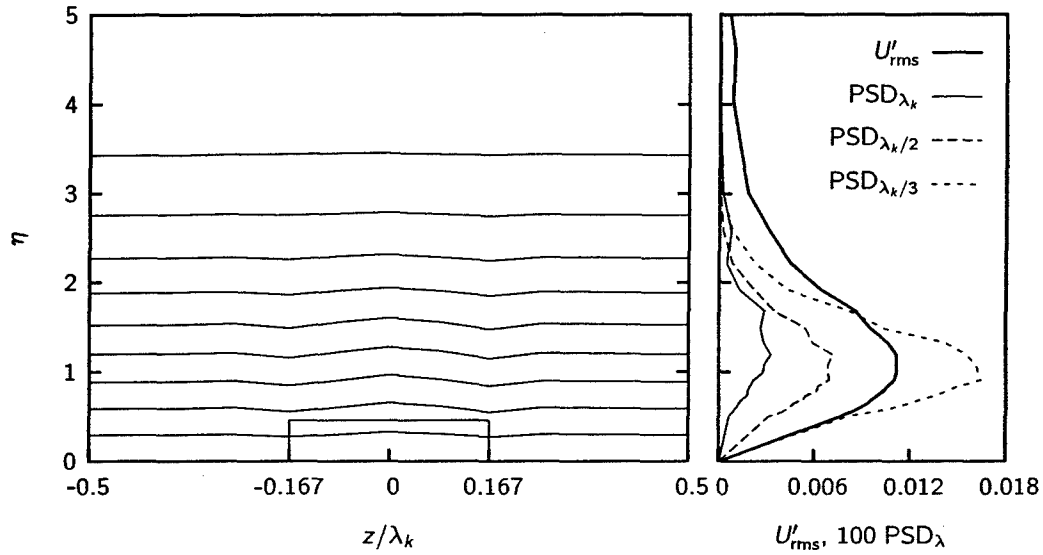

Figure 27: Streamwise velocity contours (left) and disturbance profiles (right) obtained at $x = 330$ mm for $Re_k = 36$, $D = 0.33\,\lambda_k$ roughness elements. Contour lines are 10% increments of U_∞. The rectangle in the contour plot indicates the approximate location, height and diameter of the roughness elements.

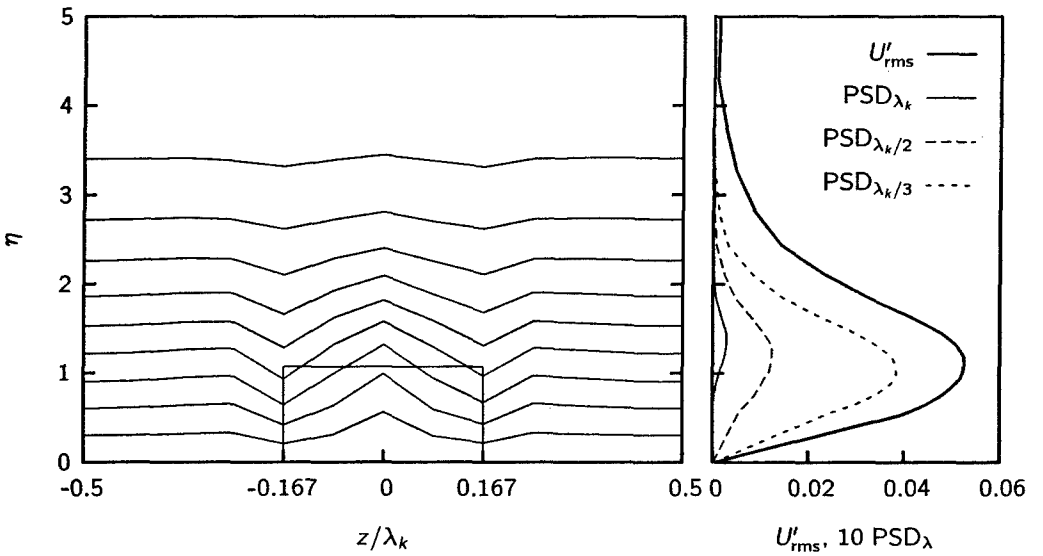

Figure 28: Streamwise velocity contours (left) and disturbance profiles (right) obtained at $x = 330$ mm for $Re_k = 195$, $D = 0.33\,\lambda_k$ roughness elements. Contour lines are 10% increments of U_∞. The rectangle in the contour plot indicates the approximate location, height and diameter of the roughness elements.

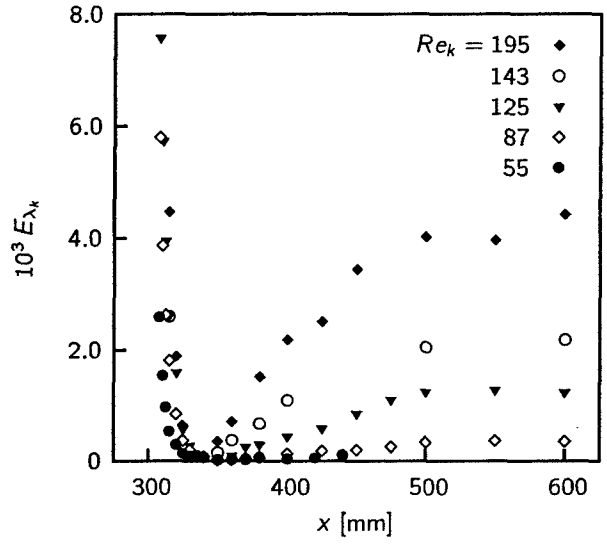

Figure 29: Variation in the λ_k component of disturbance energy across varying Re_k for $D = 0.33\,\lambda_k$ roughness elements.

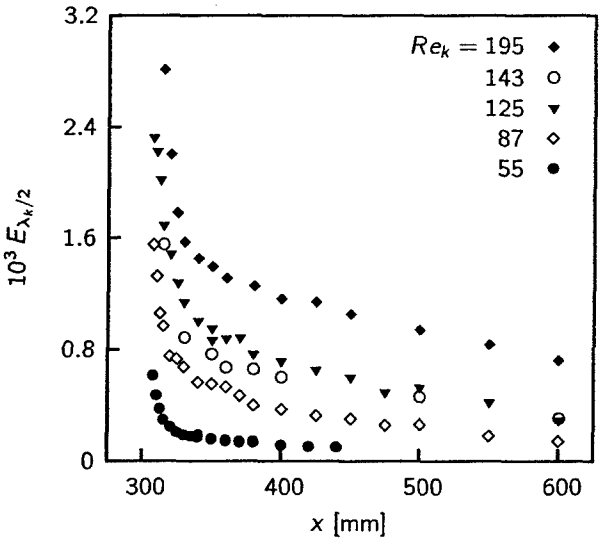

Figure 30: Variation in the $\lambda_k/2$ component of disturbance energy across varying Re_k for $D = 0.33\,\lambda_k$ roughness elements.

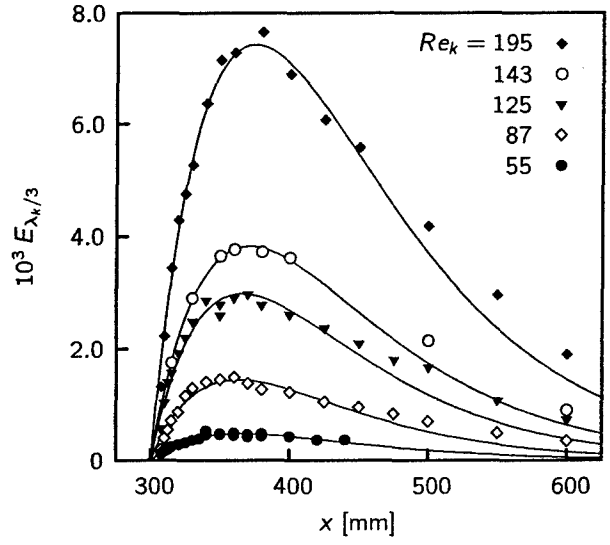

Figure 31: Variation in the $\lambda_k/3$ component of disturbance energy across varying Re_k for $D = 0.33\,\lambda_k$ roughness elements. The curves are best fits to Eqn. (4) using data obtained upstream of $x = 475$ mm.

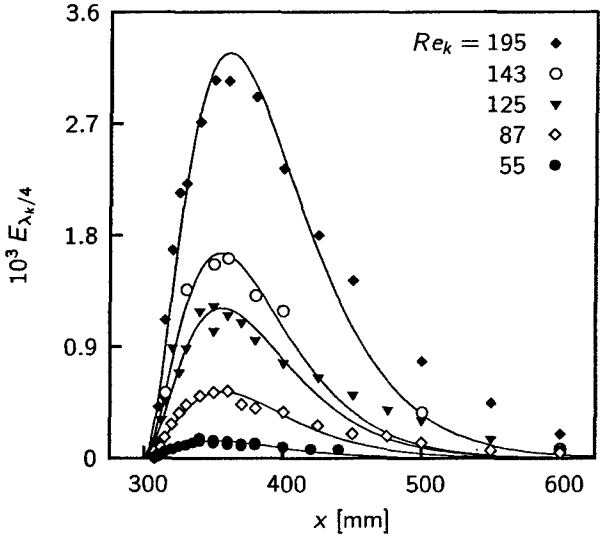

Figure 32: Variation in the $\lambda_k/4$ component of disturbance energy across varying Re_k for $D = 0.33\,\lambda_k$ roughness elements. The curves are best fits to Eqn. (3) using data obtained upstream of $x = 475$ mm.

not undergo any growth. This wavelength contains significant disturbance energy in the near wake but its energy decays monotonically throughout the measurement domain.

The $\lambda_k/3$ and $\lambda_k/4$ disturbances exhibit quite different behavior than the longer wavelengths. Figures 31 and 32 show that these disturbance components grow algebraically with x from the roughness location, reach a maximum and then decay. The growth and decay of $E_{\lambda_k/4}$ in Fig. 32 is fit to a transient growth model function

$$E_{\lambda_k/4}(x) = a_2 (x - x_k)^2 \exp[-(x - x_k)/b] \tag{3}$$

that is similar to one suggested by Boberg and Brosa (1988). The model function's parameter a_2 represents both the disturbance energy scaling and the algebraic growth rate. The parameter b represents an exponential decay length and could be thought of as the inverse of the spatial decay rate, α_i, of the slowest-decaying OSS mode that contributes to the transient disturbance. Alternatively, the model function represented in Eqn. (3) has its maximum at $x = x_{max}$ where $x_{max} - x_k = 2b$ so b is also representative of the distance over which the disturbance grows before the lift-up effect that increases the disturbance energy becomes less significant than viscous decay.

The best fit of the Eq. (3) model function to the $E_{\lambda_k/4}$ data is represented in Fig. 32 as a solid line for each Re_k. The function provides an excellent fit in the early growth and peak disturbance regions but does not follow the data at the most downstream locations. Therefore, to correctly capture the initial growth rates and the locations of the energy maxima, only data obtained upstream of $x = 475$ mm are included in the fit.

The growth of $E_{\lambda_k/3}$ shown in Fig. 31, although qualitatively similar to $\lambda_k/4$, requires a different model function for satisfactory fits. For the $\lambda_k/3$ data, the quadratic-growth model function of Eq. (3) results in too narrow a peak near x_{max} and significantly over estimates the maximum energy observed in the data. Instead, a similar fitting function with linear rather than quadratic energy growth given by

$$E_{\lambda_k/3}(x) = a_1 (x - x_k) \exp[-(x - x_k)/b] \tag{4}$$

is appropriate. This model has $x_{max} - x_k = b$. The linear dependance on x leads to somewhat faster growth in the immediate wake of the roughness array and a broader, lower peak near the energy maximum relative to the quadratic-growth model. These features are all observed in the data for the $\lambda_k/3$ component. For both the $\lambda_k/3$ and $\lambda_k/4$ data, fits to Eq. (3), Eq. (4) and mixed linear/quadratic models were attempted but it is clear that either a linear or quadratic model, not the mixed model, is appropriate in both cases. As for the $\lambda_k/4$ data, only the $\lambda_k/3$ data obtained upstream of $x = 475$ mm is included so that the initial growth and peak regions are emphasized.

It is somewhat surprising that the $E_{\lambda_k/3}$ data is described so well by the linear growth model of Eq. (4). Simple model systems of transient growth such as the one presented by Boberg and Brosa (1988) show that quadratic energy growth along the lines of that shown by the $E_{\lambda_k/4}$ data and Eq. (3) are to be expected. Linear growth should be expected of the disturbance amplitude, not the energy. Despite this, the linear growth model of Eq. (4) provides excellent fits to the $E_{\lambda_k/3}$ data throughout its growth and energy maximum regions while the quadratic growth model of Eq. (3) overestimates the energy maximum and produces too narrow a peak about the maximum. Although the mechanism responsible for the different behaviors is not known, the differences among all four of the disturbance wavelengths only serve to emphasize the importance of the receptivity process in determining the suboptimality of each disturbance component.

The model functions are obviously not a rigorous representation of spatial transient growth nor do they provide a means of determining the coefficients C_α that are the most appropriate measures of

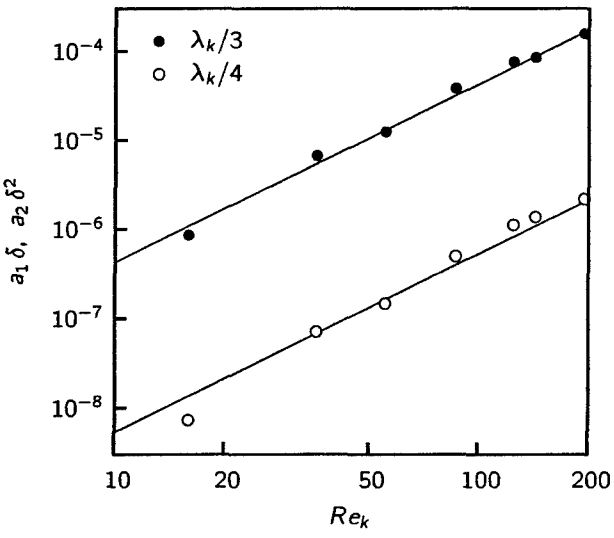

Figure 33: Variation of the fit parameters a_1 and a_2 with Re_k. The parameters are nondimensionalized by the boundary layer thickness, δ, or δ^2 at $x = 300$ mm, respectively.

transient growth receptivity. However, the parameters a_1, a_2 and b do provide a means of quantifying certain aspects of the growth and enable the role of different roughness features to be assessed in a systematic way. If a change in roughness parameters only affects a_1 or a_2 this suggests that the coefficients C_α have all been multiplied by the same constant and that the transient growth behavior is unchanged except that it occurs at a different disturbance amplitude. However, if a change of roughness parameters increases or decreases b, this suggests that disturbance energy has been redistributed among the OSS modes and that a somewhat different superposition of modes has led to the observed transient growth.

The dependence of the parameters a_1, a_2 and b on Re_k is given in Figs. 33 and 34. Figure 33 shows very clearly that the a coefficients scale quadratically with Re_k across a wide range of roughness amplitudes. In the figure, a_1 and a_2 are nondimensionalized using the boundary layer thickness at the roughness location or this value squared to give the algebraic growth rate in units of δ or δ^2, respectively, rather than inverse millimeters or inverse millimeters squared. Error bars are not plotted because these are roughly the size of the symbols. Taking the quadratic fitting functions to be $a_1\,\delta = A_1\,Re_k^2$ and $a_2\,\delta^2 = A_2\,Re_k^2$, the coefficient $A_1 = (4.3 \pm 0.2) \times 10^{-9}$ for $\lambda_k/3$ and $A_2 = (5.3 \pm 0.6) \times 10^{-11}$ for $\lambda_k/4$.

At the outset of this work, the expectation was that changing the roughness amplitude would increase the amplitude of the resulting disturbances but not affect other aspects of their development. However, the data in Fig. 34 show that the extent of transient growth, $x_{max} - x_k$, also increases with Re_k, albeit weakly. The uncertainties on the growth-length estimates are significant relative to the variation in the parameter across the Re_k range but the trend is clear. Again, the implication is that the different roughness amplitudes are producing somewhat different distributions of disturbance energy among the continuous OSS modes. As Re_k increases, it appears as if more slowly decaying modes contain progressively larger fractions of both the $\lambda_k/3$ and $\lambda_k/4$ disturbances' energy.

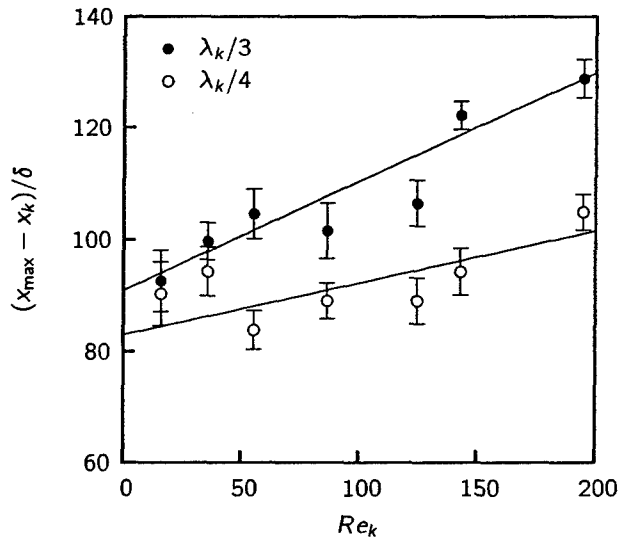

Figure 34: Variation of the growth length $x_{max}-x_k$ with Re_k. The growth length is nondimensionalized by the boundary layer thickness, δ, at $x = 300$ mm. The solid lines represent least squares fits to a line.

Considering Eqs. (3) and (4) and the dependance of $E_{\lambda_k/3}$ and $E_{\lambda_k/4}$ on Re_k through the parameters a_1 or a_2 and b, it is clear that the sets of $E_{\lambda_k/3}$ and $E_{\lambda_k/4}$ curves can both be collapsed to a single curve for each λ by scaling each by Re_k^2. The collapse is not perfect because the energy maximum shifts downstream slightly as the parameter b increases with Re_k, but this amounts to very little when compared to the a parameters' Re_k^2 scaling that changes by a factor of nearly 150 across the range of roughness heights considered in the experiment. In fact, Fig. 35 illustrates that when $E_{\lambda_k/3}$ is scaled by Re_k^2, the variability of the data almost completely masks the growth-length increase. (This figure also indicates that at $Re_k = 16$ the energy is somewhat less than expected using the Re_k^2 scaling and this may indicate that the $Re_k = 16$ roughness elements do not have such pronounced nonlinear receptivity as the other roughness arrays.) The longer-wavelength disturbance components, λ_k and $\lambda_k/2$ also scale as Re_k^2 across the entire Re_k range considered in the experiment. These components do not lend themselves to an obvious model function but simply plotting the disturbance energies divided by Re_k^2 (Figs. 36 and 37) indicates a collapse to a single curve in each case with about the same level of variability as is observed in Fig. 35.

The roughness-amplitude experiments provide evidence that the C_α spectrum is strongly affected by roughness parameters. In these experiments the λ_k disturbance component decays rapidly and then undergoes transient growth; the $\lambda_k/2$ disturbance component undergoes monotonic decay; and the $\lambda_k/3$ and $\lambda_k/4$ disturbance components undergo immediate transient growth but do so linearly with x and quadratically with x, respectively. In all cases, E_λ is observed to scale nearly as Re_k^2 between Re_k values of 16 and 195. However, the the model functions for the $\lambda_k/3$ and $\lambda_k/4$ components show that the streamwise length over which these disturbances grow is a weakly increasing function of Re_k and this makes a small impact on the energy scaling with Re_k. Additionally, the increase in the growth length implies that as Re_k is increased, OSS modes with progressively slower decay rates are being excited by the roughness and, in some sense, the disturbances are approaching optimality.

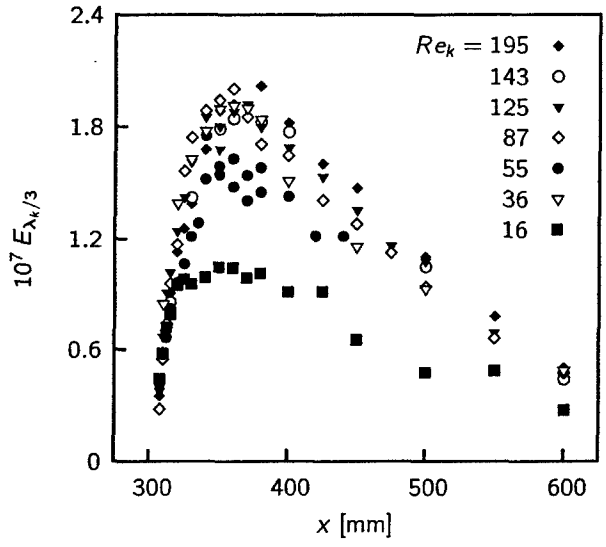

Figure 35: Variation in the $\lambda_k/3$ component of disturbance energy across varying Re_k for $D = 0.33\,\lambda_k$ roughness elements. The energies are scaled by Re_k^2.

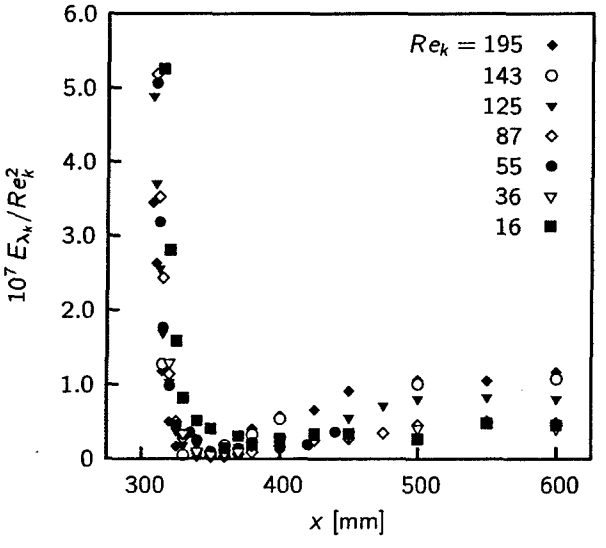

Figure 36: Variation in the λ_k component of disturbance energy across varying Re_k for $D = 0.33\,\lambda_k$ roughness elements. The energies are scaled by Re_k^2.

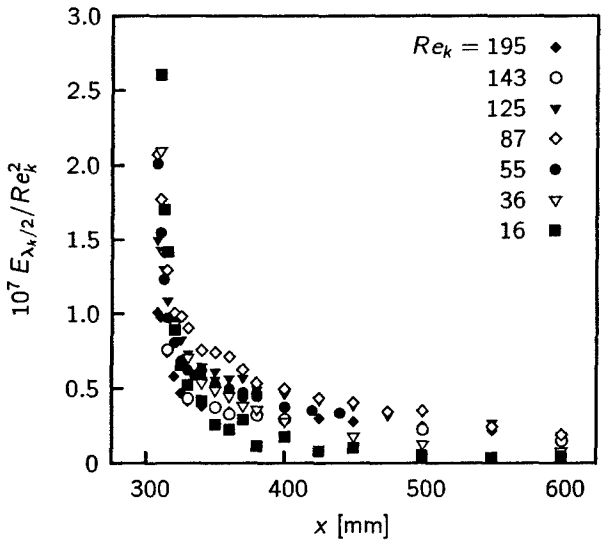

Figure 37: Variation in the $\lambda_k/2$ component of disturbance energy across varying Re_k for $D = 0.33\,\lambda_k$ roughness elements. The energies are scaled by Re_k^2.

The feature of the receptivity mechanism that is responsible for this shift toward longer growth and slower decay is not known at present. One possibility is that as the roughness amplitude is increased, the slightly different shapes associated with the roughness elements' increasing height-to-diameter aspect ratio excite slightly different distributions of OSS modes. Another possibility is that the increasing roughness amplitudes lead to increasingly strong nonlinear effects in the immediate vicinity of the roughness and it is these nonlinear effects that excite different collections of OSS modes. The transient growth is not thought to include significant nonlinear effects but the receptivity process almost certainly does because the height of the roughness elements exceeds the boundary layer's lower-deck thickness even for $Re_k = 16$. The variety of behaviors exhibited by the various spanwise wavelengths also indicates that the spanwise modes vary widely in terms of their degree of suboptimality.

4.3 Receptivity to roughness diameter

The finding that the height-to-diameter ratio may play a role in distributing energy among the continuous OSS modes prompted the second series of experiments in which four roughness diameters were considered while the roughness amplitude was held fixed at $Re_k = 177$. The roughness diameters ranged from $D = 3.81$ mm $(0.2\lambda_k)$ to 7.62 mm $(0.4\lambda_k)$. The diameter used in the roughness-amplitude experiment, $D = 6.35$ mm $(0.33\,\lambda_k)$ was not reconsidered in the second series of experiments because these data can be reliably scaled from the $Re_k = 143$ and 195 cases of the first series.

As the roughness diameter is increased from its smallest value the most obvious effects on the resulting disturbances are an increase in the total disturbance energy as the amount of obstruction to the flow is increased and, simultaneously, a shift of the energy distribution toward the longer spanwise disturbance components. Both of these effects are visible in Figs. 38 and 39. These figures show

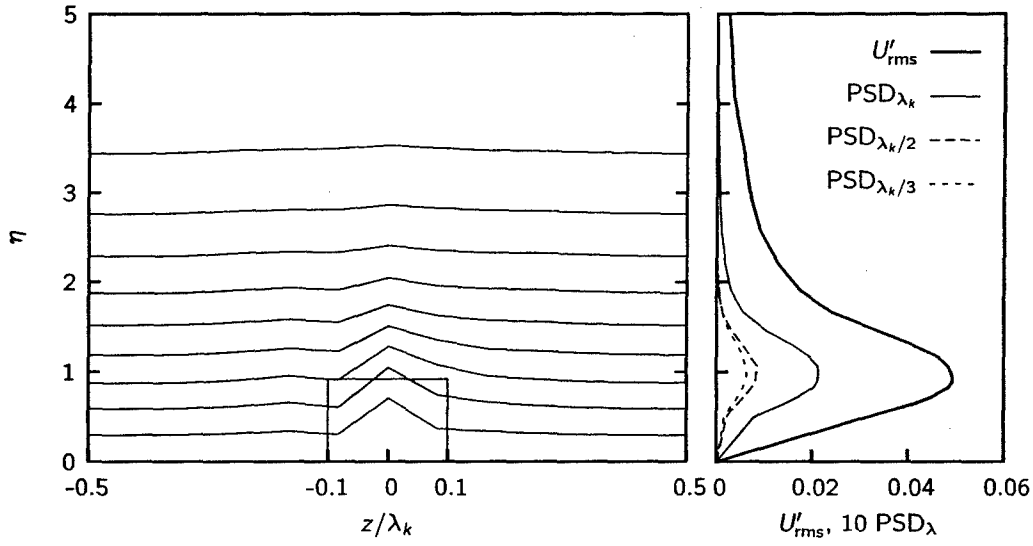

Figure 38: Streamwise velocity contours (left) and disturbance profiles (right) obtained at $x = 310$ mm for $Re_k = 177$, $D = 0.20\,\lambda_k$ roughness elements. Contour lines are 10% increments of U_∞. The rectangle in the contour plot indicates the approximate location, height and diameter of the roughness elements.

the velocity contours and disturbance profiles at $x = 310$ mm for the smallest and largest roughness diameters, $D = 3.81$ and 7.62 mm, respectively. Comparing the two figures, the U'_{rms} profiles are nearly identical except for their amplitudes which mirror the diameters of the roughness elements. Comparing the distribution of the disturbance energy among the constituent spanwise modes, the 3.81-mm-diameter roughness has a much smaller difference between the λ_k and $\lambda_k/3$ components than the 7.62-mm-diameter roughness whose λ_k component dominates the power spectrum.

The increasing total disturbance amplitude and simultaneous shift toward longer-wavelength components manifests itself clearly in the transient growth of E_{λ_k}. Figure 40 shows that as the diameter is increased, the disturbance energy of the λ_k component increases significantly. The energy may reach a maximum near $D = 0.33\,\lambda_k$ and decrease somewhat for larger diameters. However, the single case with $D = 0.40\,\lambda_k$ is insufficient to conclusively support this possibility. Besides the uniform increase in E_{λ_k} with roughness diameter, the diameter does not appear to affect the qualitative details of the evolution. For all diameters, the energy decreases rapidly for a short distance, reaches a minimum near $x = 340$ mm and then undergoes transient growth.

The situation is quite different for $E_{\lambda_k/2}$. The roughness-amplitude experiments that used $D = 0.33\,\lambda_k$ roughness elements had this component exhibiting monotonic energy decay. However, Fig. 41 shows that monotonic decay is actually unique to that diameter. The smaller-diameter roughness elements produce a qualitative behavior that is very similar to what is observed for λ_k, rapid decay until about $x = 340$ mm and then transient growth. Surprisingly, among the three shortest wavelengths, the disturbance energy decreases with increasing roughness diameter, the opposite of the trend observed for the λ_k component. The largest diameter, $D = 0.40\,\lambda_k$, produces rapid decay of $E_{\lambda_k/2}$ until about $x = 325$ mm, an energy plateau that extends until about $x = 425$ mm and slow decay beyond that point. The variety of behaviors exhibited by $E_{\lambda_k/2}$ in response to the different roughness diameters

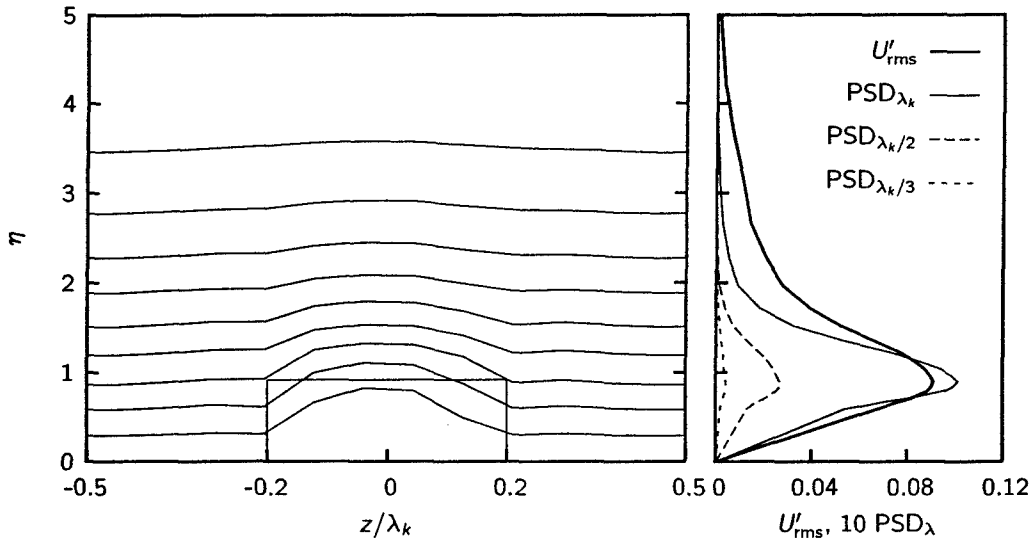

Figure 39: Streamwise velocity contours (left) and disturbance profiles (right) obtained at $x = 310$ mm for $Re_k = 177$, $D = 0.40\,\lambda_k$ roughness elements. Contour lines are 10% increments of U_∞. The rectangle in the contour plot indicates the approximate location, height and diameter of the roughness elements.

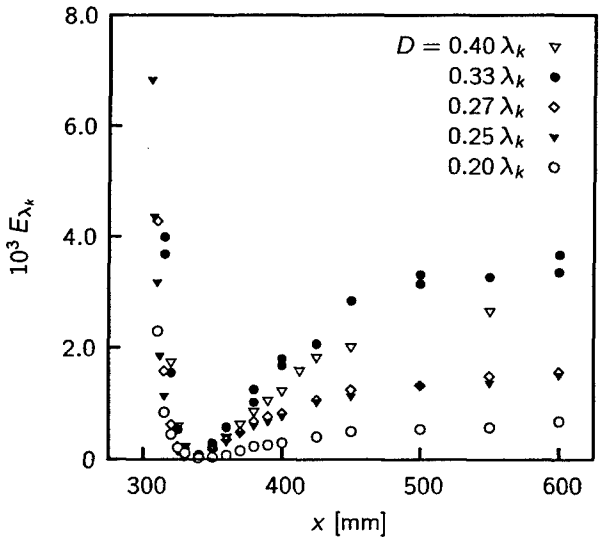

Figure 40: Variation in the λ_k component of disturbance energy across varying roughness diameter for $Re_k = 177$ roughness elements. The $D = 0.33\,\lambda_k$ data are scaled from the $Re_k = 143$ and 195 cases of Fig. 29.

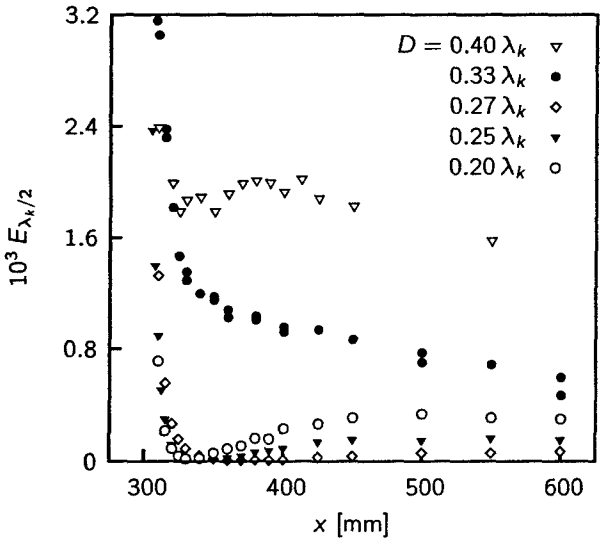

Figure 41: Variation in the $\lambda_k/2$ component of disturbance energy across varying roughness diameter for $Re_k = 177$ roughness elements. The $D = 0.33\,\lambda_k$ data are scaled from the $Re_k = 143$ and 195 cases of Fig. 30.

is striking, especially considering that these changes are triggered by diameter changes that are very small fractions of the roughness spacing. Again, the implication is that as the roughness diameter is changed, very different collections of C_α coefficients are used to represent the $\lambda_k/2$ disturbance. Some lead to transient growth while others do not.

The behavior of the $\lambda_k/3$ disturbance component is given in Fig. 42. This data and especially the region just aft of the roughness array that is highlighted in Fig. 43 shows a variety of behaviors similar to the $\lambda_k/2$ disturbance. For $\lambda_k/3$, there is strong and immediate transient growth for the $D = 0.33\,\lambda_k$ and $0.40\,\lambda_k$ roughness elements. The shorter wavelengths undergo a brief initial decay and then show a trend toward reduced disturbance growth as the roughness diameter is decreased until the $D = 0.20\,\lambda_k$ case results in monotonic decay. The evolution of $E_{\lambda_k/4}$ is not shown but exhibits similar behavior. In that case, the $D = 0.40\,\lambda_k$ roughness leads to monotonic decay; the three intermediate diameters, $0.33\,\lambda_k$, $0.27\,\lambda_k$, and $0.25\,\lambda_k$, all lead to fairly strong, immediate transient growth; and the shortest wavelength, $0.20\,\lambda_k$, leads to significantly weaker growth.

As for the roughness-amplitude experiments, the roughness-diameter experiments provide additional information on the role of receptivity. In these experiments, only the λ_k disturbance's evolution is consistent across the roughness diameters considered. The other three spanwise modes, $\lambda_k/2$, $\lambda_k/3$, and $\lambda_k/4$, all exhibit two or three of the observed types of behavior: monotonic decay, immediate transient growth, or initial decay followed by transient growth.

Once again, the variations in the qualitative nature of the transient growth indicate that very small changes in the roughness parameters can lead to significant changes in the spectrum of C_α coefficients that represent the amplitudes of the continuous spectrum of OSS modes. This sensitivity is probably associated with the nonlinearities of the receptivity mechanism because such an effect would not be observed if the receptivity was linear and the energy of each spanwise mode was proportional to that

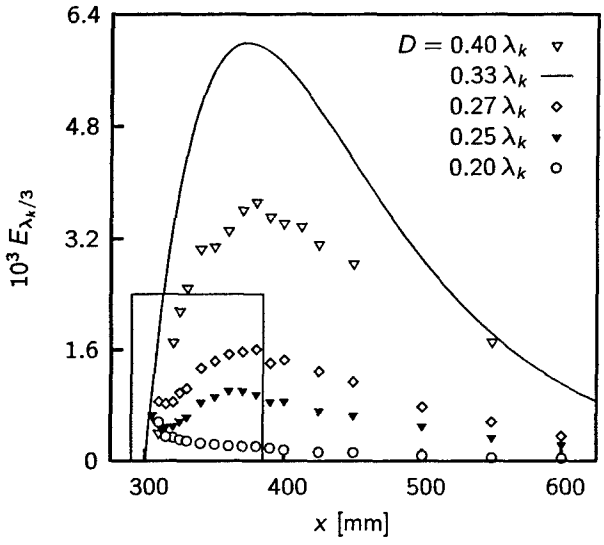

Figure 42: Variation in the $\lambda_k/3$ component of disturbance energy across varying roughness diameter for $Re_k = 177$ roughness elements. The $D = 0.33\,\lambda_k$ curve uses parameters obtained from the least-squares fits of Figs. 33 and 34. The boxed region is expanded in Fig. 43.

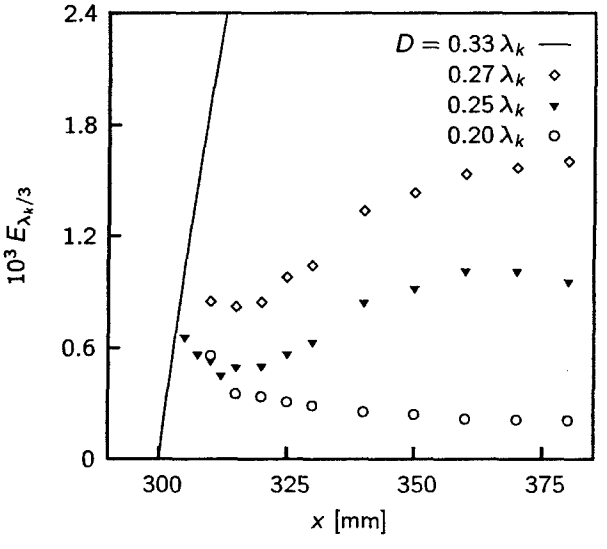

Figure 43: Detailed view of the boxed region of Fig. 42.

mode's contribution to the spanwise roughness spectrum. In the future, it is hoped that the specific receptivity mechanism that distributes energy among the OSS modes will be determined and that calculations of the coefficients can be compared directly to experimental measurements. A successful match between the theoretical and experimental spectra would then permit correct predictions of the transient growth of physically realizable disturbances.

5 Unsteady Disturbances and Bypass Transition

All of the experiments described in the preceding sections involve disturbances generated by 3D roughness elements that are of sufficiently low amplitudes that they do not lead to significant vortex shedding or immediate transition in the roughness elements' wakes. However, an equally important area of study involves transition behavior of flows that interact with larger-amplitude roughness elements. Prior to the development of transient growth theory the role of isolated and distributed 3D roughness has not been as well understood on a theoretical basis because the stationary, spanwise varying disturbances created by 3D roughness are not unstable within the context of a normal-mode stability analysis (Reshotko 2001). Typically, transition in the wake of isolated 3D roughness elements is predicted using correlations based on a critical roughness-based Reynolds number, $Re_{k,\mathrm{crit}}$, established in the 1950's (Dryden 1959; Smith and Clutter 1959; Tani 1961; von Doenhoff and Braslow 1961; Tani 1969; Sedney 1973). Within the context of the correlation approach, if a roughness element exceeds $Re_{k,\mathrm{crit}}$ transition is expected to occur at or just aft of the roughness element but if the critical value is not exceeded then no effect is expected.

The correlation approach based on a critical Re_k is well established but provides no guidance on the more-subtle effects that subcritical 3D roughness can have on the behavior of a laminar boundary layer. For instance, a particularly interesting recent finding by Cossu and Brandt (2002, 2004) is that finite-amplite optimal disturbances can suppress the growth of TS-like disturbances in a boundary layer. In Cossu and Brandt's numerical studies, spanwise-invariant disturbances in the TS-unstable frequency are introduced into a boundary layer that is modulated by stationary, spanwise-periodic optimal disturbances. As the amplitude of the transient disturbances is increased, the unsteady TS-like disturbances become increasingly modulated in the spanwise direction and experience progressively slower growth in the streamwise direction. Once the amplitude of the transient disturbances reaches about $0.2U_\infty$ at their maximum-growth location, the unsteady disturbance growth is completely suppressed. The implication is that it may be possible to use spanwise arrays of 3D roughness elements to passively delay or suppress TS-dominated transition. This control approach would be similar in appearance to the crossflow-dominated transition control approach using subcritically spaced roughness elements developed by Saric, Carrillo, and Reibert (1998) but would be quite different in terms of the instability mechanisms involved.

Implementing the control approach inspired by Cossu and Brandt's (2002, 2004) calculations involves introducing the largest possible stationary transient disturbances because as the transient disturbances' amplitudes are increased there is progressively less TS growth. However, the means of introducing the stationary disturbances — placing arrays of 3D roughness elements on the surface — will itself lead to transition if the roughness elements' amplitudes exceed $Re_{k,\mathrm{crit}}$. Another danger is that the stationary transient disturbances may become unstable to a high-frequency secondary instability once their amplitude exceeds 26% of the freestream speed (Andersson et al. 2001). Therefore, there is considerable uncertainty as to whether the approach is feasible.

In an effort to better understand the limitations on implementing Cossu and Brandt's control approach, the final series of experiments covered by this report aims to investigates the mechanisms

associated with the transient growth of stationary disturbances or the rapid transition associated with spanwise arrays of large-amplitude 3D roughness elements. The focus is on obtaining detailed measurements of the steady and unsteady flow in the elements' wakes. This data is used to assess the mechanism associated with immediate transition and to determine what role, if any, transient growth of stationary disturbances or the secondary instability of these disturbances may play in this transition scenario. In the following subsections a brief review of the literature on the role of isolated 3D disturbances is presented and the experimental results are presented and discussed.

5.1 Review of experiments on isolated surface roughness effects

The role of isolated 3D roughness elements was initiated in the 1950's by the flow visualization studies of Gregory and Walker (1950) who established a basic understanding of the horseshoe and hairpin vortex structure that exists around a moderate- to large-amplitude roughness element in a boundary layer. Gregory and Walker's results have been enhanced by numerous other flow-visualization studies that culminate with the experiments of Acarlar and Smith (1987). These lead to the conclusion that the topology of the flow about an isolated 3D roughness element in a boundary layer consists of a steady horseshoe vortex that wraps around the upstream side of an isolated roughness element and trails two steady counter-rotating legs downstream. The sense of rotation is such that along the line directly behind the roughness element the vertical velocity induced by the vortices is directed down toward the surface. At sufficiently high values of Re_k, unsteady hairpin vortices originate periodically from the separated region just aft of the roughness element. The heads of these vortices moves up and away from the roughness element and are convected downstream. Acarlar and Smith show that shedding originates from hemispherical roughness elements at around $Re_k \approx 120$ and that a Strouhal number based on the shedding frequency, roughness height, and the velocity at the roughness height, $St = fk/u(k)$, increases from below $St = 0.05$ at the lowest Re_k values that produce shedding to values between $St = 0.2$ and 0.4 as Re_k exceeds 1200 (Acarlar and Smith 1987). Hotwire measurements by Klebanoff et al. (1992) give similar results but Klebanoff et al. cast their data in terms of a Strouhal number based on displacement thickness, $St = f\,\delta^*/u(k)$, and find that $St \approx 0.3$ from $Re_k = 300$ to 1700 for hemispherical roughness elements. Klebanoff et al. further find that cylindrical elements with $d = k$ are found to produce somewhat lower Stouhal numbers that increase slightly from $St \approx 0.2$ at $Re_k = 400$ to $St \approx 0.25$ at $Re_k = 1200$.

Regarding $Re_{k,\mathrm{crit}}$, the critical roughness-based Reynolds number for immediate roughness-induced transition, the general finding is that the effect of isolated 3D roughness elements is "more critical" than 2D roughness strips. By "more critical" it is meant that that as $Re_{k,\mathrm{crit}}$ is exceeded the transition location moves forward very rapidly but that below $Re_{k,\mathrm{crit}}$, an isolated 3D element has little or no effect on transition (Dryden 1959; Smith and Clutter 1959; Tani 1961; von Doenhoff and Braslow 1961; Tani 1969; Sedney 1973). This is quite different than the behavior of boundary layers with 2D roughness that tend to show transition gradually moving forward with increasing Re_k. Studies originating with those by Klebanoff et al. (1955) establish that $Re_{k,\mathrm{crit}}$ lies between 600 and 900 for elements whose height-to-diameter ratio is approximately unity. The most recent and detailed studies of $Re_{k,\mathrm{crit}}$ are also by Klebanoff et al. (1992) who find somewhat lower values of $Re_{k,\mathrm{crit}}$ than previous studies (e.g., Tani et al. 1962) but have a somewhat less-stringent definition of transition. A key finding of by Klebanoff et al. (1992) is that even at limiting cases of high Re_k, there is always a finite distance between the roughness element and the resulting turbulent flow. The implication is that at high Re_k's transition occurs as the result of an instability of the distorted, reversed flow in the roughness element's wake that requires some finite distance to develop. Other key findings of the early transition correlation work are that $Re_{k,\mathrm{crit}}$ scales roughly as $(k/d)^{2/5}$ meaning that transition

occurs for progressively lower $Re_{k,\mathrm{crit}}$ values as the roughness diameter is increased (von Doenhoff and Braslow 1961; Tani 1969) and that elements in spanwise arrays behave as isolated elements when their spacing is three times their diameter or larger (von Doenhoff and Braslow 1961).

While transition correlations are useful, they do not reveal the detailed mechanism for transition nor do they assist in designing transition control strategies besides simply placing design limits on acceptable roughness levels. This requires detailed flow studies that can be used in conjunction with stability theories. However, there have been relatively few studies of the detailed flow field in the wake of isolated roughness elements that can be used to inspire or validate mechanisms-based theories. Notable exceptions among the early literature are by Mochizuki (1961), Tani et al. (1962), Kendall (1981) and Klebanoff et al. (1992) The measurements reported in this reports previous sections on the receptivity of transient disturbances to surface roughness provide additional data. All of these studies find complicated distortions of the steady flow in the roughness elements' wakes. Just aft of a roughness element in what Kendall (1981) refers to as the near-wake region, the flow is decelerated in the x–y (spanwise–wall-normal) plane that passes through the roughness element's center. However, farther downstream, the velocities in this plane can become accelerated with decelerated velocities on either side of the centerline plane. For this far-wake region the finding is that if the roughness element is not sufficiently large to cause transition the velocity excess can grow slightly but eventually decays.

In the context of the developing understanding of transient growth, what occurs when Re_k is below $Re_{k,\mathrm{crit}}$ is that the roughness elements produce a large initial disturbance that may be quite different than an optimal disturbance. The results by Kendall (1981) and those given in the preceding sections show that realizable disturbances include a decelerated profile directly behind the roughness element and that the energy of this disturbance decays rapidly for a short distance (Kendall's near wake). Farther downstream, some transient growth occurs that may or may not be significant relative to the disturbance's initial amplitude (Kendall's far wake). The transient growth results from the integrated effect of the stationary horseshoe vortex that redistributes streamwise momentum across the shear layer. This is the "lift-up" mechanism described by Landahl(Landahl 1980).

Vortex-shedding in the wake of moderate- to large-amplitude elements supports the notion that transition beyond $Re_{k,\mathrm{crit}}$ is due to an instability of elements' distorted wake flow. However, there are only a few studies that correlate the fluctuation intensities to particular locations in the wake. One of these is a series of u'_{rms} measurements by Klebanoff et al. (1992) in the near wake of a hemispherical roughness element. The measurements were obtained across a range of span locations for various heights in the boundary layer. High in the boundary layer there is a single peak of u'_{rms} centered at the roughness location while lower in the boundary layer there are two peaks that are located on either side of the roughness centerline. These results hint at a complicated instability associated with the various features of the distorted wake flow.

5.2 Bypass transition measurements for large Re_k

The details of the instabilities associated with bypass transition at Re_k near $Re_{k,\mathrm{crit}}$ are investigated by obtaining measurements of the steady and unsteady streamwise velocity fields U and u' in the wake of three spanwise arrays of 3D cylindrical roughness elements. These arrays all have $\lambda_k = 19$ mm and $d = \lambda_k/3$ and are located at $x_k = 300$ mm ($x_{\mathrm{vle}} = -7$ mm). The unit Reynolds number of the freestream flow is $Re' = 764 \times 10^3$ m^{-1}. Three different roughness heights are used that produce $Re_k = 202$, 264 and 334. The middle value, $Re_k = 264$ is expected to be very close to the critical Re_k for transition for this roughness configuration.

Beginning with the lowest Re_k array, the steady flow produced by this roughness array is illustrated by Figs. 44 and 45 which give the spatially phase-lock averaged steady streamwise velocities at $x =$

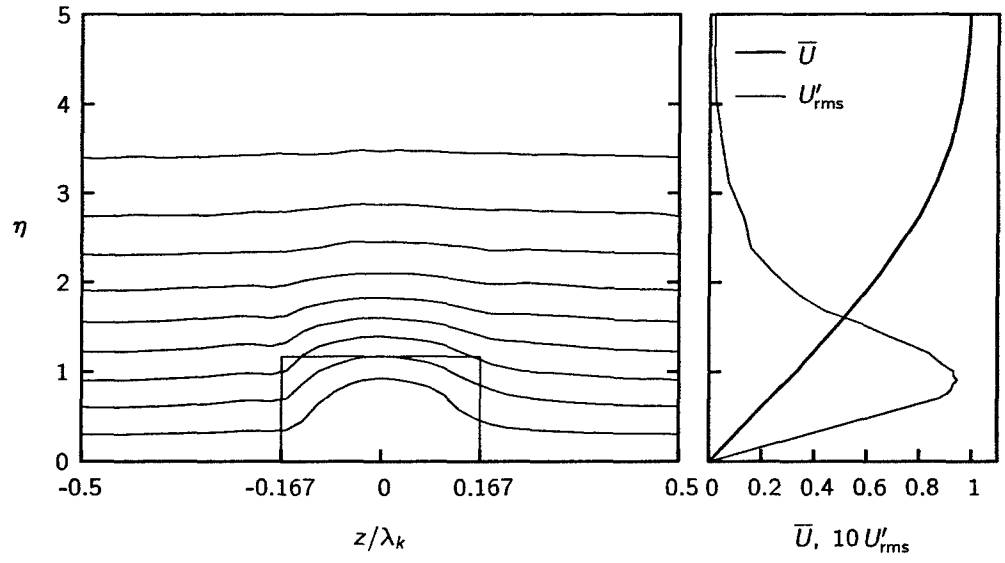

Figure 44: Streamwise velocity contours (left) and steady flow profiles (right) for $x = 310$ mm, $Re_k = 202$. Contour lines indicate 10% increments of U_∞. The rectangular box indicates the approximate size and location of the roughness element's projection onto the the η, z plane.

310 mm and 330 mm, respectively. In each plot the rectangle in the contour plot indicates the approximate projection of the $Re_k = 202$ roughness element onto the η, z plane. The $\overline{U}(\eta)$ profiles indicated by heavy solid lines are in excellent agreement with the Blasius profile. The two larger-amplitude roughness arrays with $Re_k = 264$ and 334 generate nearly identical $\overline{U}(\eta)$ profiles and $U'_{\rm rms}(\eta)$ profiles whose amplitudes scale roughly as Re_k.

The evolution of the steady disturbance energy generated by the three arrays is shown in Fig. 46. In all configurations the total disturbance energy decreases rapidly just aft of the roughness elements but undergoes transient growth farther downstream. In the $Re_k = 202$ and 264 configurations the algebraic growth rate decreases with increasing x and, beyond $x = 400$ mm, the total disturbance energy remains roughly constant for the remaining portion of the measurement domain. This behavior is consistent with what is observed in preceding roughness-induced transient growth experiments. However, for $Re_k = 334$, $E_{\rm rms}$ undergoes a second rapid decrease beginning at $x = 425$ mm. This occurs because the roughness is supercritical and trips turbulence. The resulting turbulent mixing reduces the spanwise velocity gradients and, consequentially, the energy of the steady disturbances. As will be discussed more fully below, the flow is observed to be completely turbulent downstream of $x = 475$ mm.

The unsteady disturbance field generated by surface roughness is observed by monitoring the downstream evolution of the fluctuation intensity. Figure 47 shows contours of the steady and unsteady streamwise velocities for the baseline $Re_k = 202$ configuration at $x = 310$, 350, 400 and 500 mm. Although data is available behind eight roughness elements only half of those are plotted. The colored contours in this figure indicate the temporal $u'_{\rm rms}$ velocity fluctuation intensity. (The contour levels follow an exponential distribution so that wide variations in $u'_{\rm rms}$ can be visualized.) The maximum value of $u'_{\rm rms}$ in this figure is 0.4% of U_∞. Overlaid on the unsteady fluctuation contours are the steady U velocity contour lines. In the near wake at $x = 310$ mm, the fluctuations are weak and concentrated in lobes above and downstream of the spanwise edges of the roughness elements. Moving

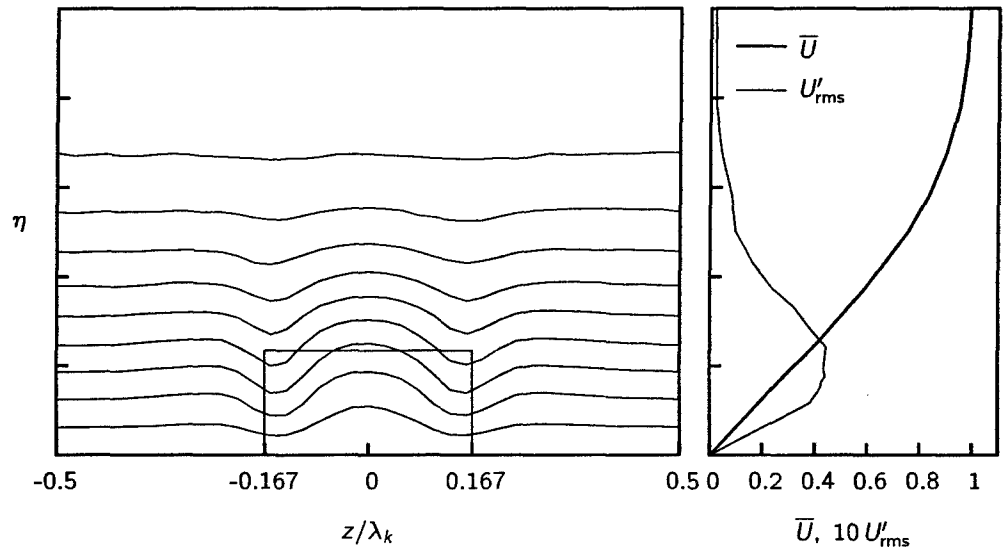

Figure 45: Streamwise velocity contours (left) and steady flow profiles (right) for $x = 330$ mm, $Re_k = 202$.

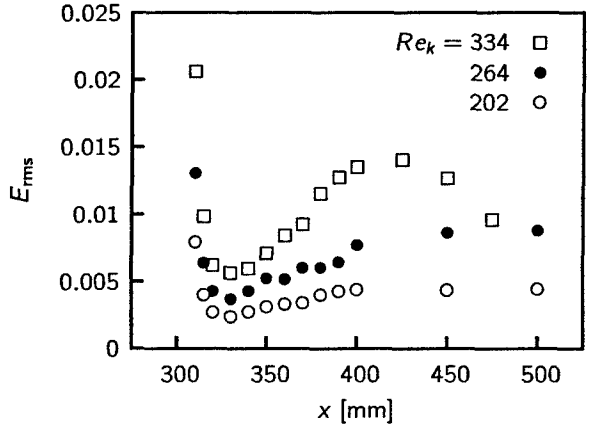

Figure 46: Streamwise evolution of the steady disturbance energy, E_{rms}.

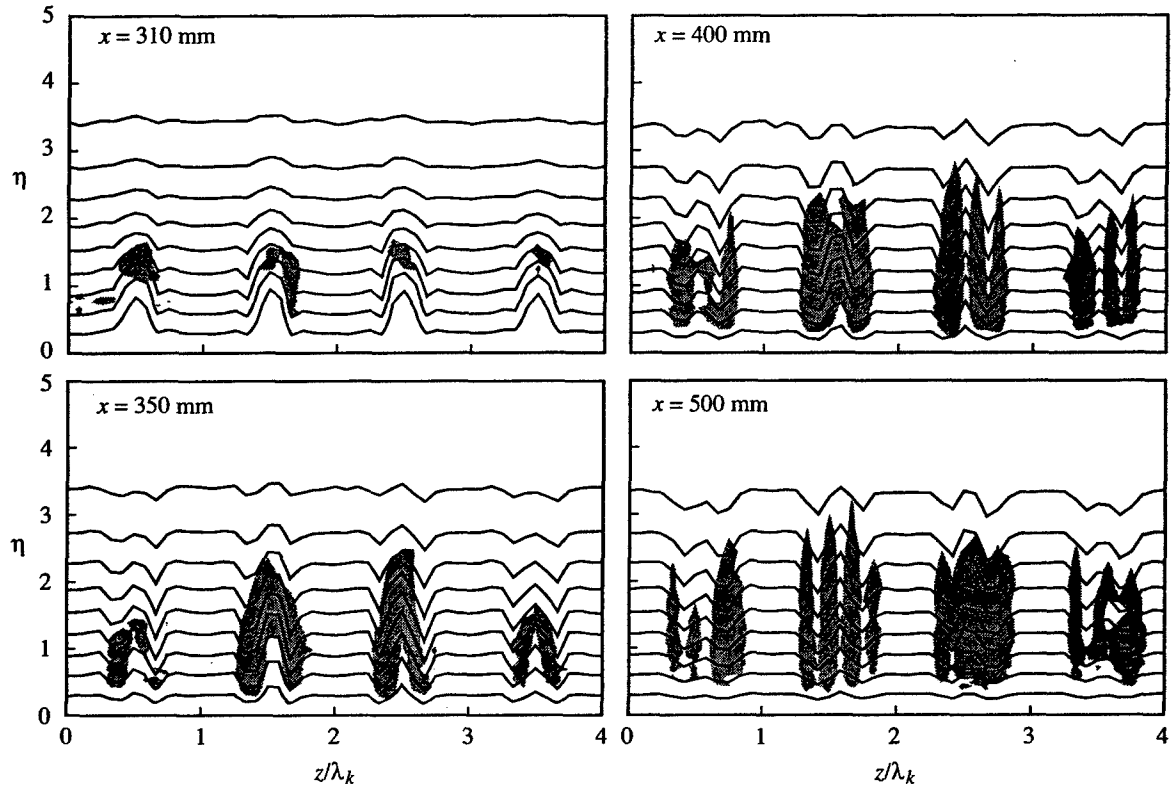

Figure 47: Contours of u'_{rms} and U for $Re_k = 202$. The black lines are 10% increments of U_∞ in U and the filled colored contours are exponentially distributed contours of u'_{rms}.

downstream to $x = 350$ mm, the fluctuations become stronger and cover a wider spanwise region. The lobes evolve into inverted V-shaped structures that are roughly symmetric about the roughness elements' centerlines. These structures could be interpreted as elongated hairpin vortices tethered to the roughness elements on their spanwise edges. At $x = 400$ mm the fluctuation intensity decreases as the structures split into as many as four lobes and cover an even larger spanwise region. It is possible that the structures all split into four lobes but that two or three lobes are sometimes observed because of the measurements' limited spanwise resolution.

A critical point is well illustrated at in the wake of the second roughness element at $x = 500$ mm. Here the u'_{rms} distribution is split into four nearly identical lobes and these are centered exactly in the regions where the spanwise gradient of the steady streamwise velocity ($\partial U/\partial z$) is a maximum. This indicates that the fluctuations are not unsteady transient disturbances but are likely to be the remnants of a Kelvin–Helmholz (KH) instability that arises at the spanwise inflection points of the streamwise velocity, that is, locations where $\partial^2 U/\partial z^2 = 0$. Nearly identical behavior with somewhat larger fluctuation intensities is observed in the wake of the $Re_k = 264$ roughness array.

Another important point is indicated by Fig. 47. Although great attention is given to produce identical roughness elements, there is great deal of variations among roughness elements' fluctuation intensities, as much as an order of magnitude in u'_{rms}. Therefore, spanwise phase-locked averaging technique is not used for unsteady fluctuation intensities.

Figure 48 shows the distribution and evolution of u'_{rms} for the transitional configuration, $Re_k = 334$, with the same contour levels used in Fig. 47. It is immediately apparent that both the unsteady fluctuation intensity and the steady disturbance levels are higher than that for the baseline configuration. Immediately downstream of the roughness array, the unsteady velocity fluctuations are concentrated in three regions, one directly above the roughness centerline and two on both sides of the roughness element. These regions are most distinct and symmetric for third and fourth elements from the left. The two lobes located downstream of either side of the roughness element can again be interpreted as the two legs of the horseshoe vortex. At $x = 350$ mm, the unsteady fluctuations are greatly intensified compared to the same streamwise location for the baseline configuration. Additionally, the spanwise region covered by the fluctuations is increased such that the second and third roughness elements' unsteady wakes are joined. At this location, the second roughness element's fluctuations are the most extensive in the wall-normal direction, as they reach the edge of the boundary layer. A stronger inverted V-shaped structure is observed downstream of the rightmost roughness element. At $x = 400$ mm, abrupt changes occur in both the steady and unsteady disturbances. The unsteady wakes of all roughness elements shown in this figure are joined and most of the boundary layer is contaminated by turbulent fluctuations. The mixing downstream of the middle two roughness elements is most severe and the steady velocity contours to from their usual laminar appearance. Further downstream, at $x = 475$ mm, the flow is completely contaminated by unsteady fluctuations with high turbulence levels. The steady velocity contours are strongly affected by turbulent mixing and are well on their way toward a fully developed turbulent boundary layer profile. The maximum u'_{rms} in this figure is 14% of U_∞.

It is obvious from Fig. 48 that the middle two roughness elements generate the strongest disturbances and trigger turbulent flow. The second roughness element's wake is selected for data analysis for each of the three roughness array amplitudes. The downstream evolution of e_{rms} generated by this element is shown in Fig. 49. With increasing downstream distance, the unsteady disturbance energy slightly increases and remains constants for $Re_k = 202$ and 264. For the transitional $Re_k = 334$ configuration it experiences exponential growth prior to transition.

The important frequencies associated with the transitional disturbance input can be revealed from the frequency spectrum of the unsteady fluctuations. Figure 50 shows the downstream evolution of the temporal power spectrum along the centerline of the second roughness element's wake for $Re_k = 334$. Each plot represents a particular streamwise location and each curve within a plot represents a particular height in the boundary layer. In the near wake, at $x = 310$ mm, peaks are observed at 360 and a 720 Hz with the latter surrounded by a band of frequencies from 600 to 800 Hz. This band will be referred to as the 700 Hz band. It is unfortunate that these values are harmonics of 60 Hz but contour plots of the bands' integrated intensities are similar to those in Figs. 47 and 48 and it is concluded that these frequencies are associated with the disturbance input and not electronic noise.

Between $x = 330$ and 360 mm, harmonics of the 700 Hz frequency band start to form as ripples in the high-frequency region of the spectra at different heights. These harmonics increase with increasing downstream distance and gradually give the power spectrum a turbulent appearance. At $x = 350$ mm, the power spectrum at $\eta = 1$ appears almost turbulent whereas the spectrum at $\eta = 2$ still has rippled structure. The spectra at $\eta = 3$ and 4 follow the same trend, lagging the others in x-direction. This suggests that the turbulent fluctuations of roughness induced disturbances propagate from the lower parts of the boundary layer to the upper parts with increasing downstream distance. By $x = 400$ mm, power spectra at all heights indicate a turbulent flow.

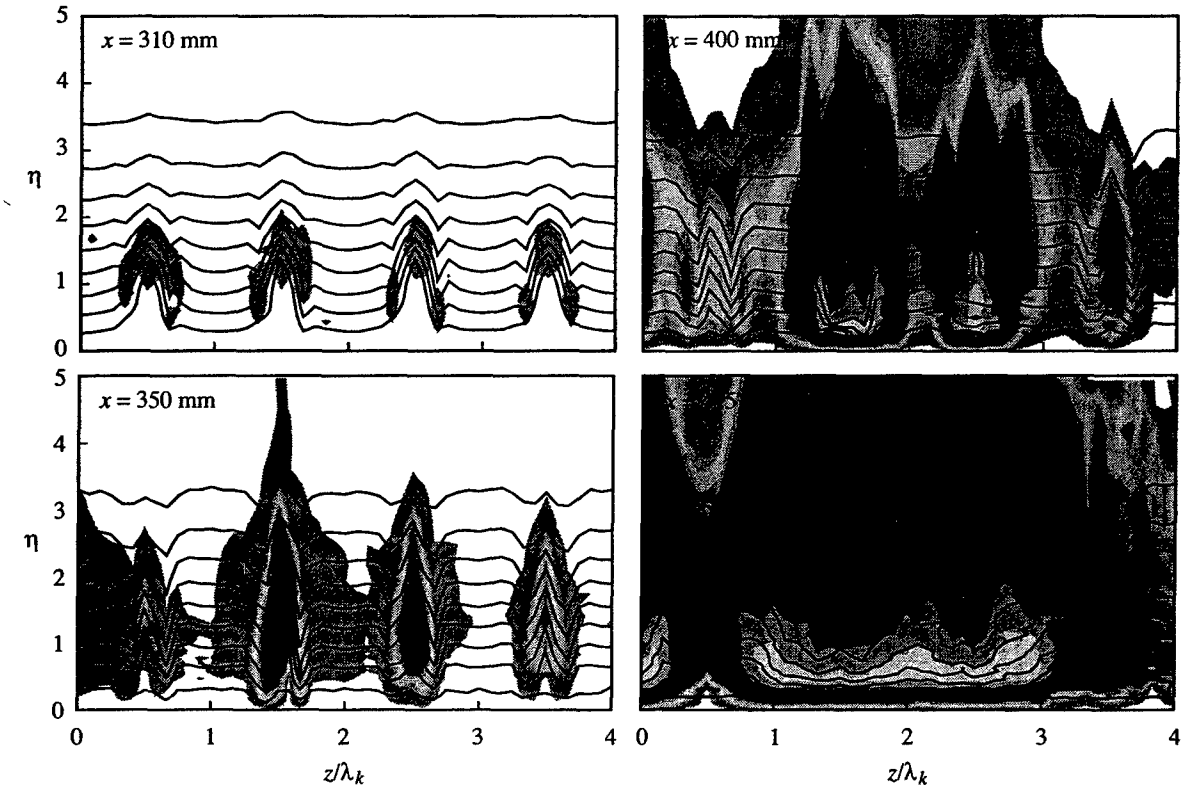

Figure 48: Contours of u'_{rms} and U for $Re_k = 334$. The black lines are 10% increments of U_∞ in U and the filled colored contours are exponentially distributed contours of u'_{rms}.

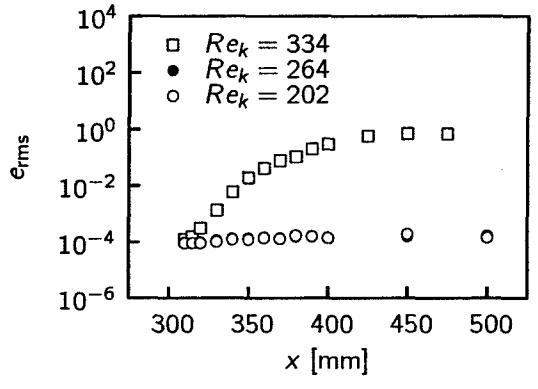

Figure 49: Streamwise evolution of the unsteady disturbance energy, e_{rms}.

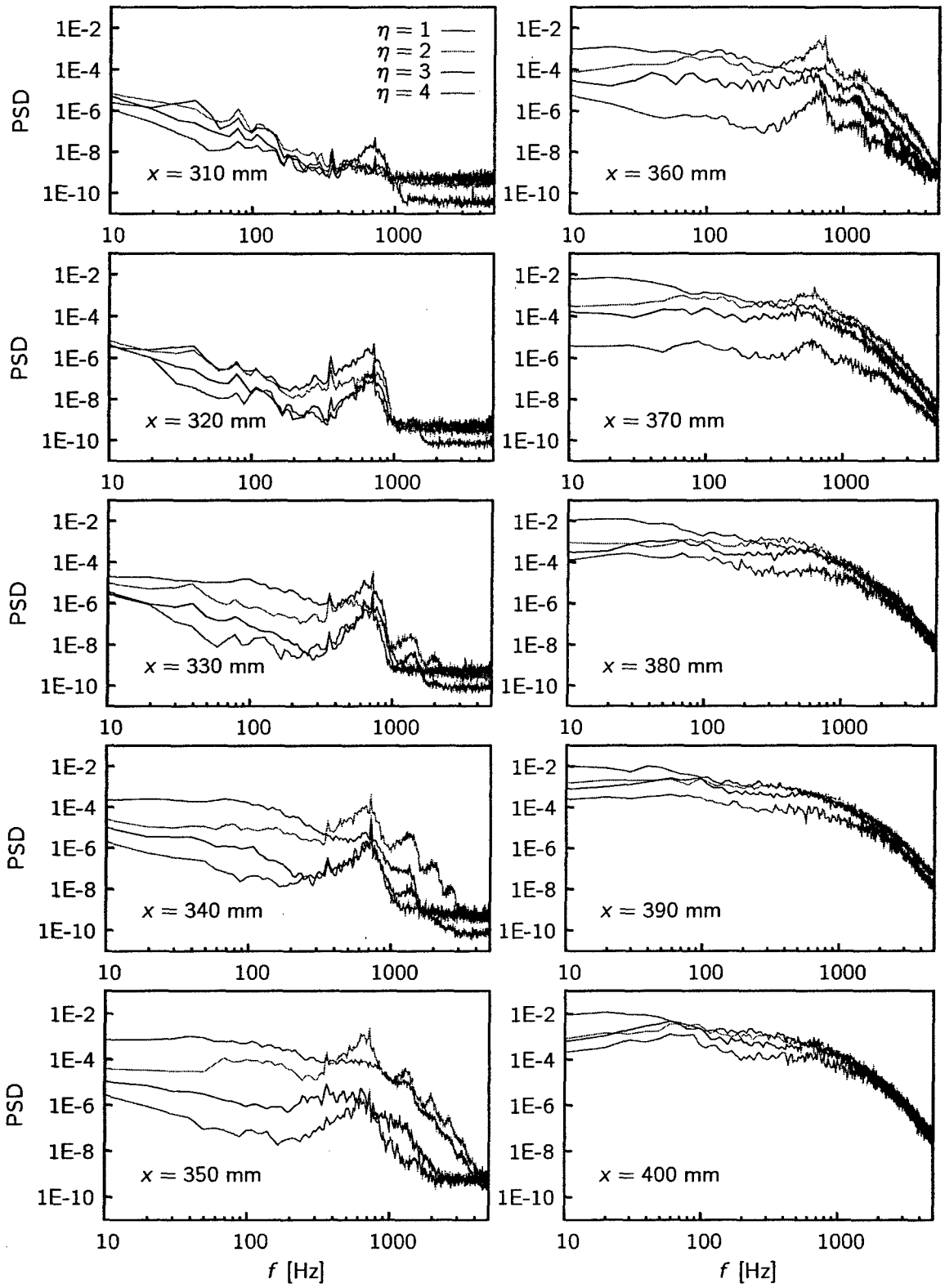

Figure 50: Temporal power spectra of the unsteady disturbances for $Re_k = 334$.

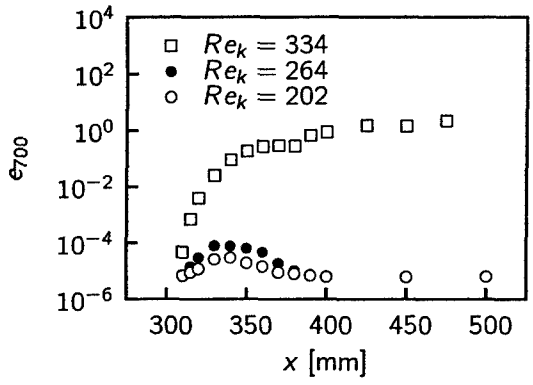

Figure 51: Streamwise evolution of the 700 Hz band's disturbance energy, e_{700}.

Similar to the rms disturbance disturbance energy, e_{rms}, a quantitative assessment of the unsteady disturbance growth can be given for the 700 Hz frequency band using e_{700}. The downstream evolution of this quantity for the second roughness element's wake is shown in Fig. 51. First, e_{700} increases with increasing Re_k. Next, the $Re_k = 202$ and 264 configurations' e_{700} grows until $x = 330$ mm then decay somewhat and remain constant for the rest of the streamwise domain. On the other hand, the transitional disturbance input experiences a exponential growth until about $x = 400$ mm and remains fairly constant for the next 75 mm. A plausible interpretation of this behavior is that the near wakes of all three roughness arrays are initially unstable to the 700-Hz disturbance. However, the stationary disturbance decreases rapidly (see Fig. 46) and, at some point, the flow becomes stable to these disturbances and their energy decreases. The exception is the transitional case where $Re_k = 334$. Here, the steady disturbance is sufficiently large that the unsteady disturbances are able to bring about transition before they enter a stable region.

Klebanoff et al. (1992) performed similar experiments using isolated 3.2-mm-high hemispherical and cylindrical roughness elements with diameters of 6.3 mm and 3.2 mm, respectively. Those authors report that bypass transition is observed at $Re_k = 325$ for hemispherical roughness elements and at $Re_k = 450$ for cylindrical roughness elements. In that study, the transition is defined as the first occurrence of turbulent bursts in the oscilloscope with a hotwire positioned on the roughness centerline close to the surface. Klebanoff et al. suggest that the Strouhal number, St, is not a strong function of Re_k, when calculated as $St = f_s \delta^* / U_k$, where f_s is the shedding frequency, δ^* is the displacement thickness and U_k is the flow velocity at roughness height. For hemispherical and cylindrical roughness elements, Klebanoff et al. report Strouhal numbers of 0.3 and 0.25, respectively. However, Klebanoff et al.'s Fig. 23 indicates that for cylindrical roughness elements, St does decrease somewhat with decreasing Re_k as Re_k approaches values used in the current work. The shedding frequency of $f_s = 720$ Hz obtained here corresponds to $St = 0.17$ for Rek=202 which is consistent with a reasonable extrapolation of Klebanoff et al.'s data. Moreover, the height-to-diameter aspect ratio of the cylindrical roughness elements is quite a bit lower in the current work than those used by Klebanoff et al. and this could be another reason for the somewhat lower Strouhal number.

6 Conclusions

This experimental project examines several issues connected with the transient algebraic growth of disturbances created by surface roughness in a zero-pressure-gradient boundary layer. These include fundamental transient growth behavior, receptivity and bypass transition at high roughness levels. The experiments that use hotwire anemometry to track the streamwise evolution of the steady and unsteady disturbances.

The results establish that surface roughness does create disturbances that undergo transient growth and that it does so in a manner consistent with the physical picture known as Landahl's (1980) lift-up mechanism. The observed growth is qualitatively similar to what is predicted by optimal-disturbance theory but theoretical predictions tend to overestimate the length over which disturbances grow and are thought to overestimate the total amount of transient growth. The difference between what is predicted by optimal disturbance theories and what is observed in the experiments is linked to receptivity. Receptivity is found to play two roles in transient growth situations: it determines the amplitude of the disturbances and also determines the character of the transient growth by distributing disturbance energy among the decaying modes of the continuous spectrum that represents solutions of the Orr–Sommerfeld/Squire system. It is observed that certain disturbances undergo algebraic growth and decay that is very similar to the evolution of optimal disturbances while other disturbances undergo only decay and other disturbances undergo initial decay and then undergo a weak transient growth and secondary decay. Why certain disturbances behave in the manner that they do is not yet fully understood. In spite of these differences, the energy of disturbances generated by spanwise arrays of 3D roughness elements appear to scale as Re_k^2 for Re_k values as low as 16 and extending to values that produce a roughness-induced bypass transition in the near wake of the roughness array ($Re_k \approx 250$).

The limit of transient-growth behavior on the threshold of the critical Re_k for bypass transition is investigated. At values of Re_k that exceed 250, unsteady disturbances are found to lead to rapid transition just aft of the roughness elements. This transition stems from a Kelvin–Helmoltz type instability of the elements' wake. It is found that this transition is not connected to transient growth. Rather, transient growth only manifests itself if the boundary-layer does not immediately transition.

Unresolved issues that will be investigated at Case Western Reserve University as a follow-up to the present work include experiments that will attempt to better explain the receptivity selection mechanism and also experiments that further investigate how random, distributed roughness leads to transient growth.

References

Acarlar, M. and C. Smith (1987). A study of hairpin vortices in a laminary boundary layer. Part 1. Hairpin vortices generated by a hemisphere protuberance. *J. Fluid Mech. 175*, 1–41.

Andersson, P., M. Berggren, and D. S. Henningson (1999). Optimal disturbances and bypass transition in boundary layers. *Phys. Fluids 11*(1), 134–150.

Andersson, P., L. Brant, B. Allessandro, and D. Henningson (2001). On the breakdown of boundary layer streaks. *J. Fluid Mech. 428*, 29–60.

Boberg, L. and U. Brosa (1988). Onset of turbulence in a pipe. *Z. Naturforsch., A: Phys. Sci. 43*, 697.

Breuer, K. S. and J. H. Haritonidis (1990). The evolution of a localized disturbance in a laminar boundary layer. Part 1. Weak disturbances. *J. Fluid Mech. 220*, 569–594.

Bruun, H. H. (1995). *Hot-Wire Anemometry Principles and Signal Analysis*. Oxford University Press.

Butler, K. and B. Farrell (1992). Three-dimensional optimal perturbations in viscous shear flow. *Phys. Fluids A 4*(8), 1637–1650.

Cossu, C. and L. Brandt (2002). Stabilization of Tollmien–Schlicting waves by finite amplitude optimal streaks in the Blasius boundary layer. *Phys. Fluids 14*(8), L57–L60.

Cossu, C. and L. Brandt (2004). On Tollmien–Schlichting-like waves in streaky boundary layers. *European J. Mech. B/Fluids 23*(6), 815–833.

Dryden, H. L. (1959). Transition from laminar to turbulent flow. In C. C. Lin (Ed.), *Turbulent Flows and Heat Transfer*, Volume 5 of *High Speed Aerodynamics and Jet Propulsion*, pp. 3–74. Princton University Press.

Ellingsen, T. and E. Palm (1975). Stability of linear flow. *Phys. Fluids 18*, 487.

Farrell, B. F. (1988). Optimal excitation of perturbations in viscous shear flow. *Phys. Fluids 31*, 2093.

Gaster, M., C. E. Grosch, and T. L. Jackson (1994). The velocity field created by a shallow bump in a boundary layer. *Phys. Fluids 6*(9), 3079–3085.

Gregory, N. and W. S. Walker (1950). The effect on transition of isolated surface excrescences in the boundary layer. Aero. Res. Council Tech. Report 13436. republished as Aero. Res. Council R. & M. 2779, 1956.

Grosch, C. E. and H. Salwen (1978). The continuous spectrum of the orr–sommerfeld equation. Part 1. The spectrum and the eigenfunctions. *J. Fluid Mech. 87*, 33–54.

Hinze, J. O. (1959). *Turbulence. An introduction to its mechanism and theory.* New York: McGraw-Hill.

Jørgensen, F. E. (1971). Directional sensitivity of wire and fibre-film probes. *DISA Info. 11*, 31–37.

Joslin, R. D. and C. E. Grosch (1995). Growth characteristics downstream of a shallow bump: Computation and experiment. *Phys. Fluids 7*(12), 3042–3047.

Kendall, J. (1981). Laminar boundary layer velocity distortion by surface roughness: Effect upon stability. AIAA Paper 81-0195.

Kendall, J. M. (1985). Experimental study of disturbances produced in a pre-transitional laminar boundary layer by weak freestream turbulence. AIAA Paper 85-1695.

Klebanoff, P., W. Cleveland, and K. Tidstrom (1992). On the evolution of a turbulent boundary layer induced by a three-dimensional roughness element. *J. Fluid Mech. 237*, 101–187.

Klebanoff, P., G. Schubauer, and K. Tidstrom (1955). Measurements of the effect of two-dimensional and thee-dimensional roughness elements on boundary-layer transition. *J. Aero. Sci. 22*, 803–804.

Klebanoff, P. S. (1971). Effect of free-stream turbulence on the laminar boundary layer. *Bull. APS 10*, 1323.

Landahl, M. T. (1980). A note on an algebraic instability of inviscid parallel shear flows. *J. Fluid Mech. 98*, 243–251.

Luchini, P. (2000). Reynolds-number-independent instability of the boundary layer over a flat surface: Optimal perturbations. *J. Fluid Mech. 404*, 289–309.

Matsubara, M. and P. H. Alfredsson (2001). Disturbance growth in boundary layers subjected to free-stream turbulence. *J. Fluid Mech. 430*, 149–168.

Mochizuki, M. (1961, December). Hot-wire investigations of smoke patterns caused by a spherical roughness element. *Nat. Sci. Report, Ochanomizu Univ. 12*(2), 87–101.

Morkovin, M., E. Reshotko, and T. Herbert (1994). Transition in open flow systems—A reassessment. *Bull. APS 39*(9), 1882.

Morkovin, M. V. (1990). On roughness-induced transition: Facts, views & speculation. In M. Y. Hussaini and R. G. Voight (Eds.), *Instability and Transition*, Volume 1, pp. 281–295. Springer.

Naguib, A. M., S. P. Gravante, and C. E. Wark (1996). Extraction of turbulent wall-pressure time-series using an optimal filtering scheme. *Exper. in Fluids 22*, 14–22.

Radeztsky, Jr., R. H., M. S. Reibert, and W. S. Saric (1999). Effect of isolated micron-sized roughness on transition in swept-wing flows. *AIAA J. 37*(11), 1371–1377.

Reshotko, E. (2001). Transient growth—A factor in bypass transition. *Phys. Fluids 13*(5), 1067–1075.

Reshotko, E. and L. Leventhal (1981). Preliminary experimental study of disturbances in a laminar boundary layer due to distributed roughness. AIAA Paper 81-1224.

Reshotko, E., W. S. Saric, and H. M. Nagib (1997). Flow quality issues for large wind tunnels. AIAA Paper 97-0225.

Saric, W. S. (1996). Low-speed boundary layer transition experiments. In T. C. Corke, G. Erlebacher, and M. Hussaini (Eds.), *Transition: Experiments, Theory and Computation.*

Saric, W. S., R. B. Carrillo, Jr., and M. S. Reibert (1998). Nonlinear stability and transition in 3-D boundary layers. *Meccanica 33*, 469–487.

Saric, W. S., H. L. Reed, and E. J. Kerschen (2002). Boundary-layer receptivity to freestream disturbances. *Ann. Rev. Fluid Mech. 34*, 291–319.

Schmid, P. J. and D. S. Henningson (2001). *Stability and transition in shear flows.* New York: Springer.

Sedney, R. (1973). A survey of the effect of small protuberances on boundary-layer flows. *AIAA J. 11*, 782–92.

Smith, A. and D. W. Clutter (1959). The smallest height of roughness capable of affecting boundary-layer transition. *J. Aero. Sci. 26*(4), 229–245,256.

Tani, I. (1961). Effect of two-dimensional and isolated roughness on laminar flow. In G. V. Lachmann (Ed.), *Boundary Layer and Flow Control*, Volume 2, pp. 637–656. Pergamon.

Tani, I. (1969). Boundary-layer transition. *Annu. Rev. Fluid Mech. 1*, 169–196.

Tani, I., A. Komoda, Y. Komatsu, and M. Iuchi (1962). Boundary layer transition by isolated roughness. Technical Report 375, Aero. Res. Inst., Tokyo Univ.

Tumin, A. (2003). Multimode decomposition of spatially growing perturbations in a two-dimensional boundary layer. *Phys. Fluids 15*(9), 2525–2540.

Tumin, A. and E. Reshotko (2001). Spatial theory of optimal disturbances in boundary layers. *Phys. Fluids 13*(7), 2097–2104.

Tumin, A. and E. Reshotko (2004). The problem of boundary-layer flow encountering a three-dimensional hump revisited. AIAA Paper 2004-0101.

von Doenhoff, A. E. and A. L. Braslow (1961). The effect of distributed surface roughness on laminar flow. In G. V. Lachmann (Ed.), *Boundary Layer and Flow Control*, Volume 2, pp. 657–681. Pergamon.

Westin, K. J. A., A. V. Boiko, B. G. B. Klingmann, V. V. Kozlov, and P. H. Alfredsson (1994). Experiments in a boundary layer subjected to free stream turbulence. Part 1. Boundary layer structure and receptivity. *J. Fluid Mech. 281*, 193–218.

White, E. B. and E. Reshotko (2002). Roughness-induced transient growth in a flat-plate boundary layer. AIAA Paper 2002-0138.

REPORT DOCUMENTATION PAGE

AFRL-SR-AR-TR-05-

01666

1. REPORT DATE *(DD-MM-YYYY)*	2. REPORT TYPE	3. DATES COVERED *(From - To)*
28-03-2005	Final	01 Dec 2001 -- 30 Nov 2004

4. TITLE AND SUBTITLE
Experiments in Transient Growth and Roughness-Induced Bypass Transition

5a. CONTRACT NUMBER

5b. GRANT NUMBER
F49620-02-1-0058

5c. PROGRAM ELEMENT NUMBER

6. AUTHOR(S)
Edward B. White

5d. PROJECT NUMBER

5e. TASK NUMBER

5f. WORK UNIT NUMBER

7. PERFORMING ORGANIZATION NAME(S) AND ADDRESS(ES)
Case Western Reserve University
10900 Euclid Ave.
Cleveland, OH 44106

8. PERFORMING ORGANIZATION REPORT NUMBER

9. SPONSORING/MONITORING AGENCY NAME(S) AND ADDRESS(ES)
Air Force Office of Scientific Research
4015 Wilson Boulevard, Room 713
Arlington, VA 22203-1954

10. SPONSOR/MONITOR'S ACRONYM(S)

11. SPONSOR/MONITOR'S REPORT NUMBER(S)

12. DISTRIBUTION/AVAILABILITY STATEMENT
Distribution Statement A. Approved for public release; distribution is unlimited.

13. SUPPLEMENTARY NOTES

14. ABSTRACT

The work reported here is a series of wind-tunnel experiments that establishes the basic behavior of roughness-induced disturbances that undergo transient algebraic growth in a laminar boundary layer. The experiments explore the disturbances' fundamental response to various configurations of surface roughness, their receptivity, and their behavior when the surface roughness amplitude is large. The results establish that roughness-induced disturbances undergo transient that is qualitatively similar to what is predicted by optimal-disturbance theory. However, these predictions overestimate the length over which disturbances grow and the total amount of growth. The discrepancy is linked to receptivity. Receptivity is found both to determine initial disturbance amplitude and to distribute energy among the modes of the continuous disturbance spectrum. At high values of the roughness-based Reynolds number transition occurs just aft of the roughness elements. This transition does not appear to be connected with transient growth. Rather, it occurs because the element's wakes are unstable to a high-frequency instability mechanism.

15. SUBJECT TERMS
transient growth
boundary-layer instability
roughness

16. SECURITY CLASSIFICATION OF:			17. LIMITATION OF ABSTRACT	18. NUMBER OF PAGES	19a. NAME OF RESPONSIBLE PERSON
a. REPORT	b. ABSTRACT	c. THIS PAGE		73	19b. TELEPHONE NUMBER *(Include area code)*